LASER-DRIVEN ROTATIONAL DYNAMICS OF GAS-PHASE MOLECULES: CONTROL AND APPLICATIONS

by

XIAOMING REN

B.S., University of Science and Technology of China, China, 2007

AN ABSTRACT OF A DISSERTATION

submitted in partial fulfillment of the
requirements for the degree

DOCTOR OF PHILOSOPHY

Department of Physics
College of Arts and Sciences

KANSAS STATE UNIVERSITY
Manhattan, Kansas
2013

Abstract

In this thesis, our work on developing new techniques to measure and enhance field-free molecular alignment and orientation is described. Non-resonant femtosecond laser pulses are used to align and orient rotationally-cold gas-phase molecules. The time-dependent Schrödinger equation is solved to simulate the experimental results. A single-shot kHz velocity map imaging (VMI) spectrometer is developed for characterizing 1D and 3D alignment. Stimulated by a novel metric for 3D alignment proposed by Makhija *et al.* [Phys. Rev. A **85**,033425 (2012)], a multi-pulse scheme to improve 3D alignment is demonstrated experimentally on difluoro-iodobenzene molecules and the best field-free 3D alignment is achieved. A degenerate four wave mixing probe is developed to overcome limitations in VMI measurement; experiments on different types of molecules show good agreement with computational results. Highly aligned linear molecules are used for high harmonic generation experiments. Due to the high degree of alignment, fractional revivals, variation of revival structure with harmonic order and the shape resonance and Cooper minimum in the photoionization cross section of molecular nitrogen are all observed directly in experiment for the first time. Enhanced orientation from rotationally cold heteronuclear molecules is also demonstrated. We follow the theory developed by Zhang *et al.* [Phys. Rev. A **83**, 043410 (2011)] and demonstrate experimentally for the first time that for rotationally cold carbon monoxide an aligning laser pulse followed by a two-color laser pulse can increase field-free orientation level by almost a factor of three compared to using just the two-color pulse.

LASER-DRIVEN ROTATIONAL DYNAMICS OF GAS-PHASE MOLECULES: CONTROL AND APPLICATIONS

by

XIAOMING REN

B.S., University of Science and Technology of China, China, 2007

A DISSERTATION

submitted in partial fulfillment of the
requirements for the degree

DOCTOR OF PHILOSOPHY

Department of Physics
College of Arts and Sciences

KANSAS STATE UNIVERSITY
Manhattan, Kansas
2013

Approved by:

Major Professor
Vinod Kumarappan

Copyright

Abstract

In this thesis, our work on developing new techniques to measure and enhance field-free molecular alignment and orientation is described. Non-resonant femtosecond laser pulses are used to align and orient rotationally-cold gas-phase molecules. The time-dependent Schrödinger equation is solved to simulate the experimental results. A single-shot kHz velocity map imaging (VMI) spectrometer is developed for characterizing 1D and 3D alignment. Stimulated by a novel metric for 3D alignment proposed by Makhija *et al.* [Phys. Rev. A **85**,033425 (2012)], a multi-pulse scheme to improve 3D alignment is demonstrated experimentally on difluoro-iodobenzene molecules and the best field-free 3D alignment is achieved. A degenerate four wave mixing probe is developed to overcome limitations in VMI measurement; experiments on different types of molecules show good agreement with computational results. Highly aligned linear molecules are used for high harmonic generation experiments. Due to the high degree of alignment, fractional revivals, variation of revival structure with harmonic order and the shape resonance and Cooper minimum in the photoionization cross section of molecular nitrogen are all observed directly in experiment for the first time. Enhanced orientation from rotationally cold heteronuclear molecules is also demonstrated. We follow the theory developed by Zhang *et al.* [Phys. Rev. A **83**, 043410 (2011)] and demonstrate experimentally for the first time that for rotationally cold carbon monoxide an aligning laser pulse followed by a two-color laser pulse can increase field-free orientation level by almost a factor of three compared to using just the two-color pulse.

Table of Contents

Table of Contents vi

List of Figures viii

List of Tables xi

Acknowledgements xiii

1 Introduction to laser induced molecular alignment 1
- 1.1 Background . . . 1
- 1.2 Theoretical treatment of field-free one dimensional alignment . . . 7
  - 1.2.1 Linear and symmetric-top molecules . . . 7
  - 1.2.2 Asymmetric-top molecules . . . 13
- 1.3 Improving molecular alignment . . . 16

2 A one kHz velocity map imaging spectrometer for measuring molecular alignment 19
- 2.1 Introduction . . . 19
- 2.2 A single shot one kHz system and analysis of the images . . . 20
- 2.3 Measuring FF1DA . . . 25

3 Field-free three-dimensional alignment 31
- 3.1 Introduction to FF3DA . . . 31
- 3.2 A metric for 3DA and a multi-pulse scheme to enhance FF3DA . . . 33
- 3.3 Experiment of multi-pulse FF3DA . . . 40
- 3.4 Tomographic measurement . . . 43

4 Optical measurement of molecular alignment 47
- 4.1 Introduction to different optical measurements . . . 47
- 4.2 A pump-degenerate four wave mixing technique . . . 52
- 4.3 A pulse shaping setup to enhance FF1DA . . . 60

5 High Harmonic Generation from aligned molecules 67
- 5.1 Introduction to high harmonic generation . . . 67
- 5.2 Experiment and calibration of HHG spectrometer . . . 72
- 5.3 HHG from well aligned nitrogen molecules . . . 79
- 5.4 Extracting Photoionization Cross Section from N_2 . . . 83

6 Alignment-assisted orientation of molecules **92**
6.1 Introduction to molecular orientation 92
6.2 Orienting molecules using two-color laser field 94
6.3 Enhanced molecular orientation using a combination of IR and two color-laser field 99

7 Summary **107**

Bibliography **130**

A List of rotational constants, polarizabilities, spin statistics and hyperpolarizabilities for different molecules. **131**

B Derivation of the expression of the third order susceptibility tensor element χ_{ZZZZ} for nitrogen and benzene. **133**

C Coefficients obtained from fitting harmonic delay and angle scans. **137**

List of Figures

1.1 Demonstration of different kinds of alignment and orientation on 3,5-Difluoro-iodobenzene molecules as well as the definition of molecular and lab frames. 2
1.2 TDSE calculation of the alignment trace for linear molecules 10
1.3 TDSE calculation of the alignment trace for a symmetric-top molecule: benzene 13
1.4 TDSE calculation of the alignment trace for an asymmetric top molecule: iodobenzene 14
1.5 A multi-pulse calculation for increasing alignment degree of N_2 molecules. . . 18

2.1 VMI setup and a typical VMI raw image of I^+ ion from aligned DFIB molecules 21
2.2 Producer-consumer model for parallel processing of the images. 24
2.3 VMI images before and after analysis. 25
2.4 Experimental setup for FF1DA of iodobenzene molecules using single pump beam. 26
2.5 Measured alignment trace from iodobenzene molecules. 27
2.6 Experimental setup for multi-pulse FF1DA of N_2 molecules. 28
2.7 Measurement and calculation for aligning N_2 molecules using three pump pulses in VMI. 29

3.1 Structure of 3,4-dibromothiophene, 3,5-difluoroiodobenzene, sulfur dioxide and ethylene molecules. 33
3.2 The four equivalent target orientations for 3DA reached by rotating about the LF axes by 180 degrees. 34
3.3 TDSE calculations of the FF3DA from iodobenzene molecules using two orthogonally polarized pulses as an example to show $\langle \cos^2 \delta \rangle$. 36
3.4 TDSE calculations of the FF3DA from DFIB using four laser pulses, first one is linear, the rest are elliptical. 40
3.5 End and side views of both iodine and fluorine ion fragments before and after each pump pulse. 41
3.6 Time evolutions of the angular distribution in both I^+ side views and F^+ end views after each pump pulse. 43
3.7 Filtered back-projection algorithm. 44
3.8 Reconstructed 3D-momentum distribution for I^+ at the peak of FF1DA and FF3DA. 45

4.1 Experimental setup of the Kerr-effect measurement. 48
4.2 Revival trace in air measured by optical Kerr-effect. 49
4.3 Fourier transform of the revival trace in air measured by optical Kerr-effect . 50

4.4 A demonstration of the phase matching in the transient grating diffraction method. . . . 51
4.5 Measured revival trace in nitrogen gas jet using transient grating method. . . 52
4.6 A demonstration of the pump-degenerate four wave mixing setup. 53
4.7 Experimental setup for the pump-DFWM experiment. 55
4.8 Pump-DFWM measurement and calculation of normalized χ^2_{ZZZZ} component from aligned N_2 molecule. 57
4.9 Pump-DFWM measurement and calculation of normalized χ^2_{ZZZZ} component from aligned C_6H_6 molecule. 58
4.10 Pump-DFWM measurement and calculation of normalized χ^2_{ZZZZ} component from aligned C_6H_5I molecule. 59
4.11 The pulse shaping setup for increasing FF1DA for pump-DFWM experiment. 60
4.12 The changes of the output laser pulses comparing to the inputs with different order of phases added on the SLM using our pulse shaping setup. 62
4.13 A plot shows the cross-correlation of the compressed pulse comparing to the original pulse. The compression is done by optimizing the SH signal using the pulse shaping setup and a genetic algorithm. 63
4.14 Results from optimizing alignment of toluene molecules using our pulse shaping setup. 64
4.15 Cross-correlation of a TL pulse and the optimum pulse from the optimization. 65

5.1 Three-step model for HHG. 67
5.2 Calculated angle and energy dependent photoionization cross section and phase from N_2 HOMO, only parallel component is shown. 72
5.3 Experimental setup for HHG experiment. 73
5.4 HHG spectrum measured from N_2 molecules. 74
5.5 Yield of harmonic 19 from aligned N_2 as a function of pump probe delay. . . 75
5.6 Plasma emission lines from both neon and helium gases and the calibrated harmonic spectrum from Neon. 76
5.7 Calibrate our HHG spectrometer by comparing one of the second order diffraction to its corresponding first order. 78
5.8 The abnormal behavior of harmonic 11 in nitrogen molecule. 79
5.9 Delay scans after the second pump. The normalized experimental revivals, QRS calculations and theoretical fittings are all plotted. 80
5.10 Angle scans at alignment peak for different harmonics as a function of photon energy and pump probe angle, signal has been normalized to isotropic spectrum. 83
5.11 This figure shows experimental harmonic yield, QRS calculation of angle dependent harmonic yield, angle fittings to the experimental harmonic yield and extracted molecular frame angle dependent harmonic yield from fitting both delay and angle scans. 86
5.12 Delay scan measurements and fittings for three different alignment levels from N_2, the extracted Molecular Frame tunneling ionization rates are also plotted for all three cases. 88

5.13 Calculated and extracted angle dependent Nitrogen HOMO PICS. 90

6.1 Experimental setup for orienting CO molecules using two-color laser pulse. . 96
6.2 Measured and calculated $\langle\cos^2\theta_{2D}\rangle$ and $\langle\cos\theta_{2D}\rangle$ traces for a two-color pulse by gating on the highest kinetic energy channel of the C^{2+} fragment. 98
6.3 Measured and calculated $\langle\cos^2\theta\rangle$ and $\langle\cos\theta\rangle$ traces for both IR and two-color pulses by gating on the highest kinetic energy channel of the C^{2+} fragment. . 100
6.4 Abel inverted images for C^{2+} momentum distribution when there is no orientation (no pump), weak orientation (just the two-color pump) and good orientation (both pumps). The corresponding angular distributions are also calculated and shown. 101
6.5 Calculation of alignment and orientation traces for two-color pump and both pumps. The time evolution of orientation from even and odd J states are also plotted separately. Calculated population of rotational J states for each thermally populated initial state for the case of using just IR pump, two-color only pump and both pumps at our experimental conditions are also shown. 103
6.6 Calculated maximum $\langle\cos\theta\rangle$ values at different combinations of blue-IR ratio, two-color total intensity and pumps separation for rotational temperatures of 3 K and 30 K. 105

B.1 The trace of $\frac{\chi^2_{ZZZZ}}{\chi^2_{ZZZZ-iso}}$ as a function of θ for both nitrogen and benzene. . . . 135

List of Tables

1.1 List of different type of revivals and corresponding selection rules for asymmetric top molecules, the formulas for calculating the revival time and the numbers for iodobenzene molecules are given. 15

5.1 List of retrieved rotational temperatures, laser parameters and coefficients of D^0_{00}, D^2_{00} and D^4_{00} for three different aligning pump pulses. T is in units of Kelvin, τ and I are in units of fs and TW/cm^2 respectively and t_{sep} is in units of ps. 89

A.1 List of rotational constants, polarizabilities and spin statistics for different linear molecules. Rotational constants are in units of cm^{-1}, polarizabilities are in atomic units. In addition, the perpendicular and parallel components of the first order hyper-polarizability of CO are $\beta_{\parallel}$=29.9 and $\beta_{\perp}$=7.9 in atomic units. 131

A.2 List of rotational constants, polarizabilities and spin statistics for symmetric top and asymmetric top molecules. Rotational constants are in units of cm^{-1}, polarizabilities are in atomic units. A, B and C correspond to the fastest axis, intermediate axis and the slowest axis, x, y and z are the corresponding polarizabilities. 132

A.3 List of hyper-polarizabilities for different molecules, values for N_2 are in atomic units and the other two are in units of 10^{-36} esu. 132

C.1 List of coefficients obtained from fitting harmonic delay scans. 138

C.2 List of coefficients obtained from fitting harmonic angle scans. 138

Acknowledgments

First, I would like to thank my PhD advisor, Dr. Vinod Kumarappan, who been very patiently guided me through my PhD. I would like to thank him for teaching me step-by-step how to set up a research lab and how to align laser beams. I will always remember all the hours he spent in the lab with me, teaching me basic skills such as aligning two irises during my first year. I appreciate every discussion with him. No matter what level of question I asked, he always explained without indignation until I understood. His enthusiasm for research inspired me to enjoy every hour's work in the lab and pursue better understanding of every physics problem.

I would also like to thank my lab mate—Varun Makhija, who has been a great person to work with. His broad knowledge and deep understanding of physics always helped me when I got confused about my work. I appreciate all the time we spent together in the lab, discussing how the experiments work, fixing LabVIEW programs, tuning the laser and more. My special thank to him for proof reading my thesis and spending numerous hours correcting it. I would like to thank him more as a friend, who has been always supportive during the hard times of my life.

My sincere thanks to Dr. Carlos Trallero as well. I enjoyed collaborating with him in the high harmonic generation experiment. Without the support from him and his group members Jan Tross and Sudipta Mondal, the harmonic experiment would not have been possible.

I'd like to thank all my thesis committee members Dr. Carlos Trallero, Dr. Itzik Ben-Itzhak, Dr. Brett Esry, Dr. Sanjoy Das and the outside chair, Dr. Dale Schinstock for their time spent correcting my thesis. My special thanks to Dr. Brett Esry, who has been very carefully reading and polishing this document till the moment of submission.

Many thanks to the former KLS group members Dr. He Wang, Dr. Hiroki Mashiko, Dr. Baozhen Zhao and Dr. Kun Zhao for teaching me about the KLS laser system.

I would like to sincerely thank Dr. Anh-Thu Le for performing QRS calculations for the HHG measurement and Dr. Cheng Jin for discussions about the HHG experiment.

Of course, without the support from Al Rankin, Mike Well, Scott Chainey, Bob Krause, Vince Needham and Kevin Carnes, all the experiments would not not have been possible.

I'd like to thank all the people I worked with in the lab. Jan Tross and Sudipta Mondal for the HHG experiments; Hui Li for the orientation experiment; Kelsie Betsch, Mohammad Zohrabi and Nora Kling for teaching me about the PULSAR system. Special thanks to Dr. Matthias Kling for discussions and collaboration on the orientation experiment.

I also want to thank Matthew Rothfuss, who has been a great friend and lab mate, for always being very helpful in the lab and providing movies to watch during data collection.

At last but not least, I'd like to thank all my friends for supporting me during my PhD: Junliang Xu, Wei Cao, Shun Wu, Matthew Rothfuss, Christian Madsen, Adrian Madsen, Wes Erbsen, Shou Zeng, Aram Vajdi and many more. Without your support, I would not be able to come this far.

This work was supported by the Chemical Sciences, Geosciences, and Biosciences Division, Office of Basic Energy Sciences, Office of Science, U.S. Department of Energy.

Chapter 1

Introduction to laser induced molecular alignment

1.1 Background

Laser induced molecular alignment has developed rapidly over the last two decades [1]. The goal is to use non-resonant laser pulses to fix molecular axes (in a gas-phase target) to the laser polarization axes so that experiments can be performed close to the molecular frame (MF). This is important since experiments performed in the MF are not averaged over the molecular axes distribution, which can "blur" the outcomes. Information with more angular resolution can be obtained from the MF measurements.

The definition of the molecular and lab frame (LF) are shown in Fig. 1.1. Throughout this thesis, the LF and MF are denoted by (X, Y, Z) and (x, y, z) axes, respectively. The LF is defined by the laser, with X and Z defined as laser polarization directions and Y as the laser propagation direction. The MF x, y, z axes represent the slowest, intermediate, and fastest axes about which molecule will rotate. Our goal is to bring the LF as close as possible to the MF. The possible alignment and orientation scenarios are depicted in Fig. 1.1 using the asymmetric top molecule 3,5-difluoro-iodobenzene (DFIB). In the case of no alignment, the molecular (x, y, z) axes are pointing in random directions. By confining molecular z axis with the lab Z axis, 1D alignment (1DA) can be achieved, but the x and y axes remain randomly oriented and there is no distinction between the positive and negative

Z direction. The x and y axes of this molecule can be further confined to the corresponding X and Y axes resulting in 3D alignment (3DA). Further, the symmetry between the positive and negative Z directions can be removed by orienting the molecules.

There are two conventional ways of characterizing the degree of alignment. First, in the direction cosines representation, $\langle\cos^2\theta_{xX}\rangle$, $\langle\cos^2\theta_{yY}\rangle$ and $\langle\cos^2\theta_{zZ}\rangle$ quantify the proximity of each individual MF axis to its corresponding LF axis [2, 3], where θ_{xX}, θ_{yY} and θ_{zZ} are angles between x and X axes and so on (these angles are not shown). Second, in the Euler angle representation $\langle\cos^2\theta\rangle$, $\langle\cos^2\phi\rangle$ and $\langle\cos^2\chi\rangle$ quantify alignment [4, 5], where θ, ϕ and χ are illustrated in Fig. 1.1. $\langle\cos\theta\rangle$ is used to quatify orientation. In this thesis, the direction cosine representation is chosen to characterize alignment and orientation.

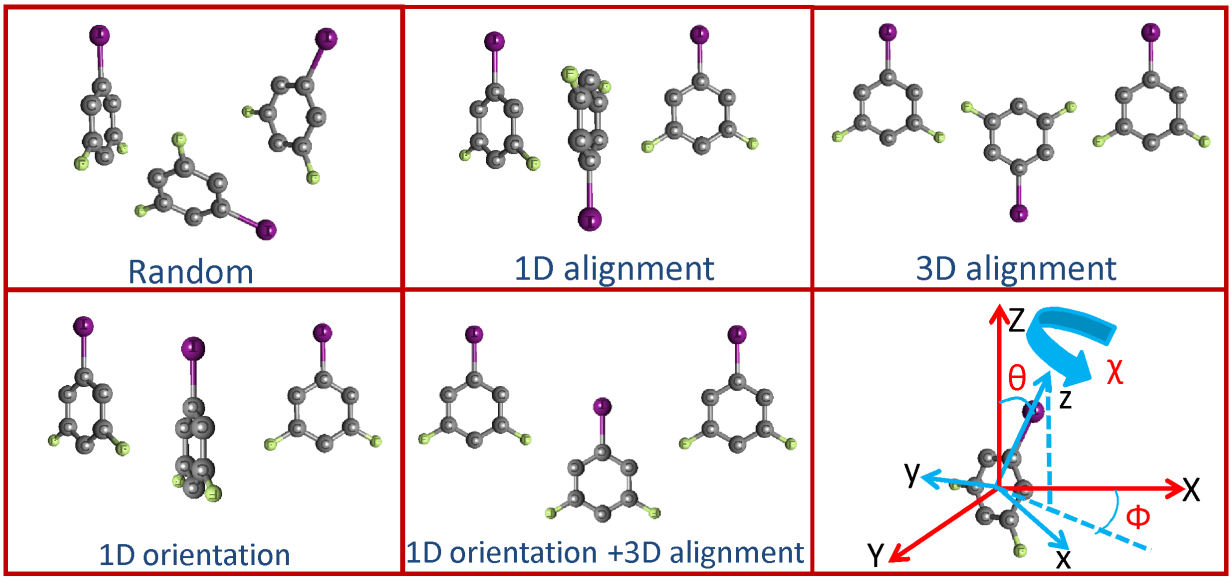

Figure 1.1: *Demonstration of different kinds of alignment and orientation on 3,5-Difluoro-iodobenzene molecules as well as the definition of molecular and lab frames. See text for details.*

There are mainly two categories of laser induced molecular alignment: geometric alignment and dynamic alignment [6]. The former is simply the alignment in the fragment distribution due to selective ionization. The latter requires a non-ionizing laser pulse to torque the molecules and drive them towards the laser polarization direction. In this thesis,

we are particularly interested in dynamic alignment which provides an aligned molecular ensemble that can be used for further experiments. There are two types of dynamic alignment — adiabatic alignment and impulsive alignment. When the laser pulse duration τ is much larger than the molecule's rotational period — $1/2B$ for a linear molecule with rotational constant B — the induced alignment is adiabatic. Conversely, if $\tau \ll 1/2B$, the induced alignment is impulsive and occurs after the pulse has passed and is hence field-free alignment. Both scenarios were predicted and studied theoretically in 1995 by Friedrich and Herschbach [7] and Seideman [8].

In the case of 1DA, the first adiabatic 1DA experiment was carried out by Larsen *et al.* in 1999 [9], in which a yttrium aluminum garnet (YAG) laser with nanosecond pulse duration (full width at half maximum in intensity) was used to align several different molecules such as I_2, CH_3I and C_6H_5I. A value of $\langle\cos^2\theta_{2D}\rangle$ above 0.8 was achieved for most of the molecules, measured using a velocity map imaging (VMI) spectrometer, where θ_{2D} is evaluated from the 2D images recorded by a camera (more detail will be given in Chap. 2). Adiabatic alignment tends to give very good alignment provided the molecules are rotationally cold. The highest degree of alignment achieved so far, $\langle\cos^2\theta_{2D}\rangle$=0.97, was reported by aligning state-selected iodobenzene molecules [10]. However, since the optimum alignment always happens at the peak of the laser pulse, many further experiments will be affected by this aligning laser field. For example, in situations involving back scattered electrons, such as high harmonic generation (HHG) [11, 12] and non-sequential double ionization [13, 14] processes, such an external field will certainly affect the electronic trajectories and complicate the experimental results. That is the reason why more and more work is focused on using short laser pulses to get field-free alignment. All the work present in this thesis will also be focused on field-free alignment. In the field-free alignment experiment carried out in 2001 [15], picosecond laser pulses were used to impulsively align I_2 molecules and strong-field alignment revivals were observed for the first time. Impulsive alignment occurs via the excitation of numerous angular momentum states resulting in a rotational wave packet

which, for linear and symmetric top molecules, periodically re-phases since the rotational energies of such molecules are regularly spaced. The best field-free alignment achieved so far is $\langle \cos^2 \theta_{2D} \rangle$=0.83 in rotationally cold iodobenzene molecules [16]. In both the adiabatic and impulsive cases, the keys to better alignment are fewer initial incoherent rotational states and a large number of coherently populated rotational states, which corresponds to lower initial rotational temperature and larger laser fluence as long as no vibrational or electronic excited states are populated.

In the case of 3DA, a majority of the work has been focused on adiabatic 3DA. This goal was achieved by using either one elliptically polarized nanosecond YAG laser pulse [17] or a combination of a linearly polarized nanosecond YAG laser pulse with a perpendicularly polarized femtosecond infrared (IR) laser pulse [18]. Even though good 3DA can be achieved, field-free three dimensional alignment (FF3DA) is still required for certain experiments due to the reasons described previously. Disappointingly, to date, limited work has been done to explore FF3DA and possible ways of enhancing it. For example, using two orthogonally polarized time delayed femtosecond IR pulses [19] or a single elliptical polarized femtosecond IR pulse [20]. Both provide a FF3DA level slightly above the isotropic value. More detail will be given in Chap. 3.

The goal of molecular orientation was initially achieved without utilizing a laser field. A hexapole state selector [21] or a strong electric field [22] can fulfill the task, but both have certain limitations. Laser induced orientation was initially achieved adiabatically and later extended to the field-free regime. The adiabatic case requires a strong laser field and a moderate DC electric field [23], whereas the field-free case uses few or single cycle terahertz pulses [24] or phase synchronized fundamental and second harmonic pulses [25]. Experimentally, the degree of field-free orientation reported is still under 0.1 for $\langle \cos \theta \rangle$ [26]. More detail will be given in Chap. 6.

In terms of applications, a large majority of work has been focused on attaining field-free one dimensional alignment (FF1DA) of simple linear molecules, which serves the needs for

further experiments on these systems. There is also a large amount of work on attaining FF1DA for asymmetric top molecules; however, very few further experiments have been performed either due to experimental constraints or the difficulties of interpreting and simulating the complicated system. Only in recent years has some work been carried out, such as high harmonic generation from 1D aligned allene molecules [27]. There are also a few reports on field-free three-dimensional alignment (FF3DA) for asymmetric top molecules [19, 20], which will provide even more information in further experiments. Unfortunately, this still remains a challenge for the whole field since only poor FF3DA can be achieved. Due to the challenge of achieving good field-free orientation, harmonic generation experiments on oriented CO molecules have only recently been reported [28].

For example, the technique of alignment can be used for imaging isolated molecules. A high energy electron beam [29] or X-ray beam [30] can be impinged on a gas target and due to the large scattering cross section of electrons and atoms, a diffraction pattern will form in the far field containing information about the molecular structure. Only the internuclear distances can be extracted from the diffraction pattern if the molecules are randomly oriented. However, when the molecular axes are fixed in space, the diffraction pattern will contain information about the bond angle of the molecule as well. Position of the atoms can be retrieved and the precision of the retrieved information is dependent on the degree of alignment that can be obtained. The first experiment was demonstrated by Hensley *et al.* [29], in which a CF_3I molecule is aligned and imaged.

Aligned molecules can also be used for imaging molecular orbitals. Different orbitals of the molecule will have very different angular dependence. For instance, in nitrogen molecules, for the outermost σ_g electron orbital, the probability of finding an electron along the N-N bond axis (0 degrees) is much larger than that along the perpendicular axis (90 degrees). However, for the next orbital, π_u, the probability peaks at 90 degrees. In the case of oxygen molecules, for the outermost orbital π_g, the probability peaks around 45 degrees. Therefore, it is necessary to align the molecules so that different orbitals can be identified

and extracted in the measurement. So far, orbital structure has been successfully extracted experimentally for molecules such as N_2 [31], CO_2 [32, 33]. The dependence of harmonic generation on the alignment angle of polyatomic molecules has also been shown to follow the structure of the outermost orbital [27].

Since the electron density distribution is very angle dependent, the study of strong-field ionization can also benefit from aligned molecules. Photoelectron angular distributions in the multi-photon regime [34] and angle dependent ionization rates in the tunneling regime [35] have been successfully measured experimentally. The former yields the electron angular dependence for different multiphoton ionization channels. The latter maps the contribution of different molecular orbitals.

Upon removal of one electron, in the presence of a laser field, the electron can be driven back to collide with the parent ion. The structure of the molecules that the electron "sees" when it recollides may be different from when it ionizes. If the molecules are fixed in space, molecular dynamics such as bond lengths or bond angles changing can be probed to better precisions [36, 37].

There are many other measurements that will benefit from using aligned molecules. Some of these experiments have been successfully demonstrated with simple molecules in the last few years. Extending these to more complex molecules remains challenging due to either the lack of techniques providing highly aligned samples in multi-dimensions or other technical difficulties. This motivates the search for more efficient alignment schemes with the purpose of providing highly aligned molecular targets for future investigations.

This thesis details our contributions to this field. FF1DA, FF3DA, FF1D orientation and further experiments will be discussed. A breakthrough significantly enhancing FF3DA and an experimental demonstration of increasing orientation levels will be described. High harmonic generation from highly aligned linear molecules will be demonstrated as an application of FF1DA.

1.2 Theoretical treatment of field-free one dimensional alignment

Under the rigid rotor approximation [1], when a multi-cycle laser pulse interacts with a molecule, any contribution from the molecule's permanent dipole will be averaged out because the laser electric field changes direction every half cycle. It is the induced dipole that mediates the interaction since the direction of the induced dipole changes with the direction of the electric field. The total Hamiltonian can then be expressed as

$$\hat{H}_{\text{total}} = \hat{H}_{\text{rot}} + \hat{V} = \hat{H}_{\text{rot}} - \frac{1}{4}\sum_{i,j} \alpha_{ij} E_i E_j, \tag{1.1}$$

where H_{rot} is the field-free Hamiltonian, V is the interaction potential, α_{ij} are the polarizability tensor elements in the lab frame with $i, j = X, Y, Z$, and E is the laser electric field. The total Hamiltonian H_{total} varies depending on the type of molecules that are interacting with the laser. The different types — linear molecules, symmetric top molecules and asymmetric top molecules — will be discussed individually in the following sections.

1.2.1 Linear and symmetric-top molecules

For linear molecules interacting with a linearly polarized laser pulse, the total Hamiltonian can be written as

$$\hat{H}_{\text{total}} = B\hat{J}^2 - \frac{E_o(t)^2}{4}(\Delta\alpha \cos^2\theta + \alpha_\perp), \tag{1.2}$$

where $B = 1/2I$ is the rotational constant, I is the moment of inertia, $\hat{J}$ is the angular momentum operator, $E_o(t)$ is the time-dependent electric field envelope, $\Delta\alpha$ is the polarizability anisotropy—the difference of the polarizabilities parallel and perpendicular to the molecular axis — $\alpha_\parallel - \alpha_\perp$. The basis set that describes the rotational states will be the spherical harmonics $|JM\rangle$, where M is the projection of the angular momentum J onto the LF Z axis. If the laser pulse is linearly polarized the system has cylindrical symme-

try and M is conserved. For each initial thermal populated state, we can write down the time-dependent Schrödinger equation (TDSE) for the wavefunction $|\psi(t)\rangle$,

$$\left[B\hat{J}^2 - \frac{E_o(t)^2}{4}(\Delta\alpha\cos^2\theta + \alpha_\perp)\right]|\psi(t)\rangle = i\partial_t\,|\psi(t)\rangle\,, \tag{1.3}$$

where $|\psi(t)\rangle = \sum_{J'} C_{J'M}(t)\,|J'M\rangle$, $C_{J'M}(t)$ are the time-dependent coefficients of each state. Projecting the Schrödinger equation onto a state $|JM\rangle$, and taking into account that

$$\hat{J}^2\,|JM\rangle = J(J+1)\,|JM\rangle \tag{1.4}$$

we get,

$$\partial_t C_{JM}(t) = -iC_{JM}(t)\left[BJ(J+1) - \frac{E_o(t)^2}{4}\alpha_\perp\right] + i\frac{E_o(t)^2}{4}\Delta\alpha\sum_{J'} C_{J'M}\left\langle JM|\cos^2\theta|J'M\right\rangle. \tag{1.5}$$

The term $\langle JM|\cos^2\theta|J'M\rangle$ gives the selection rules for J. $\cos^2\theta$ can be rewritten using Wigner d-matrices $d^j_{m'm}$,

$$\cos^2\theta = \frac{2}{3}d^2_{00} + \frac{1}{3}. \tag{1.6}$$

Using the coupling equations [3.97] and [3.119] given by Ref. [38], we can get

$$\left\langle JM|\cos^2\theta|J'M\right\rangle = \sqrt{\frac{(2J'+1)(2J+1)}{4\pi}}\begin{pmatrix} J & 2 & J' \\ 0 & 0 & 0 \end{pmatrix}\begin{pmatrix} J & 2 & J' \\ M & 0 & M \end{pmatrix}, \tag{1.7}$$

since the $\cos^2\theta$ interaction couples rotational states with the same parity, therefore, the selection rules for J are $\Delta J = 0, \pm 2$. Assuming a maximum value for J, which depends on the initial population and the intensity of the laser pulse, we can calculate the transition matrix before propagating the wavefunction in the laser field. The value of the maximum J is determined such that by adding one extra J state, the calculated values of $\langle\cos^2\theta\rangle$ change by less than 1×10^{-5} relatively. In the field, a Runge-Kutta method with adaptive step

size [39] is used to solve the differential equations numerically with an absolute tolerance of 1×10^{-10}. At each time step, an array of the coefficients is obtained, whose square gives the population of the corresponding J state. Once we get the wavefunction $|\psi(t)\rangle$, we can calculate the expectation value $\langle\cos^2\theta\rangle(t)$ to quantify the alignment in the laser field for each initial state.

After the laser pulse, the evolution of the wavefunction can be calculated by solving the TDSE for the field-free Hamiltonian,

$$|\psi(t)\rangle = \sum_{J'} C_{J'M}(t_e)\,|J'M\rangle \exp\big[-iE_{J'}(t-t_e)\big], \tag{1.8}$$

where t_e is the time corresponding to the end of the laser pulse and $E_{J'}$ are the eigenvalues of the field-free Hamiltonian.

In order to get the alignment trace for the molecules with an initial rotational temperature, each initial state is thermally weighted by ω_i, assuming a Boltzmann distribution

$$\omega_i = g_i \frac{\exp(-E_i/k_BT)}{\sum_j \exp(-E_j/k_BT)}, \tag{1.9}$$

where g_i and E_i are the nuclear spin statistical weight and field-free eigenvalues of the i^{th} initial state respectively, k_B is the Boltzmann constant, and T is the initial rotational temperature. In order to estimate the number of initial thermally populated rotational states for a given temperature, the partition function is calculated by continually adding the Boltzmann factors of successive J states until the change in the function is less than 1×10^{-5}. Then, the initial number of rotational states is estimated by adding the thermal populations of successive J states until the sum is larger than 0.999. At last, the partition function is recalculated by including those initial states. By propagating the initial states separately, $\langle\cos^2\theta\rangle(t)$ can be evaluated for a given molecule at a given initial rotational temperature. Fig. 1.2 shows some examples for the alignment of N_2, O_2, CO_2 and N_2O molecules.

We can see from the figure that besides the initial alignment, there are periodic recur-

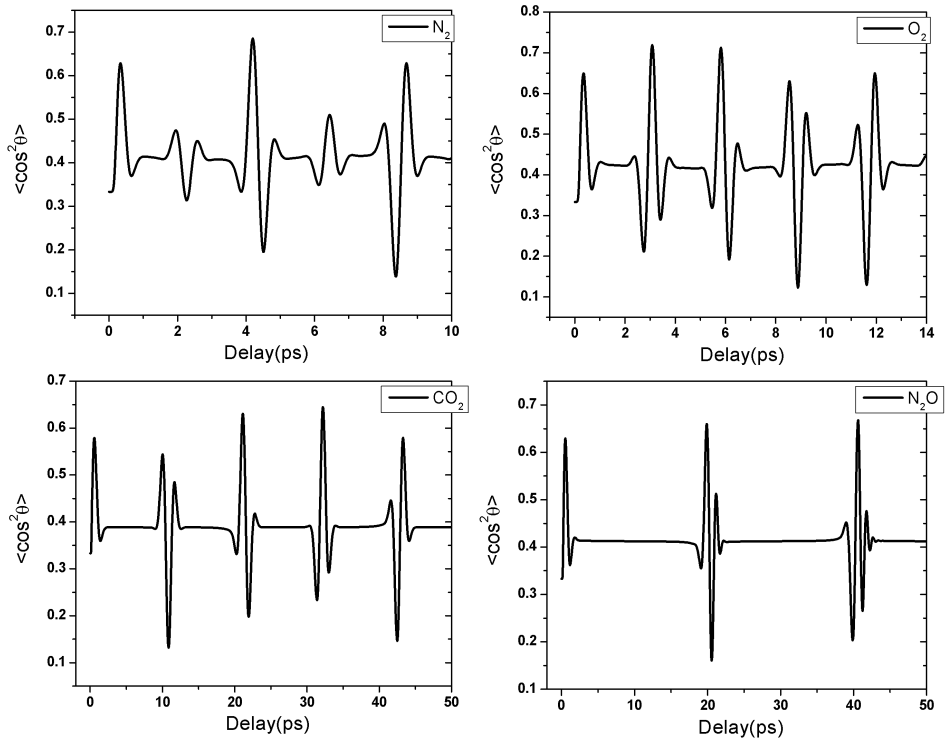

Figure 1.2: *TDSE calculations of the alignment traces for four molecules with different spin statistics. One full revival period is shown for all the molecules. A rotational temperature of 30 k is assumed for all molecules and the laser parameters are chosen to be 80 fs, 50 TW/cm^2, reproduced from Fig. 3.4 of [40].*

rences of the alignment, some of which are stronger than the initial peak. These are the previously mentioned rotational revivals. Depending on the nuclear spin statistics, different molecules will have different revival structures. For example, N_2 has revivals at 1/4 of the rotational period which are small compared to half and full revivals. O_2 and CO_2 have big quarter revivals but in opposite directions. N_2O does not have quarter revivals. To explain this, we can take a close look at the expectation values of $\cos^2\theta$ for the field-free hamiltonian. From Eq. 1.8, we get

$$\left\langle \cos^2\theta \right\rangle (t) = \sum_{J',J} C^*_{J'M}(t) C_{JM}(t) \exp\left[i(E_{J'} - E_J)(t - t_e) \right] \left\langle J'M \right| \cos^2\theta \left| JM \right\rangle . \qquad (1.10)$$

The phase term is $\phi = (E_{J'} - E_J)(t - t_e) = 2\pi B[J'(J'+1) - J(J+1)](t - t_e) = 2\pi B(J' -$

$J)(J'+J+1)(t-t_e)$. Because of the selection rule, $J'-J=\pm 2,0$, we have $\phi = 2\pi 2B(2J+3)t'$ or $-2\pi 2B(2J-1)t'$ ($J'-J=0$ adds a constant to the baseline, we use t' for $t-t_e$). Since the rotational period equals 1/2B and the phase is $n\pi$ at $t' = n/4B$, n=0,1,2,3..., there will always be coherent addition of all the states at integer multiples of half the rotational period. This causes the half and full revivals seen in Fig. 1.2. At $t' = 1/8B$, even and odd J states will be exactly out of phase. Therefore, the structure at quarter revivals will depend on the spin statistical weights of the even and odd J states. For N_2, the ratio of even and odd states is 2:1, which cancels out part of the quarter revivals, resulting in a smaller revival. While for O_2 and CO_2, only even or only odd states contribute, making the quarter revivals large but in opposite directions. For N_2O, even and odd states are equally weighted, and thus the quarter revivals cancel out completely, leaving only half and full revivals. (Spin statistics for the molecules considered in this thesis are given in App. A). So, structure of fractional revivals can be a useful tool for examining the symmetry of the rotational states [41] and more will be discussed in later chapters.

Symmetric top molecules are quite similar to linear molecules in the sense that the interaction only results in transitions between J states. The differences are in the field-free Hamiltonian. The basis set describing the rotational states for symmetric-top molecules is the Wigner D functions $|JKM\rangle$, where the extra quantum number K is the projection of the angular momentum onto the MF z axis. Since the interaction does not depend on angle χ, the angle of the rotation of the molecule about its own z axis, K is conserved.

In order to write down the field-free Hamiltonian and its eigenvalues, we need to specify the type of symmetric top in question. In general, the field-free Hamiltonian can be expressed as

$$\hat{H}_{\text{free}} = \frac{J_x^2}{2I_{xx}} + \frac{J_y^2}{2I_{yy}} + \frac{J_z^2}{2I_{zz}} = AJ_x^2 + BJ_y^2 + CJ_z^2, \tag{1.11}$$

where J_x, J_y and J_z are projections of the angular momentum about the molecular (x, y, z) axes. I_{xx}, I_{yy} and I_{zz} are moments of inertia, and A, B and C are rotational constants

of each axis. For symmetric top molecules, two of the three axes are identical. If these two axes are fast axes and $I_{xx} = I_{yy} < I_{zz}$, the molecule is referred to as an oblate top. For prolate tops, $I_{xx} < I_{yy} = I_{zz}$. The field-free Hamiltonians and eigenvalues for both types are as follows [38],

Oblate top:

$$\hat{H}_o = A\hat{J}^2 + (C - A)J_z^2 \tag{1.12}$$

$$E(J, K) = AJ(J + 1) + (C - A)K^2 \tag{1.13}$$

Prolate top:

$$\hat{H}_p = C\hat{J}^2 + (A - C)J_z^2 \tag{1.14}$$

$$E(J, K) = CJ(J + 1) + (A - C)K^2. \tag{1.15}$$

We can then solve the TDSE following the same steps as discussed above for linear molecules except that now the selection rules for the observable $\langle \cos^2 \theta \rangle$ are $\Delta J = 0, \pm 1$ and ± 2. Fig. 1.3 shows an example of the calculated alignment trace from the oblate top benzene. The polarizabilities $\alpha_{\parallel}$ and $\alpha_{\perp}$ of the molecule are calculated using $\alpha_{\parallel} = (\alpha_{xx} + \alpha_{yy})/2$ and $\alpha_{\perp} = \alpha_{zz}$, where α_{xx}, α_{yy} and α_{zz} are the diagonal elements of the molecular polarizability tensor.

Note that initially $\langle \cos^2 \theta \rangle$ decreases instead of increasing as in Fig. 1.2. This is because for benzene, the symmetry axis (in this case, the axis perpendicular to the plane of the benzene ring) is the least polarizable axis, while the laser pulse aligns the most polarizable axis of the molecule. The symmetry axis will therefore initially be driven away from the laser polarization axis, and as a result, $\langle \cos^2 \theta \rangle$, where θ is defined as the angle between the symmetry axis of the molecule and the laser polarization axis, will decrease below the isotropic value 1/3 [42].

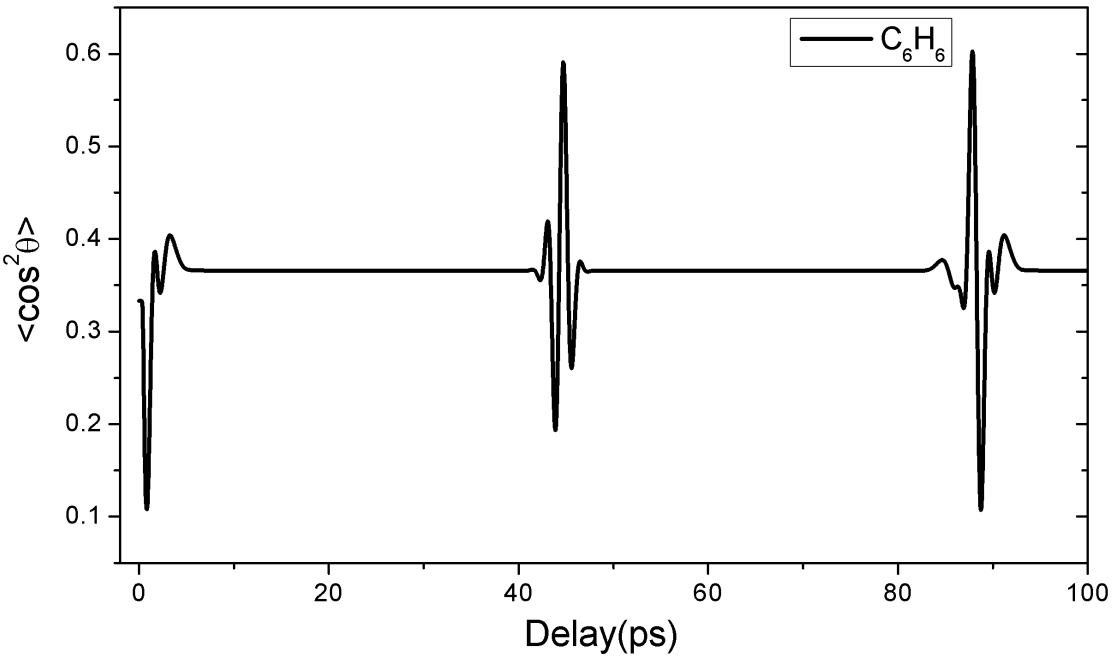

Figure 1.3: *Calculated alignment trace for 30 K benzene molecules for a 130 fs and 15 TW/cm^2 laser pulse.*

1.2.2 Asymmetric-top molecules

In Eq. 1.11, if a molecule has $I_{xx} \neq I_{yy} \neq I_{zz}$, it is an asymmetric top molecule. TDSE calculations for this type of molecule can be very hard and time consuming and will only be briefly introduced here. The code for asymmetric top TDSE was written by Varun Makhija, who also performed all the computations for such molecules..

Unlike linear and symmetric top molecules, the field-free eigenfunctions of asymmetric tops do not have an analytical form. However, they can be written in the symmetric top basis:

$$|\psi(t)\rangle = \sum_{J',K'} C_{J',K'}(t)\,|J'K'M\rangle\,. \tag{1.16}$$

Diagonalizing the matrix calculated using Eq. [6.65∼6.69] from Zare [38] and sorting the energy for each J state in ascending order, we get a set of eigenvalues in the $|J\tau M\rangle$ basis, where τ labels the energy levels and ranges from -J to J.

For molecules with the polarizability and moment of inertia tensor diagonalized in the same coordinate system, the interaction potential can be written as:

$$\hat{V} = -\frac{E^2}{4}\left[\sin^2\theta(\alpha_{xx}\cos^2\chi + \alpha_{yy}\sin^2\chi) + \alpha_{zz}\cos^2\theta\right], \tag{1.17}$$

where $\alpha_{xx}, \alpha_{yy}, \alpha_{zz}$ are the diagonal elements of the polarizability tensor of the molecule. Using Eq. 1.17 in the TDSE gives the following equation for the $C_{J,K}$s

$$\partial_t C_{JK}(t) = -i\sum_{J',K'} C_{J',K'}(t)\left[\left\langle J'K'M|\hat{H}_{\text{free}}|JKM\right\rangle \delta_{J,J'} + \left\langle J'K'M|\hat{V}|JKM\right\rangle\right]. \tag{1.18}$$

The matrix elements for $\hat{H}$ and $\hat{V}$ can be written analytically in the $|JKM\rangle$ basis [38], following which the above set of differential equations can be solved numerically. Following the laser pulse, the wavefunction is transformed to the $|J\tau M\rangle$ basis and propagated in time using the field-free eigenvalues. Fig. 1.4 shows $\langle\cos^2\theta\rangle(t)$ for a thermal distribution of iodobenzene molecules at 1 K.

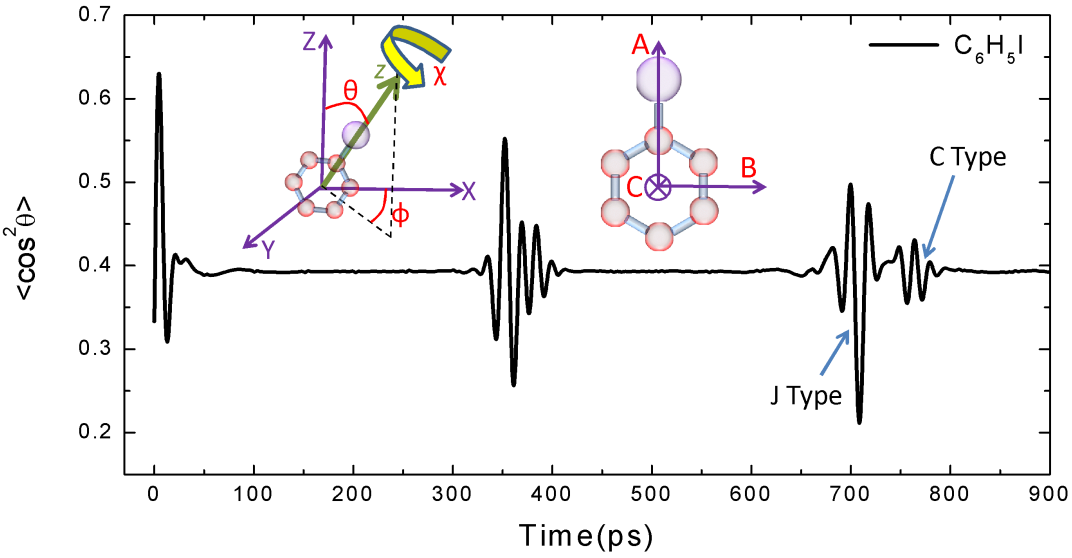

Figure 1.4: *Calculation for iodobenzene molecules, at a rotational temperature of 1 K. 555 total initial states are populated and thermal averaged. The laser pulse duration is 140 fs and the intensity is 8 TW/cm², calculated by Varun Makhija.*

Revival type	Revival time	Selection rules	Iodobenzene
J-type	t$\approx n/2(B+C)$	$\Delta J = 1, 2; \Delta K = 0$	707.8 ps
K-type	t$\approx n/(4A-2B-2C)$	$\Delta J = 0; \Delta K = 2$	50.3 ps
Hybrid	t$\approx n/(2A-B-C)$	$\Delta J = 0; \Delta K = 1$	100.7 ps
C-type	t$\approx n/4C$	$\Delta J = 2; \Delta K = 0$	754.7 ps
A-type	t$\approx n/4A$	$\Delta J = 2; \Delta K = 2$	44.1 ps

Table 1.1: *List of different type of revivals and corresponding selection rules for asymmetric top molecules, the formulas for calculating the revival time and the numbers for iodobenzene molecules are given.*

Since the energy levels of an asymmetric top molecule are not regularly spaced, the revival trace is not periodic. However, subsets of energy levels are regularly spaced and result in approximately periodic revival traces. Such revivals are named J-type, K-type, Hybrid-type, C-type and A-type depending on which rotational coherences are involved [43]. C- and A-type revivals can be thought of as rotations about the molecular C and A axes. All the other revivals involve rotation about all three molecular axes. Selection rules for different types and the approximate periods of these revivals based on the subsets of approximately regular energy levels for iodobenzene are shown in Tab. 1.1.

Since both J and τ quantum numbers are involved in the transitions, the size of the Hamiltonian matrix that needs to be solved is $J^2 + 2J$, as more and more J states are populated—resulting in better alignment—the amount of time needed for the simulation increases significantly. At the same time, energy spacing scales with the molecular rational constant, which is inversely proportional to the moments of inertia. Therefore, for heavy asymmetric tops such as iodobenzene, even at 1 K, over 500 initial states are thermally populated. A calculation for an effective aligning pulse will easily take one day. Therefore, a few tricks are worth exploring to reduce the computation time. For example, because positive and negative K states give the same interaction matrix elements, only positive K states are needed for constructing the interacting matrix [30]. This will reduce the time by at least a factor of 2. Furthermore, performing calculations for different initial states in parallel will also reduce the calculation wall-time.

1.3 Improving molecular alignment

The ultimate goal of aligning molecules is to bring the molecular axes as close to the lab frame axes as possible. As previously mentioned, there are mainly two ways of increasing the degree of alignment. One is to reduce molecular rotational temperature, and the other is to increase laser fluence.

The molecular rotational temperature can be cooled using a high pressure supersonic gas jet. A kHz Even-Lavie pulsed valve [44] is used for our experiments. About 70 atmosphere backing pressure of helium gas is used to carry out the target molecules through a 0.1 mm orifice of the gas jet into a vacuum with 10^{-7} torr background pressure. When operating at 1 kHz, with such a high backing pressure, a short opening time and high pumping capacity are required. In our case, with an 8 μs jet opening time, a 2500 L/s turbo pump is needed to maintain a chamber pressure of 10^{-5} torr. Because of the huge pressure difference on the sides of the small orifice, helium gas gets accelerated in the vacuum to a velocity of about 1780 m/s at room temperature [44]. As the initial thermal energy of helium is converted to translational kinetic energy of the jet, collisions between the helium atoms and the target molecules also result in the reduction of the internal (vibrational and rotational) energy of the molecules. Rotational temperature around 1 K for heavy molecules such as iodobenzene can be obtained. For lighter molecules, carbon monoxide for example, when mixed with helium gas, rotational temperatures below 5 K are accessible. However, below a certain temperature limit, clusters of target molecules and helium atoms will start to form and prevent further cooling. Even without seeding in carrier gases (helium, neon and so on), supersonic expansion of a gas sample can also cool the rotational temperature of the molecule to some extent, for instance, neat nitrogen can be cooled to about 10 K. However, for some molecules, backing pressure needs to be much lower in order to prevent clustering. An additional state selector or deflector [45] can further bring the temperature down to sub-kelvin regime. The underlying principle is that a strong inhomogeneous electric field stark shifts the rotational energy levels, dispersing different states spatially. By selecting different

parts of molecular beam to probe, molecules with sub-kelvin rotational temperature can be studied.

Improving alignment by increasing the laser fluence has the limitation that the laser intensity should not cause any vibrational or electronical excitations. Furthermore, it has been shown that the degree of alignment that can be achieved by using a single intense ultrashort laser pulse is limited [46]. Initially, pulse shaping experiments were performed to seek complex pulse shapes in order to enhance the alignment. Later on, a multipulse scheme was proposed to overcome this limit by dividing the too intense laser pulse into two pulses or even several pulses. The first pulse initiates the rotational wave packet and the following pulse kicks the molecules again at the rephasing or revival times to populate more coherent rotational states—thus squeezing the molecular angular distribution. This scheme has been proved to be very effective. For example, in an experiment performed by Bisgaard *et al.* [47], it has been shown that with the same pulse duration and total intensity, splitting the aligning pulse into two time separated pulses can increase the degree of alignment from $\langle \cos^2 \theta \rangle = 0.57$ to 0.66 for rotationally cold iodobenzene molecules. It also shows that the optimum conditions are: (1) the second pulse kicks right at the alignment peak of the first pulse; (2) the second pulse is three times more intense than the first one. In another experiment reported by Cryan *et al.* [48], eight femtosecond laser pulses are used to repetitively kick room temperature nitrogen gas at full rephasing times and the $\langle \cos^2 \theta \rangle$ value increases from about 0.4 to almost 0.7.

The calculation for multi-pulse alignment is relatively easy. The TDSE calculation for the first pulse is the same as previously explained, and the initial set of C_{JM} coefficients for each successive pulse is obtained after propagation through the interval between the pulses. A calculation is shown in Fig. 1.5 for aligning N_2 molecules using three pulses. As is evident this technique works very well for boosting the degree of alignment. In the later chapters of this thesis, multi-pulse alignment will be used extensively for enhancing FF1DA and inducing and enhancing FF3DA.

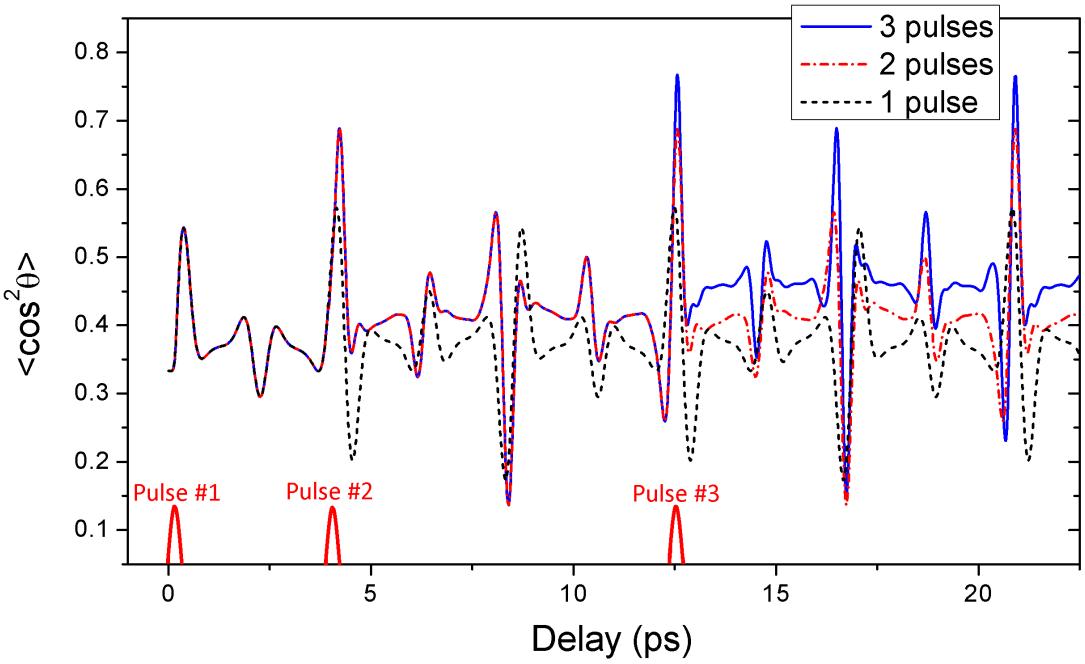

Figure 1.5: *30 K N_2 molecules are aligned by three 80 fs, 30 TW/cm^2 laser pulses, first pulse comes at t=0 ps, revival trace is shown in black dash line. Second pulse comes at t=3.94 ps, right at the rising edge of the half revival, the trace is shown in red dash dot line. The third pulse comes at t=12.3 ps, at the rising edge of the full revival after the second kick, the trace is shown in blue solid line.*

Chapter 2

A one kHz velocity map imaging spectrometer for measuring molecular alignment

2.1 Introduction

Since the development of velocity map imaging (VMI) [49] as a method to measure the momentum spectrum of charged particles, this technique has been widely used in atomic and molecular physics. Compared to other methods of measuring momentum distributions, for instance, cold target recoil ion momentum spectroscopy (COLTRIMS) [50, 51], which measures 3D momentum distribution for both ions and electrons of the target in a coincident manner, a VMI measurement does not record arrive time information. It measures an integrated momentum distribution along one momentum component and the spatial distribution for either ions or electrons sources, resulting in momentum distributions with a much higher count rate than the COLTRIMS measurement. Thus, VMI is very suitable for experiments in which only momentum information is needed, such as measuring molecular alignment. The fundamental idea is to use a non-uniform electric field as a "lens" to focus charged particles. A three metal plate configuration is the simplest design (see Fig. 2.1). By adjusting the high voltages on the first plate (the repeller) and the second plate (the extractor), we can tune the focus of the "lens" so that all the particles with equal initial momentum in the detector plane are focused to the same position on the detector. With

the use of a microchannel plate (MCP) detector to amplify the signal and a phosphor screen to convert the resulting electron pulse to visible light, two dimensional momentum distributions can be directly imaged using a camera. By determining the centroid of the light emission from the phosphor due to an individual detection event, it is possible to enhance the resolution of the detector well past the average width of the spot [52]. In addition, by using either the inverse Abel transform [53] or the inverse Radon transform [54], full three dimensional distributions can be extracted from the raw 2D images (more detail of this reconstruction will be given in Chap. 3).

Within the axial-recoil approximation [55] it is assumed that the molecule in question dissociates along the direction of its molecular bond. Therefore, the two dimensional momentum distribution of the fragment ions measured using VMI would directly reflect the molecular axes distribution, if the selectivity of the dissociating pulse can be minimized. A number of experiments use the axial-recoil approximation in conjunction with VMI to measure molecular alignment [9, 15, 18, 34, 45, 56–58]. A typical VMI image from aligned molecules is shown in Fig. 2.1, it is a 2D projection of the 3D momentum distribution onto the detector plane, from which we could measure $\langle \cos^2 \theta_{2D} \rangle$ to estimate the degree of alignment, where θ_{2D} is angle between laser polarization direction and the vector of each hit with respect to the image center. Note that $\langle \cos^2 \theta_{2D} \rangle$ has an isotropic value of $1/2$ instead of $1/3$ for $\langle \cos^2 \theta \rangle$.

2.2 A single shot one kHz system and analysis of the images

In experiments with kHz ultrafast lasers, the common practice is to use a Peltier-cooled high-resolution CCD camera to capture the integrated 2D momentum distributions. This method suffers from two disadvantages — the dynamic range of the measurement is limited by noise (either optical or in the camera), and the resolution is limited by the average width (in pixels) of the light distribution from the MCP-phosphor detector on the image intensifier

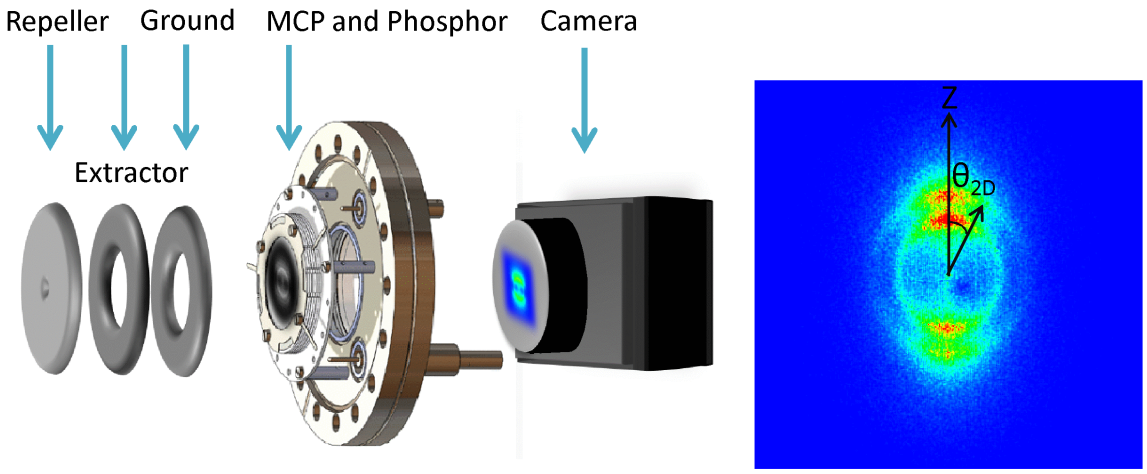

Figure 2.1: *VMI setup and a typical VMI raw image of I^+ ion from aligned DFIB molecules. The up-down asymmetry of the image is due to the difference of the gain efficiency at different positions on the detector.*

of the camera. When operating with high count rates, it is also easy to saturate the detector and hence lose information about the relative intensity distribution. These issues can all be addressed by single shot operation with centroid determination [52], in which each charged particle hit within every laser shot is thresholded and tagged by its position information, but working in this mode remains a challenge when the laser operates at 1 kHz. Another 1 kHz VMI that was simultaneously developed elsewhere [59] has used customized hardware, making it inconvenient to replicate and preventing widespread adoption. Therefore, we developed a simple implementation of a system capable of kHz single shot-operation (with a 500×500 pixel camera) with off-the-shelf components. The ease of implementation of this scheme should lead to its use widely in the atomic and molecular physics community.

The first requirement for a kHz detection system is a phosphor screen that has a lifetime less than 200 μs. This allows the signal from one laser pulse to decay to a sufficiently low level before the next pulse arrives so that there are no inter-pulse pile-up effects. We use a 40 mm diameter MCP with a P47 phosphor. The phosphorescence lifetime of P47 is 120 ns, which is substantially better than the minimum requirement. Even though the phosphor's quantum efficiency is lower than that of the commonly used P43, it is still not too low as

to be unusable for this purpose.

The second requirement is a camera that can take images at 1000 fps with sufficient efficiency and gain uniformity. We chose the Basler A504k (later on updated to a Basler acA2040-180km), a CMOS camera rated to operated at 500 fps with 1280×1024 pixel image size. When the image size is reduced to 500×500 pixels, the camera operates at 1000 fps. This is our mode of operation. The camera can be triggered externally, and gated to an exposure time as low as 2 μs. Even though the phosphor has a low enough lifetime that pileup is not an issue, it is nevertheless useful to reduce optical and electronic noise in the image by using the shortest acceptable exposure time.

Transferring data to a computer at a 1000 fps requires a fast bus and frame grabber. The Basler A504k uses dual-channel Cameralink connection to achieve 640 MB/s transfer rate. We use National Instrument's PCIe-1429 frame-grabber to connect to the camera. With a 4×PCIe bus, 8-bit image data can be transferred to the computer's RAM at the full 1 kfps rate.

Thus, this combination of phosphor, camera and frame-grabber is capable of handling the detection of VMI spectra at the required 1 kfps. Higher repetition rates can also be achieved at the cost of a smaller image size.

With 8-bit, 500×500 pixel frames and 1 kfps acquisition rate, the computer must handle 250 MB of raw image data per second. There are two possible ways of handling this: write the raw data to hard drives and process it off-line, or analyze each individual image for detection events in real-time and write only the location of each particle hit to the hard drive. The former requires very fast, large capacity hard-drives, and provides no feedback while the experiment is running. The latter requires a fast computer running an efficient algorithm, capable of analyzing individual images in less than 1 ms. We chose the latter option both due to the challenges involved in writing data at such high rates and for the real-time feedback it provides.

An image-analysis algorithm must satisfy several requirements. In addition to being

fast enough, the algorithm needs to identify individual events while discriminating against noise in the image and trying to distinguish single particle hits from double (or more) hits (constituting in intra-pulse pile-up's, which must be avoided if saturation effects are to be minimized), and calculate the centroid of each hit with the highest accuracy possible. Intra-pulse pile-up cannot be completely removed - there is always the possibility of two particles hitting the same channel of the MCP detector, especially when it is desirable to count hundreds of events per laser shot in order to measure a momentum distribution with high statistics. Since the detector is operating in the counting or saturation mode, pulse height measurements cannot distinguish such double hits from single events. Nevertheless, it is often the case that the overlap of light emission is only partial and in such cases it is possible either to separate the events completely or at least tag double hits as such. An important advantage of doing this is that counting the number of double events in an image and comparing that number to the number of single hits is an effective way of ensuring that the count rate is not too high that image quality is degraded by intra-pulse pile-up effects.

A raw 8-bit, 500×500 pixel image is first convoluted with a Laplacian of Gaussian (LoG) filter [60] which is a convolution of a Laplacian filter and Gaussian filter. The latter filter smooths the image before edges in the image are sharpened by the former. The output of the LoG filter is then eroded [61] to remove any isthmuses between partially overlapping events. Erosion also removes any noise pixels that are too small to be real events. After erosion, the image is thresholded, and any connected regions are indexed. Each indexed region is identified as a real event, and its centroid, area and ellipticity are then determined. The area and the ellipticity are examined to determine if the event might actually be a double event. If either the area or the ellipticity is larger than preset values, the event is tagged as a double and counted twice for the purposes of reconstructing the momentum distribution from the raw images. The centroid of each event is recorded in a file, with x and y position values stored as floats. The total data that is written to a file is only a few kilobytes per frame, depending on the count rate.

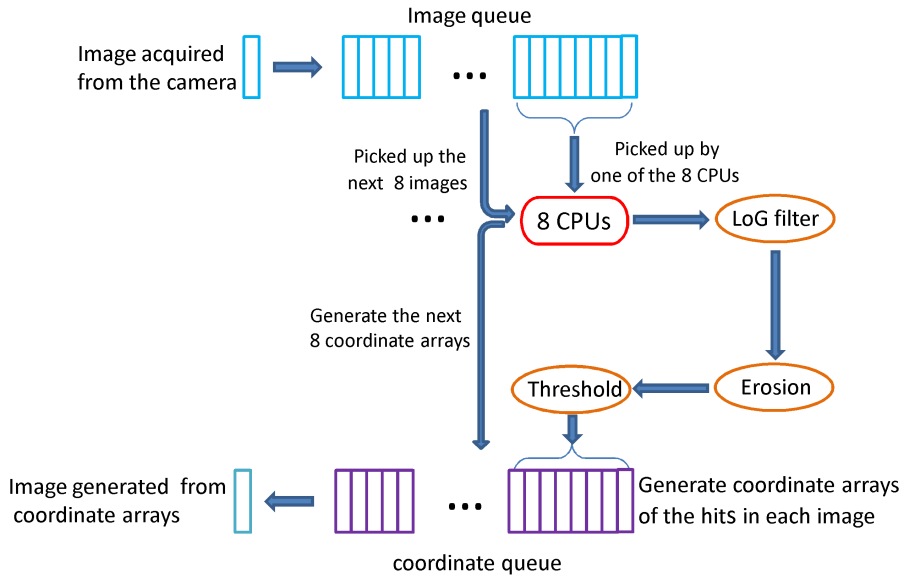

Figure 2.2: *Schematic diagram showing the producer-consumer model implemented for parallel processing of raw image data.*

In order to achieve 1 kfps operation, clones of the image processing algorithms are running simultaneously on all eight available cores of a Dell T7400 workstation. This is achieved using a producer-consumer model and queues [62]. This implementation is shown schematically in Fig.

After each consumer loop has determined the centroids of every event it detects on an image, it writes an array containing the x and y positions of each event to another queue (named coordinate queue in the figure). The event's queue contains variable length arrays of pairs of coordinate values, and is written to by all eight consumer loops. This queue is monitored by another loop that creates the accumulated image, monitors the count rate of single and double events, and writes data to disc. The producer consumer model is used again, but this time there are eight producer loops and one consumer. Since the single consumer loop is computationally trivial, it is able to handle the event's queue at the requisite 1 kfps.

Fig. 2.3 shows a single frame, before and after analysis. The image after analysis is plotted from the position array by assigning an intensity value of 1 for each single event

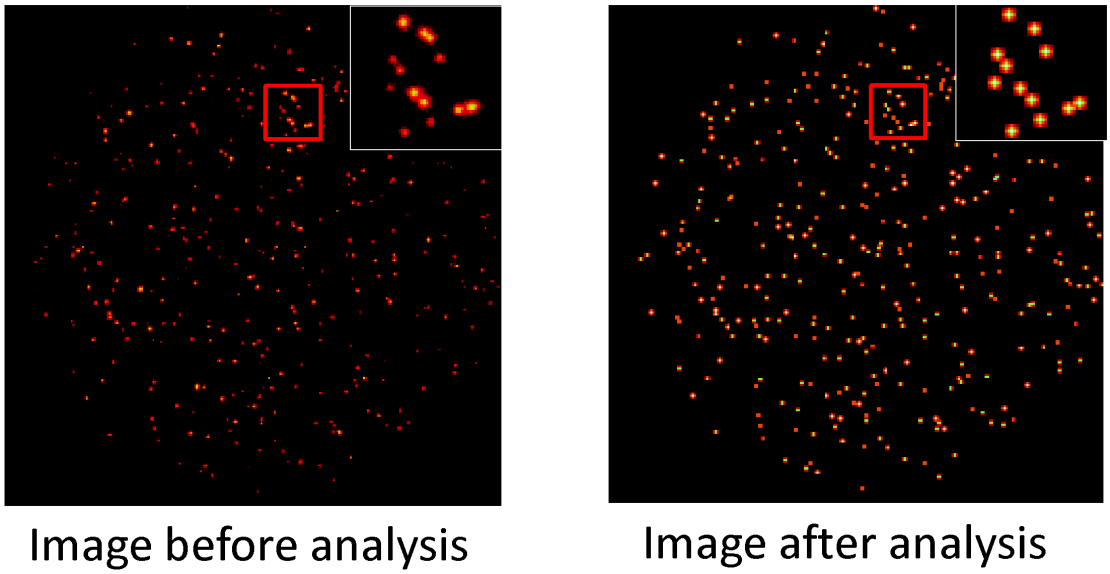

Figure 2.3: *A single frame from the camera, before and after analysis. Ellipticity threshold:1.9, area threshold:10 (any events with ellipticity or area larger than the threshold are treated as double events). The analyzed image has been Gauss-smoothed for display purposes. The top right on both images show a zoom in of the region marked by the red square box.*

and 2 for double events. Overall, the kHz data acquisition system for VMI experiments has several advantages given the widespread use of kHz lasers. We expect such systems to be utilized combining with single shot carrier-envelope phase (CEP) tagging technique [63] for studying CEP-dependent molecular dynamics [64]. Such a system could also be used for single shot high harmonic experiments, once again obviating the need for precise CEP control. High dynamics range measurements, such as the electron momentum distribution after laser induced rescattering and diffraction, should also benefit from such a system. As a demonstration, we use this system to measure FF1DA.

2.3 Measuring FF1DA

The experimental setup is shown in Fig. 2.4, the laser system we use is the Kansas Light Source (KLS), a home-built, multi-pass, chirped-pulse amplified (CPA) Ti-Sapphire laser system. It delivers laser pulses at 2 kHz, 2 mJ/pulse, 30 fs centered at about 790 nm. The

laser beam is then split into pump and probe arms using a broadband 50/50 beam splitter (BS), the probe beam goes through a 30 cm automatic stage which can delay it up to 2 ns. The two beams are then recombined collinearly on another broadband 50/50 beam splitter and focused together using a 35 cm lens into the target chamber (lower chamber in the figure) where a VMI sits. A half-wave plate and polarizer set is placed in the probe arm to vary the intensity. Time overlap of pump and probe pulses is found by focusing both into a barium borate (BBO) crystal to generate second harmonic (SH). Since this was a collinear setup, the blue light could not be separated from the fundamental and both were focused onto a photodiode. When the two pulses are overlapped the SH from their coherent sum causes a jump in the photodiode signal. The target gas molecules supersonically expand through the Even-Lavie gas jet, which cools the rotational temperature of the molecules. When traveling from the source chamber (upper chamber in the figure) to the interaction region in VMI, the molecular rotational temperature further cools down to about 1 K for heavy molecules like iodobenzene and light molecules like N_2 can also get below 10 K.

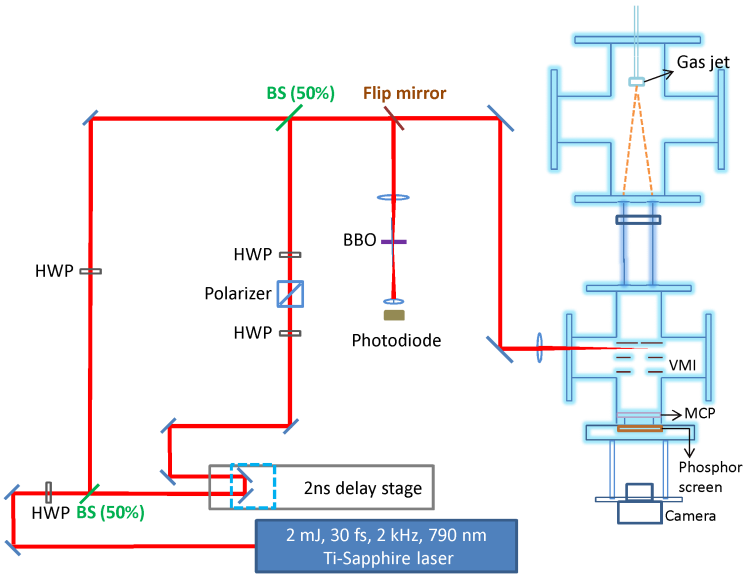

Figure 2.4: *Experimental setup for inducing and measuring FF1DA from rotationally cooled iodobenzene molecules. See text for details.*

A measured alignment trace for a whole C-type rotational period of iodobenzene molecules

is plotted in Fig. 2.5. The pump beam aligns the molecule and the probe beam is delayed with respect to the pump to Coulomb explode the molecules. A VMI image with thousands of laser shots is acquired for I^+ fragment, from which $\langle \cos^2 \theta_{2D} \rangle$ is calculated from the position of each ion hit. By selecting one dissociative channel (depending on its sensitivity to the alignment) and averaging over all the $\cos^2 \theta_{2D}$ values within that channel we can get $\langle \cos^2 \theta_{2D} \rangle$. Ideally, the baseline before time zero should be 0.5 with an ionizing pulse polarization pointing into the detector plane, here it is slightly higher because the pump beam, with its polarization parallel to the detector plane, produces some ionization. Both full and half J-type and C-type revivals are clearly seen in the figure, but no A-type or K-type are seen because the measured $\langle \cos^2 \theta \rangle$ does not involve the angle χ. The appearance of J- and C-type revivals but not A- and K-types revivals is consistent with the calculation, shown in Fig. 1.4 of Chap. 1.

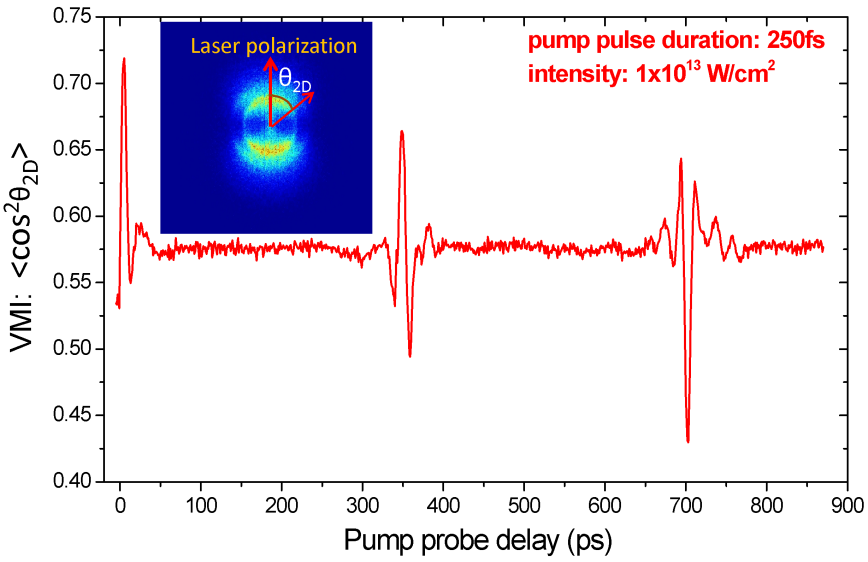

Figure 2.5: *A VMI measurement of the alignment trace of iodobenzene molecules, laser conditions are marked in the figure. The inset shows the VMI image at the initial alignment peak, about 4 ps.*

Even though iodobenzene is an asymmetric top molecule and the theoretical calculations are relatively complex, the experiment is less challenging since the molecules are rotaionally

cooled and highly polarizable, making them very responsive to the laser pulse provided that it is non-ionizing. The degree of alignment attained is $\langle \cos^2 \theta_{2D} \rangle = 0.72$, which is already relatively high. In contrast, for light simple molecules such as N_2, it is experimentally challenging since the molecule has a ''high" rotational temperature ($\sim$ 10 K) and weak polarizability. To strongly align N_2, we take advantage of the multi-pulse technique as discussed in Sec. 1.3. The experimental setup is modified and shown in Fig. 2.6.

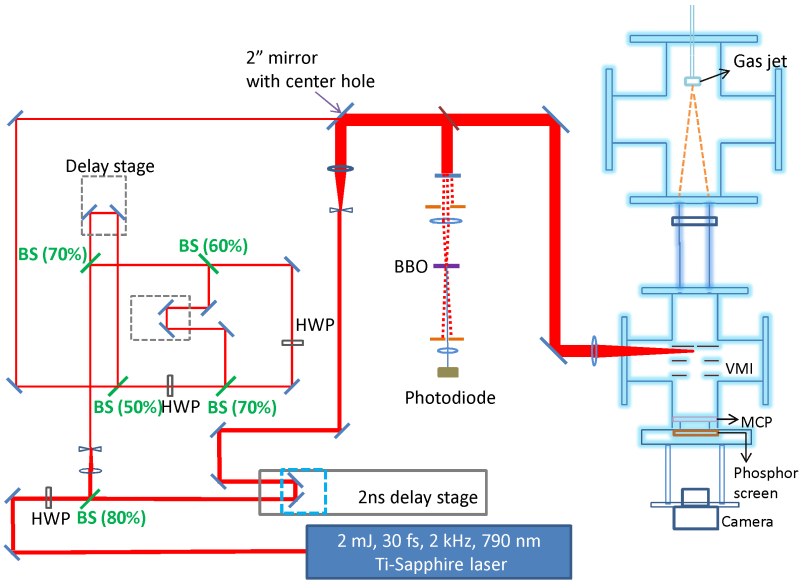

Figure 2.6: *Experimental setup for inducing and measuring FF1DA from rotational cooled nitrogen molecules using three aligning laser pulses. See text for details.*

In order to get multiple laser pulses and still maintain a reasonable amount of energy in each pulse, we make several changes to our setup. First, most of the laser power (80%) goes to the pump beams that are split into three. To make up for the power loss in the probe, we expand the probe beam using a telescope to double the original size, therefore, the intensity at the focus will increase by a factor of four. On the other hand, the pump beam is shrunk by a factor of two to be able to pass through the hole in the center of a 2 inch recombining mirror from which the probe is reflected off. This also expands the size of the pump focal spot, ensuring that the probe only samples strongly aligned molecules. Several additional BS with different splitting ratios are in the pump arm to generate the

three pump beams, two of which have manual delay stages to control the relative delays of all the pump pulses. Since now, all the beams are non-collinear, we can find the time overlap by looking at the SH signal in the center of two fundamentals after they are focused into the BBO crystal. VMI images are then acquired for N^+ fragment and the alignment trace from all three kicks is plotted in Fig. 2.7 along with a TDSE calculation. Note that, the theory can not be directly compared to the measurement, since the theory calculates $\langle \cos^2 \theta \rangle$ while experiment measures $\langle \cos^2 \theta_{2D} \rangle$ from the 2D images. In principle, $\langle \cos^2 \theta_{2D} \rangle$ can be calculated given the angular distribution of the molecule's rotational wave packet and angle dependent dissociative probabilities for N^+ fragment. This calculation will be discussed in later chapters, though the qualitative features of the measurement and the calculated $\langle \cos^2 \theta \rangle$ trace are similar.

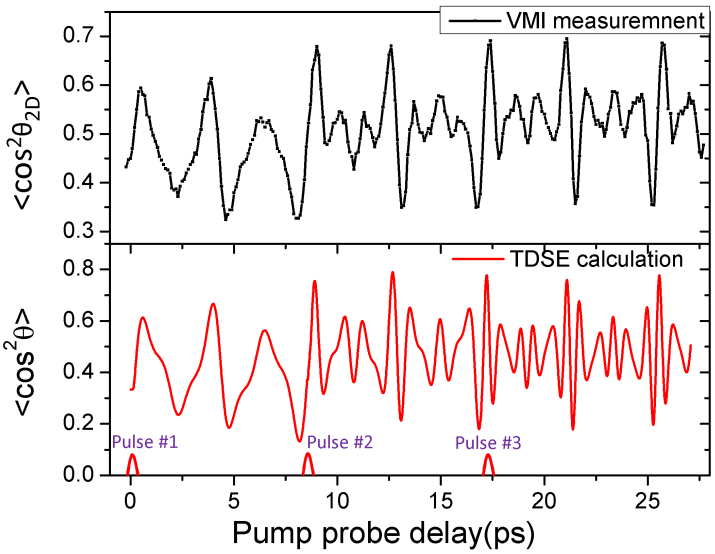

Figure 2.7: *Black curve: Measured momentum distribution of N^+ fragment from N_2 molecules using three time delayed pump pulses. Red curve: A simulation of the multi-pulse alignment for $\langle \cos^2 \theta \rangle$, laser conditions are estimated to be: pulse 1, 80 fs, 20 TW/cm^2, t=0 ps; pulse 2, 80 fs, 30 TW/cm^2, t=8.55 ps; pulse 3, 80 fs, 20 TW/cm^2, t=16.9 ps. Molecular rotational temperature is estimated to be 5 K to give the best agreement between measurment and calculation.*

It took substantial effort to realize that such a complicated multi-pulse setup is actually capable of generating remarkable FF3DA with a slight modification, the next chapter will

particularly focus on getting FF3DA using multiple laser pulses.

Chapter 3

Field-free three-dimensional alignment

3.1 Introduction to FF3DA

The goal of bringing the MF close to the LF is not fulfilled after achieving good 1D alignment (1DA) for asymmetric top molecules. Further confinement is needed in more dimensions. The first experimental and theoretical report on aligning asymmetric tops in three dimensions (3DA) was published very shortly after the first experiment on 1DA of linear molecules [17]. 3DA was achieved by impinging an elliptically polarized nanosecond YAG laser on 3,4-dibromothiophene (see Fig. 3.1) molecules. $\langle \cos^2 \theta_{2D} \rangle \approx 0.78$ was measured for the S^+ momentum distribution using VMI. At the same time the distribution from the Br^+ ion gets narrow, suggesting that there is a weak confinement of the molecular plane as well. In later experiments, the degree of 3DA was further increased by using a linearly polarized nanosecond YAG laser combined with a femtosecond IR field which kicks the molecule in the perpendicular direction at the peak of 1DA [18]. The experiment was performed on 3,5-difluoroiodobenzene (DFIB) molecules (Fig. 3.1). The 3DA is characterized by two angles together: one is the 2D angle between the C-I axis and the polarization axis of the adiabatic pulse and the other is the angle between the benzene plane and the polarization axis of the IR pulse. For these angles, cosine-squared values of 0.87 and 0.74, respectively, were achieved. Even though good 3DA can be achieved using this technique, the align-

ment occurs in the presence of the adiabatic laser field. As stated in Chap. 1 3DA under field-free conditions is desirable. However, there is currently very limited work on FF3DA. The first experimental demonstration used two time delayed, orthogonally polarized fs laser pulses to induce FF3DA of SO_2 molecules [19]. The first pulse aligned the most polarizable axis of the molecule, termed the O axis in the paper (Fig. 3.1). The second pulse arrived slightly before the alignment peak for the O axis and aligned the second most polarizable axis (termed the S axis) in the perpendicular direction. A serious limitation to this method is that second pulse drives the O axis away from alignment. However, since the S axis rotates faster than the O axis, when its alignment peaks the O axis alignment has still not completely faded away, resulting in relatively weak FF3DA (compared to the above mentioned adiabatic technique). The degree of FF3DA achieved in this case was measured using coincidence detection, which under the axial-recoil approximation yields 3D measurements of the angles. The cosine-squared values for angles between the laser polarizations and the S and O axes were each measured to be 0.6. Another technique uses a single elliptically polarized short pulse to align the ethylene molecule and claims to observe FF3DA at a revival time [20] by analyzing calculated alignment traces for several different direction cosines, such as $\langle\cos^2\theta_{xX}\rangle$, $\langle\cos^2\theta_{yY}\rangle$, $\langle\cos^2\theta_{zZ}\rangle$ and some off-diagonal directional cosines (see Chap. 1 for definitions of the direction cosines). An experiment is carried out using an optical Kerr-effect technique detailed in the next chapter of this thesis. The expectation values of two direction cosines are estimated to be 0.37 from the results of this experiments, implying very weak FF3DA since the isotropic values are 1/3.

In both examples, in order to quantify 3DA, careful examinations of the temporal evolution for several direction cosines are required. This makes the characterization of 3DA complicated in both experiments and computations. We know that for 1DA, a single measure: $\langle\cos^2\theta\rangle$ can be used to quantify the degree of alignment, is there a similar measure for 3DA as well? Besides that, and more importantly, only relatively weak FF3DA has been achieved so far, and a theoretical study proved that SO_2 cannot be 3D aligned using

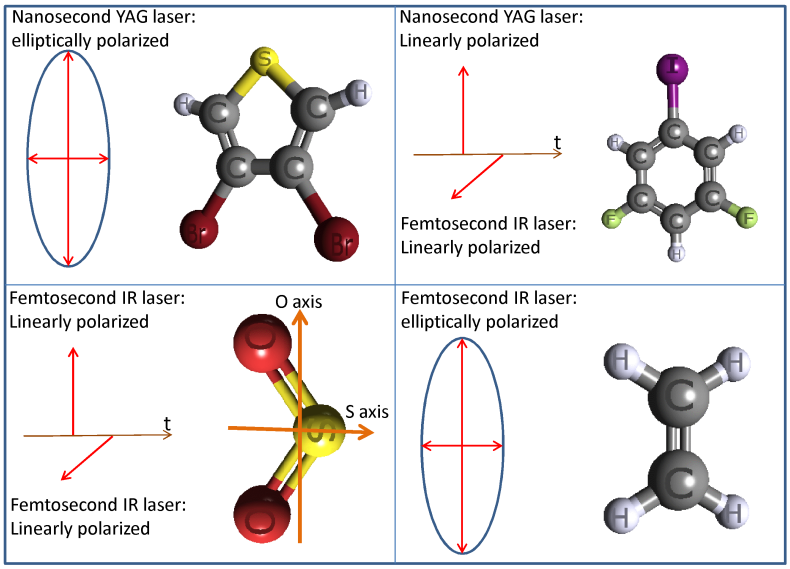

Figure 3.1: *Structure of 3,4-dibromothiophene and 3,5-difluoroiodobenzene, sulfur dioxide and ethylene molecules.*

multiple identical elliptically polarized pulses [65]. Is there another pulse sequence that can fulfill this task? Both questions will be addressed in this chapter.

3.2 A metric for 3DA and a multi-pulse scheme to enhance FF3DA

Part of this section is adapted from Makhija *et al.* [66].

In order to find such a single measure for 3DA, we use the axis-angle representation rather than Euler angles or direction cosines, because in the axis-angle representation, the distance between any two orientations can be represented by a single rotation δ_{if}, which is the rotation that takes an initial orientation $(\theta_i, \phi_i, \chi_i)$ to the final orientation $(\theta_f, \phi_f, \chi_f)$ [66, 67]. By writing the rotation in terms of the rotation matrices $\mathbf{R}(\theta, \phi, \chi)$ [68], we have

$$\cos\delta_{if} = \frac{1}{2}\{tr[\mathbf{R}^T(\theta_i, \phi_i, \chi_i)\mathbf{R}(\theta_f, \phi_f, \chi_f)] - 1\}. \tag{3.1}$$

With the goal of rotating any arbitrary MF to the LF, the final orientation is the LF—thus $\mathbf{R}(\theta_f, \phi_f, \chi_f)$ is the identity matrix. $\cos\delta$ can then be written in terms of other representa-

tions:

$$\cos\delta = (\cos\theta + 1)[\cos(\phi + \chi) + 1]/2 - 1 = [\cos\theta_{xX} + \cos\theta_{yY} + \cos\theta_{zZ} - 1]/2 \qquad (3.2)$$

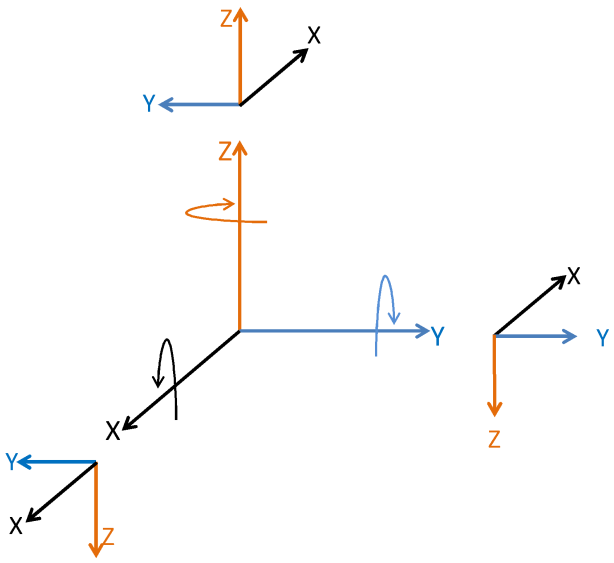

Figure 3.2: *The four equivalent target orientations for 3DA reached by rotating about the LF axes by 180 degrees.*

Since a 3D aligned distribution has D_2 symmetry, there are four equivalent target orientations connected by a rotation of the LF about any of its Cartesian axes by 180 degrees, see Fig. 3.2. Defining these rotations as δ_F ($F = O, X, Y, Z$), where O represents the LF and X, Y, Z correspond to target orientations obtained from rotation about the LF X, Y, Z axes. These can be expressed in terms of the Euler angles as follows

$$\cos\delta_O = (1 + \cos\theta)[1 + \cos(\phi + \chi)]/2 - 1, \qquad (3.3)$$

$$\cos\delta_X = (1 - \cos\theta)[1 - \cos(\phi - \chi)]/2 - 1, \qquad (3.4)$$

$$\cos\delta_Y = (1 - \cos\theta)[1 + \cos(\phi - \chi)]/2 - 1, \qquad (3.5)$$

$$\cos\delta_Z = (1+\cos\theta)[1-\cos(\phi+\chi)]/2 - 1, \tag{3.6}$$

taking into account that 3DA does not distinguish between positive and negative directions for all the MF and LF axes. The square of the above cosines for each target orientation can be averaged resulting in an expression for the distance from a 3D aligned distribution –

$$\cos^2\delta = \frac{1}{4}(1+\cos^2\theta_{xX}+\cos^2\theta_{yY}+\cos^2\theta_{zZ}). \tag{3.7}$$

For perfect 3DA, the (x, y, z) axes get confined to the corresponding (X, Y, Z) axes and $\langle\cos^2\delta\rangle = 1$. The expectation value for a uniform distribution equals $1/2$, and its minimum value is $1/4$ when all three axes are perfectly anti-aligned. For perfect 1DA, the expectation value will be $3/4$.

In order to test the validity of this measure, a calculation on FF3DA of iodobenzene molecules is performed using the same pulse configuration as in Ref. [19]. Two orthogonally polarized laser pulses were used to induce FF3DA. The first Z-polarized pulse aligns the most polarizable C-I axis (or z axis), the second X-polarized pulse comes around the peak alignment of the z axis and kicks the benzene plane inducing confinement of the other two axes. Fig. 3.3 shows the time evolution of the three direction cosines along with the trace for $\langle\cos^2\delta\rangle$.

It is clear from the figure that, with just one pulse, right after the kick, the z axis gets pushed closer to the Z axis while angles θ_{yY} and θ_{xX} are also affected but do not contribute to the structure of $\langle\cos^2\delta\rangle$. After the second pulse, which is polarized along the perpendicular axis, the z axis is driven away from the Z axis very quickly. However, the x and y axes are confined to the corresponding LF axes even faster, and reach peak alignment before the z axis completely misaligns, resulting in FF3DA. This can be directly seen in the $\langle\cos^2\delta\rangle$ plot, where the spike following the second pulse indicates FF3DA. Therefore, instead of searching for the FF3DA peak from many different direction cosine traces, we only need to look at the $\langle\cos^2\delta\rangle$ trace to find out that the FF3DA peaks at 4.73 ps.

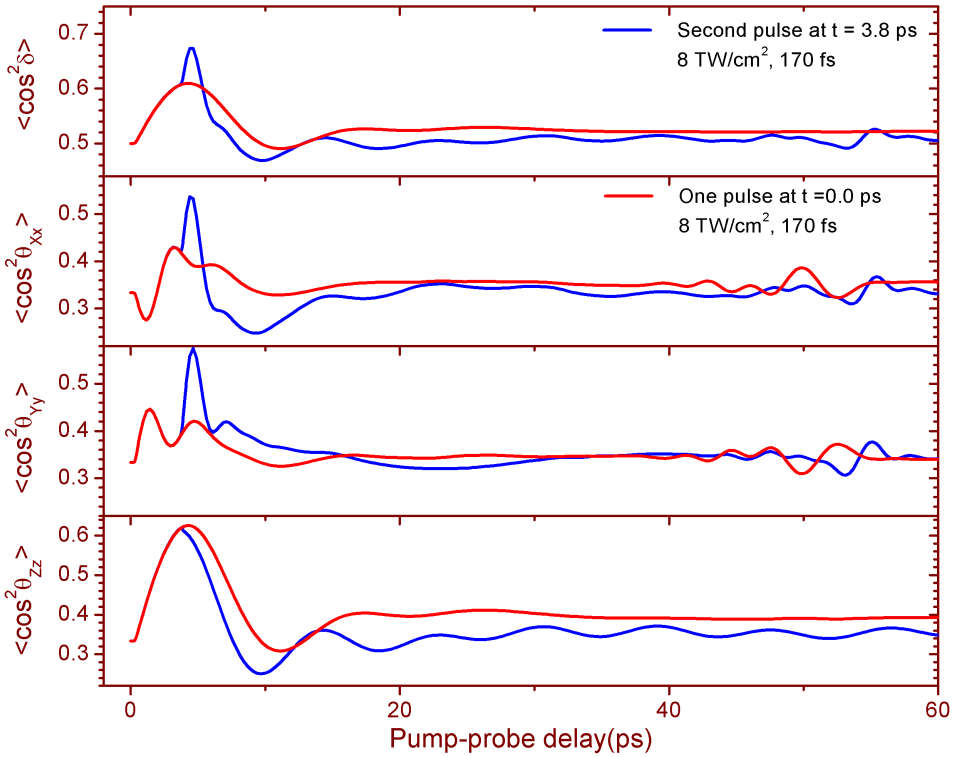

Figure 3.3: *TDSE calculations of the FF3DA from iodobenzene molecules using two orthogonally polarized pulses. Blue line shows the time evolution after one laser pulse, red line shows the time evolution after both pulses. Laser parameters are as shown in the figure, the rotational temperature of iodobenzene is 0.5 K. Calculated by Varun Makhija.*

By knowing the exact time when 3DA peaks and its strength from calculating $\langle\cos^2\delta\rangle$, this measure can be explored computationally to find possible ways of enhancing 3DA. In the previously mentioned experiment by Lee *et al.* [19], the two orthogonally polarized pulses give $\langle\cos^2\delta\rangle$=0.63 while a single elliptically polarized pulse used by Rouzée *et al.* [20] gives $\langle\cos^2\delta\rangle$=0.52. Both are not very strong compared to an isotropic value of 0.5. More importantly, neither shows scope for improvement. Specifically, using two orthogonally polarized pulses will always degrade the alignment of the first axis. Even though tuning the separation of the pulses makes it possible to find the optimum FF3DA peak, it still compromises the alignment of the most polarizable axis in order to achieve FF3DA. In Ref. [19], the first pulse already gives $\langle\cos^2\delta\rangle$=0.62 while the final 0.63 value is a result of loss of alignment in the first axis and gain in alignment of the other two axes. For a single

elliptically polarized laser pulse with defined intensity and pulse duration, ellipticity is the only knob. Linear polarization will give FF1DA, circular polarization will cause planar alignment [17], and Rouzée *et al.* [20] show that a specific ellipticity in between results in the best FF3DA for a given molecule.

In order to develop a technique that is more efficient and robust, it is intuitive to think of using multiple laser pulses since it was shown to be effective for linear molecules. Such a method has already been theoretically simulated for an asymmetric top molecule—SO_2 [65], showing that multiple pulses could not be used to increase or even induce FF3DA. However, this rather general conclusion was drawn after only attempting to align SO_2 with a single predefined pulse sequence. Our calculations show that a multi-pulse scheme indeed works for increasing FF3DA, provided that an appropriate pulse sequence is applied. We were able to determine that for a molecule with both prolate-type inertia and polarizability tensors such as SO_2, a sequence of elliptically polarized pulses following a linearly polarized pulse will result in a strongly 3D aligned distribution. Using DFIB as an example, the linear first pulse aligns the C-I axis and the subsequent elliptical pulses align all three axes simultaneously. Each successive kick is timed to arrive at the peak FF3DA induced by the preceding pulses as quantified by $\langle \cos^2 \delta \rangle$. The ellipticities are determined by comparing the matrix elements of $\langle \cos^2 \delta \rangle$ with the interaction Hamiltonian [30]. We can write both analytically in the symmetric top basis $|JKM\rangle$

$$
\begin{aligned}
&\langle JKM|H_I(t)|J'K'M'\rangle \;=\; \\
&\quad 4\pi\alpha I(t)\Big[\frac{(2-3\epsilon_X^2)}{\sqrt{6}}\,\langle JM;2,0|J'M'\rangle + \frac{\epsilon_X^2}{2}(\langle JM;2,2|J'M'\rangle + \langle JM;2,-2|J'M'\rangle)\Big] \\
&\quad \times [\alpha_0^2\,\langle JK;2,0|J'K'\rangle + \alpha_2^2(\langle JK;2,2|J'K'\rangle + \langle JK;2,-2|J'K'\rangle)], \qquad (3.8)
\end{aligned}
$$

$$
\begin{aligned}
&\big\langle JKM|\cos^2\delta|J'K'M'\big\rangle \;=\; \\
&\quad \frac{1}{4} + \frac{1}{4}\delta_{JJ'}\delta_{KK'}\delta_{MM'} + \frac{1}{4}\sqrt{\frac{2J+1}{2J'+1}}\,\langle J,M;2,0|J',M'\rangle\,\langle J,K;2,0|J',K'\rangle \\
&\quad + \frac{1}{8}\sqrt{\frac{2J+1}{2J'+1}}\Big\{\big[\,\langle J,K;2,2|J',K'\rangle + \langle J,K;2,-2|J',K'\rangle\,\big] \\
&\quad \times \big[\,\langle J,M;2,2|J',M'\rangle + \langle J,M;2,-2|J',M'\rangle\,\big]\Big\}, \qquad (3.9)
\end{aligned}
$$

where $H_I(t)$ is the interaction Hamiltonian and ϵ_X is the weight of the electric field amplitude in the X direction. The electric field can be expressed as $\mathbf{E}(t) = E_0(t)[\epsilon_X\cos(\omega t)\mathbf{e}_X + \sqrt{1-\epsilon_X^2}\sin(\omega t)\mathbf{e}_Z]$, α is the fine structure constant, α_m^l are spherical components of the molecular susceptibility tensor and $\langle J,M;J',M'|J'',M''\rangle$ are the Clebsch-Gordan coefficients. We label those terms with $\Delta K, M = 0$ as 00 terms, those with $\Delta K = 0, \Delta M = \pm 2$ as 02 terms and so on. As shown in both equations, there are only 00 and 22 terms in the matrix element of $\cos^2\delta$ while matrix elemeent of H_I has 00, 22, 20 and 02 terms. In order to boost FF3DA, or equivalently, enhance $\langle\cos^2\delta\rangle$, our goal is to increase both 00 and 22 tinteractions. The 00 term is equivalent to $\cos^2\theta$ interaction (for linearly polarized laser pulse), thus contributes to 1DA of the C-I axis (z axis) while the 22 term contributes to the alignment of the other two axes (x and y axes). In the interaction matrix elements, there are two extra terms—02 and 20, both will contribute to the value of $\langle\cos^2\delta\rangle$, however, the mechanism of thier contribution merits further theoretical investigation. Guided by TDSE calculations over a range of parameters, we choose pulse sequences that enhance the 00 and 22 terms in the interaction while reducing the effect of the 02 and 20 terms. Since the parameters space is not searched systematically, our results only set a baseline — better

pulse sequences for maximizing 3DA are very likely to exist.

Note that the 00 term contributes up to 1/4 of the total $\langle \cos^2 \delta \rangle$ (in addition to the isotropic value of 1/2). So in order to enhance FF3DA, it is important not to compromise the FF1DA. Therefore, the coefficient of the 00 term in the interaction matrix element needs to satisfy: $2 - 3\epsilon_X^2 \geq 0$, which yields $\epsilon_X^2 \leq \frac{2}{3}$. That is the condition on the ellipticity for each of the following elliptical pulses, which can align all three axes through the 00 and 22 terms. Fig. 3.4 shows a simulation of such a multi-pulse scheme on DFIB molecules using up to four pulses, the first linearly polarized along the LF Z axis, and the rest elliptically polarized in LF XZ plane with the major axis in the Z direction. Each pulse after the first one arrives a few hundred fs before the peak of the $\langle \cos^2 \delta \rangle$ due to all the previous pulses. Specifically, the first pulse (at t=0 ps) gives a peak $\langle \cos^2 \delta \rangle$ value of 0.61 at around 3.4 ps, the second pulse arrives at 2 ps to increase the value of $\langle \cos^2 \delta \rangle$. Before it reaches the peak value at around 3.53 ps, the third pulse arrives at 3.3 ps to enhance the FF3DA. Ideally, we can add as many pulses as we want as long as there is enough time to fit in pulses before the FF3DA peaks.

It is clear from the calculation that, after each kick, all three axes are better confined and FF3DA increases continuously. In particular, there is an increment rather than decrement in the z axis alignment, which leads to a much better FF3DA compared to the case in Fig. 3.3. A $\langle \cos^2 \delta \rangle$ value of 0.71 is achieved after the first three pulses, which is a significant improvement over previous attempts. However, we can not directly measure $\langle \cos^2 \delta \rangle$ in experiment yet. The proposed pulse sequence is demonstrated experimentally by aligning DFIB molecules, and the degree of FF3DA is estimated by the confinement of the molecular C-I axis to the laser Z axis and the benzene plane to the laser X axis, which are measured using VMI.

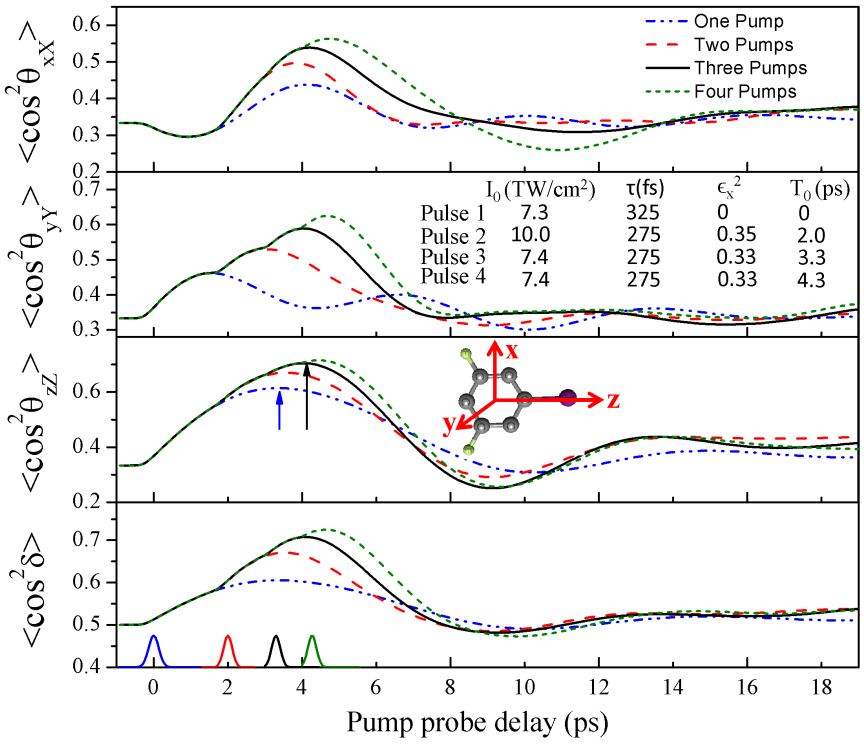

Figure 3.4: *TDSE calculations of the FF3DA from DFIB using up to four laser pulses. Top three panels show the time evolution of the three direction cosines, bottom one shows how* $\langle \cos^2 \delta \rangle$ *evolves after each kick. Pulse intensities and durations are limited by the experimental constraints. Calculated by Varun Makhija.*

3.3 Experiment of multi-pulse FF3DA

The experiment is performed using the same setup as in Fig. 2.6 with a quarter-wave plate placed in the beam path after the recombination of pump 2 and 3 to make both circularly polarized. Then pump 2 and 3 recombine with pump 1 on a BS that has different transmission efficiency for, and adds different phase to the s and p polarization components, making the circularly polarized light elliptically polarized but with major axes tilted away from Z axis. A quartz plate is placed in the path after the recombination of all three pumps to rotate the major axes back to the LF Z axis. Polarizations of all pump and probe pulses are carefully characterized by measuring Stokes parameters. The target DFIB molecules are seeded in high pressure helium gas through the supersonic gas jet and rotationally cooled

to about 1 K. We use VMI to measure the momentum distribution of both I^+ and F^+ fragments. The former indicates the alignment of the C-I axis and the latter the confinement of the benzene plane.

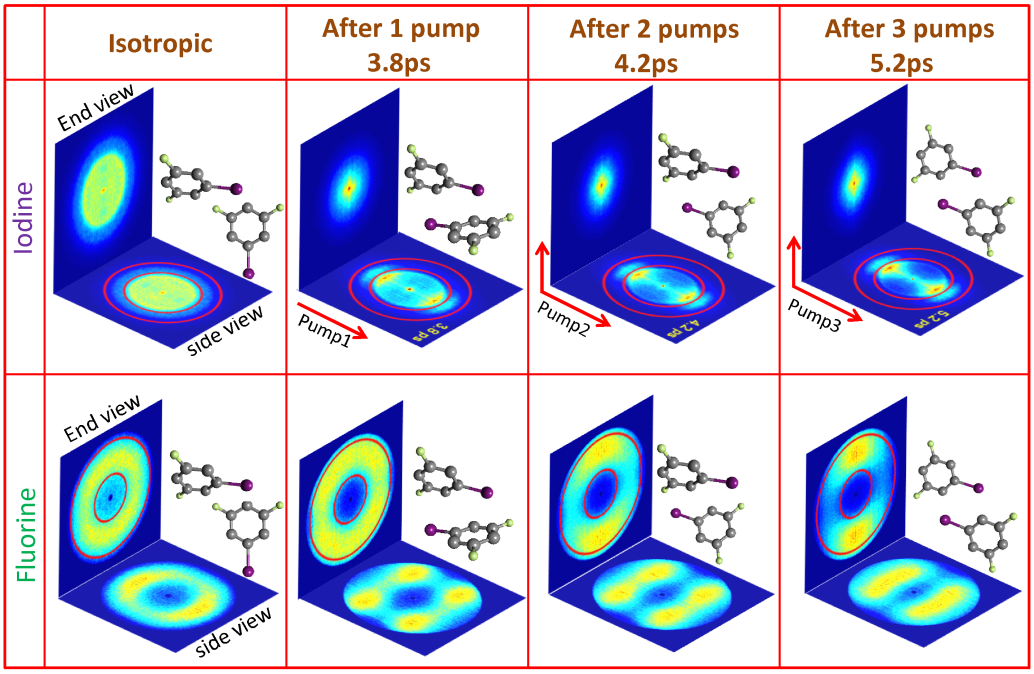

Figure 3.5: *End and side views of both iodine and fluorine ion fragments at different moments, all images have been Gaussian smoothed and four fold symmetrized (Since the polarization of the elliptically polarized pulses have four fold symmetry in the polarization plane, the resulting momentum distributions have four fold symmetry.). "Isotropic" gives the momentum distribution for both ions before any aligning pumps interact with the molecules. "After 1 pump" shows the distributions at the peak of the FF1DA of C-I axis, which is about 3.8 ps. "After 2 pumps" and "After 3 pumps" show the distributions at the peak of the FF3DA after two kicks and three kicks, respectively.*

Images for both ions at different times are shown in Fig. 3.5. For both I^+ and F^+, images collected with the C-I axis aligned perpendicular to the detector are referred to as "end view" images, and those with the C-I axis parallel to the detector are referred to as "side view" images. The polarization of the probe pulse is chosen to be perpendicular to the detector plane for both I^+ end and side views. For F^+, the probe is perpendicular to the detector for end views and parallel to the detector for side views. By doing so, the effect of the probe on the measured angular distributions is minimized. Before any aligning pulses,

both end and side views of I^+ give uniform distributions, while for F^+, because the probe preferentially dissociates molecules that have the C-I axis along the probe polarization axis, the resulting F^+ distribution has a donut shape for both side and end views. The first linearly polarized pulse aligns the C-I axis but leaves the benzene ring spinning. At the alignment peak, the I^+ side view clearly shows more counts along pump 1's polarization axis, and because of the alignment of the C-I axis and the distribution of the I^+ in the end view becomes tighter. For F^+, because the C-I axis is fixed, more F^+ will be driven away from the center, so in the end view, the number of counts in the center of the donut decrease significantly. Since the benzene ring is still spinning, the projection of the spinning F^+ rings produces four spots in the side view images. Pump 2 aligns both the C-I axis and the benzene ring at the same time. The side view distribution of I^+ gets stretched and further confined to the major axis and the end view distribution becomes even tighter. The minor axis of pump 2 starts to align the benzene ring, in the end view of F^+ the distribution starts going towards the direction of the minor axis and since the rotation of the benzene ring is more confined now, the four spots on the side view start to merge into two spots. After pump 3 arrives, it further increases FF3DA, especially for the F^+ distribution, where both the side and end views of F^+ become more confined. We can define an angle θ_{2D} in the I^+ side views as the angle between vector of an individual hit with respect to the image center and laser major axes. We can define the same angle for the F^+ end views as the angle with respect to the laser minor axes. Then we can plot the evolution of the cosines of both angles after each pump pulse, as shown in Fig. 3.6. A projected 2D value of 0.8 is reached for the C-I axis and 0.65 for the benzene plane at the peak of the FF3DA which, to the best of our knowledge, is the highest degree of FF3DA achieved thus far. It is also comparable to the peak values measured in [18], where the peak alignment occurs in the presence of the aligning laser field. Furthermore, this value can be further enhanced by adding more elliptically polarized pulses as shown theoretically in Fig. 3.4.

Calculations also show that the pulse sequence described here, with the pulses appro-

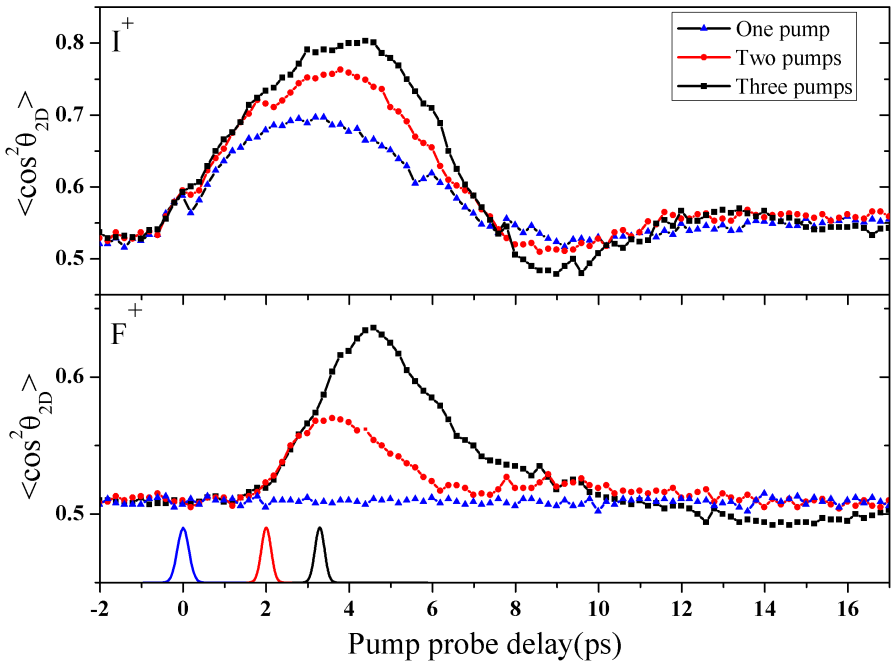

Figure 3.6: *Top panel shows the time evolution of the* $\langle \cos^2 \theta_{2D}$ *measured in* I^+ *side views for one pump, two pumps and all three pumps. Lower panel shows a similar figure measured in* F^+ *end views. Laser parameters are the same as in Fig. 3.4.*

priately timed, is also effective for other asymmetric tops with a prolate-like polarizability, however, the same pulse sequence is not effective for those with oblate-like polarizability. In the latter case, changing the linear first pulse to an elliptical pulse is predicted to induce and enhance FF3DA.

3.4 Tomographic measurement

Even though the 2D momentum distributions and their evolution with time suggest that we have achieved remarkable FF3DA, they do not distinguish clearly between confinement of the molecular C-I axis to XZ plane or the Z axis. It is possibe that the elliptically polarized pulsed will confine the C-I axis to the plane of the polarization rather than to the major axis if incorrect ellipticities (with $\epsilon_X^2 > \frac{2}{3}$) are used. In order to correctly quantify the alignment of the C-I axis we need to reconstruct the 3D I^+ momentum distribution. For that purpose, a tomographic measurement is needed since the distribution does not have

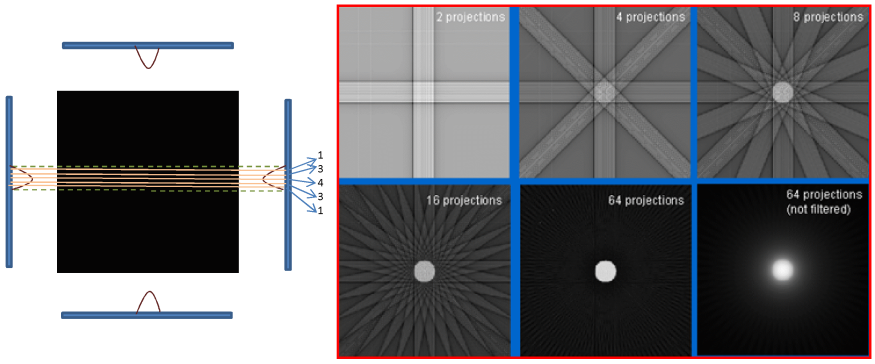

Figure 3.7: *A simple illustration of how the filtered back-projection algorithm works.Right side figures are adapted from www.impactscan.org/slides/eanm2002/img014.gif.*

cylindrical symmetry.

To perform such a measurement, the probe polarization is chosen to be circular to minimize the probe selectivity effect. Then a zero order broadband half-wave plate is placed after the recombination of all the beams and rotated with a step size of 2 degrees between 0 and 90 degrees rotating the beam polarizations together at a pump-probe delay of 5.2 ps, where the maximum FF3DA is achieve. Therefore, we get 90 projections of the 3D distribution onto the detector plane with each projection containing up to 1 million ion counts. A filtered back-projection algorithm [69] is then used for the reconstruction of the 3D momentum distribution.

Fig. 3.7 shows how the algorithm works. Briefly, when the unknown 2D object gets projected onto a line, an intensity array will be accumulated on each line. Projecting different intensity lines back, the intersection of those lines will form the object. The figure on the right tells us that the more projections we have, the more resolution we will have in the reconstructed object. In our case, we have a 3D object that projects onto 2D planes, though the procedure is the same. By running such an algorithm on the data set with the correct ellipticity, we get the reconstructed 3D-momentum distribution for I^+ in Fig. 3.8.

These plots show that the C-I axis remains well aligned with the Z axis rather than getting redistributed to the XZ plane after the elliptical pump pulses. When combined with

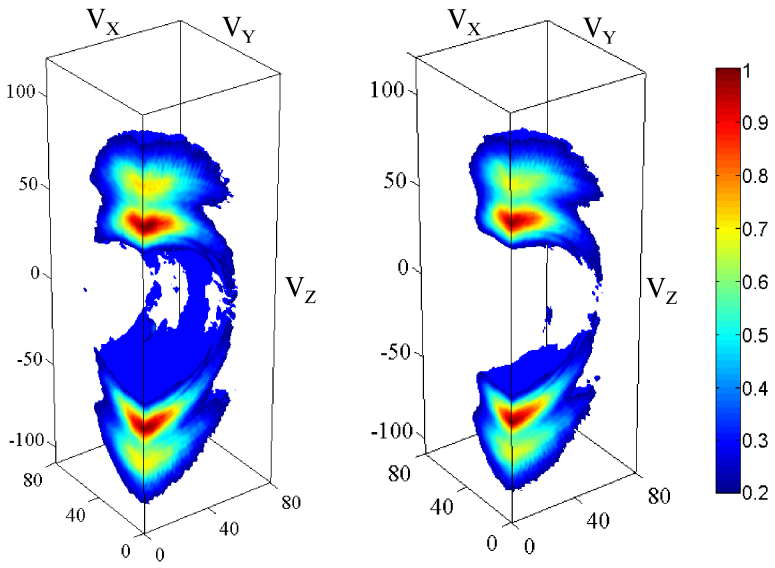

Figure 3.8: *Reconstructed 3D-momentum distribution for I^+ at the peak of FF1DA (left) and FF3DA(right).*

the fluorine projections in Fig. 3.5, these images show FF3DA unambiguously. We can also calculate $\langle\cos^2\theta\rangle$ values from the reconstructed 3D distributions for the peak FF1DA and FF3DA, which are 0.56 and 0.65, respectively. These two values can be directly compared to the values indicated by the arrows in the $\langle\cos^2\theta_{zZ}\rangle$ plot in Fig. 3.4. The calculated values are 0.61 and 0.7, which are higher than the measured ones. One possible reason is that in the calculation the molecular rotational temperature is set to be 0.5 K, while in the experiment, it is more likely to be around 1 K. Further no intensity averaging over the focal volume is performed in the calculation.

In Chap. 2 and 3, I have described in detail the VMI technique for measuring momentum distributions from molecular fragments. Both FF1DA and FF3DA can be measured using this technique. However, there are several limitations, first, the fragments must dissociate along the bond axis direction to reveal the alignment distribution, or in other words, only those molecules obeying the axial-recoil approximation can be used as the targets for measuring alignment. Second, due to the sensitivity of the detection system, the gas density needs to be very low in the interaction region, therefore, the aligned molecules will not be

suitable for any further experiments that require high gas density, such as high harmonic generation. So we would like to find some ways that allow us to measure alignment from much broader species of molecules as well as in an environment with much higher gas density, this will be the topic of the next chapter.

Chapter 4

Optical measurement of molecular alignment

4.1 Introduction to different optical measurements

Generally speaking, one does not need to break the molecule in order to measure its alignment [70, 71]. Moreover, angular dependence of the dissociation channels of molecules, especially for large molecules, can be quite complicated [72]. In the VMI measurement, the momentum distribution of the fragments is convolved with the contribution from the strong probe pulse and thus does not always represent the degree of alignment very precisely. On the other hand, linear and non-linear optical interactions with a molecular gas are easier to characterize and can be used as a measurement of alignment. The idea is that when molecules are not aligned, all optical properties should be the same along all different directions. When molecules are aligned, let's say 1D aligned along the LF Z axis, optical properties, such as refractive index and higher order non-linear optical susceptibilities, will be different along the Z axis compared to the X or Y axis. The stronger the alignment, the greater the difference between the optical properties of the axes will be. Measuring these differences through optical interactions with the gas can serve as a measure of the degree of molecular alignment.

There are two popular ways of doing optical measurements. The first measures the induced birefringence in the gas, named Kerr-effect measurement [71]. The second measures

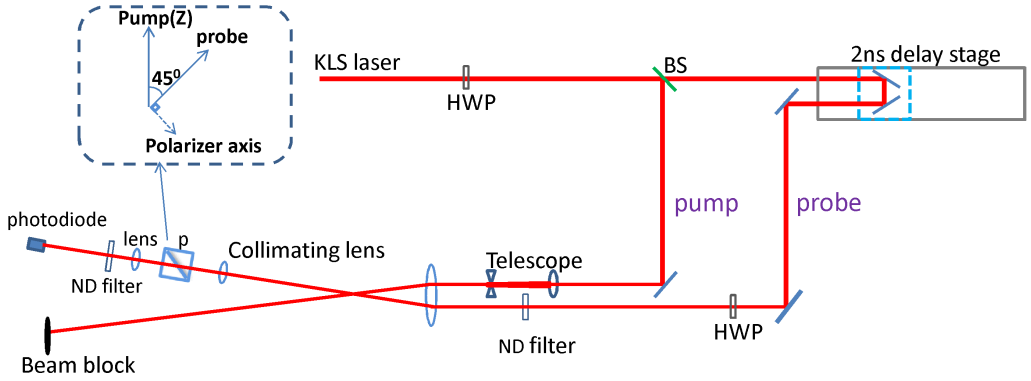

Figure 4.1: *Experimental setup of the Kerr-effect measurement.*

alignment using the transient grating diffraction technique [70, 73]. These two methods will be discussed in detail in this section.

The simple experimental setup for Kerr-effect measurement is shown in Fig. 4.1. The KLS laser beam is split into pump and probe arms, and focused non-collinearly using a 2 inch lens into the target gas—air is used for the experiment. A telescope is placed in the pump beam in order to reduce the pump beam size, thus increasing the size of its focal spot, ensuring that the probe beam only sees molecules that are aligned. A neutral density (ND) filter is placed in the probe beam to greatly reduce the power causing the probe beam to not dissociate or ionize the molecules. After the focus, the probe is collimated and sent through a polarizer after which the light intensity is measured using a photodiode. Polarization of the pump pulse is along the LF Z axis while the probe polarization is 45 degrees with respect to that of the pump. The optical axis of the polarizer is perpendicular to the probe. Initially, when there is no alignment, the probe beam gets filtered by the polarizer and there is no light on the photodiode. After the pump beam aligns the molecules in the air (mostly N_2 and O_2) along the Z axis, the probe beam will experience different refractive indices along Z and its perpendicular axis—X axis. Thus, the X and Z components of the probe pulse will have a phase difference which causes it to become elliptically polarized. Light along the minor axis will transmit through the polarizer and fall on the detector. The better the alignment is, the larger the ellipticity, and correspondingly the stronger the photodiode

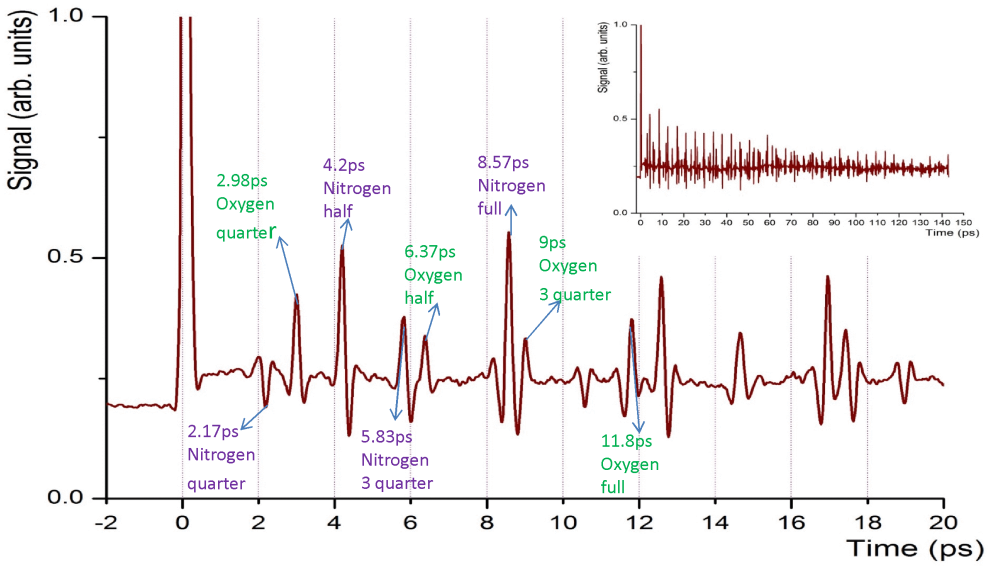

Figure 4.2: *Revival trace in air measured by optical Kerr-effect. All the quarter, three quarter and full revivals can be seen for both N_2 and O_2 molecules at the correct time. A long delay scan up to 140 ps is shown in the inset.*

signal. Fig. 4.2 shows our measured trace from air with all revivals from N_2 and O_2 marked. Note that the alignment dies gradually for a delay up to 140 ps. This is because at high gas density and high temperature, molecular collisions wash out the alignment as time evolves.

The signal is proportional to $(\cos^2\theta - 1/3)^2$ [71], so it gives a positive peaks for both alignment and anti-alignment. Due to this lack of sensitivity to direction, this type of measurement is called a homodyne measurement. In practice the signal may appear heterodyned (sensitive to direction) in the presence of a baseline offset due to light leakage through the polarizer. As shown previously in Eq. 1.10, the phase difference between two rotational states that coupled by the $\cos^2\theta$ interaction equals $2B(2J+3)$. Therefore, a Fourier transform will give frequency components spaced by $4B$, as plotted in Fig. 4.3. Contributions from even and odd J states are marked by the red lines for N_2 and O_2 molecules, respectively.

The Kerr-effect measurement is easy to set up and interpret, however, since it is a linear optical process, a large amount of gas density is required to give enough refractive index anisotropy—the difference between refractive index parallel and perpendicular to the molec-

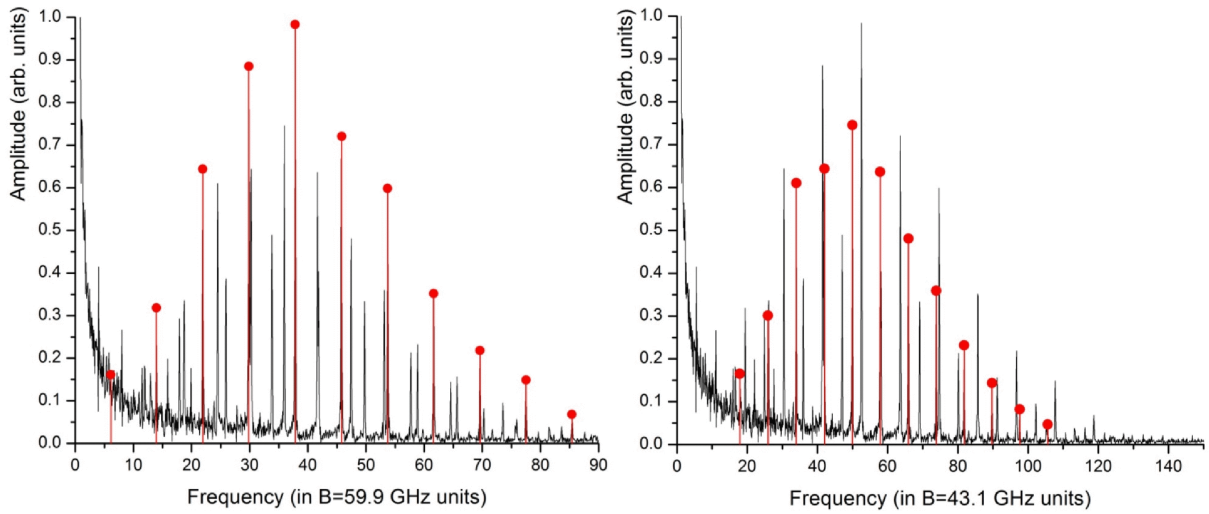

Figure 4.3: *Fourier transform of the revival trace in air. Left panel shows the spectrum as a function of the N_2 rotational frequency, components from even J states are marked as red lines. Right panel shows the same thing for odd J states in O_2.*

ular axis—in order to cause change to the polarization of the probe. For a pulsed gas jet, the number density in front of the jet is still much smaller compared to the air target used, therefore, the depolarization of the probe is too weak to be detected (or distinguished from the background light) by using an avalanche photodiode detector, however such experiment was demonstrated successfully by using a photomultiplier tube [71] for a CO_2 gas jet. Nevertheless, when measuring alignment from non-gaseous molecules, such as iodobenzene (IB) molecules, a small amount of liquid is placed inside the gas jet and carried out by the carrier gas, the resulting gas density is orders of magnitudes smaller than using pure molecular gases. The Kerr-effect technique is clearly not very suitable for such experiments. Therefore, a more sensitive, non-linear optical method has been explored for measuring alignment from low number density molecules, named transient grating diffraction technique.

Fig. 4.4 shows the focusing geometry for this technique. Three laser beams with the same wavelength at three corners of a square (BOX-CARS geometry [74]) focus into the gas target using the same lens. Because of phase matching, a fourth beam of the same color will exit from the forth corner at the output and this is the signal beam that is detected. Two

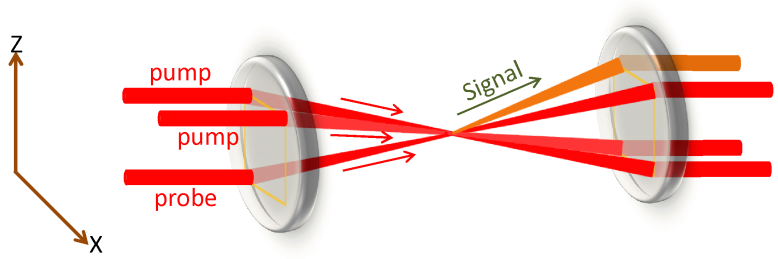

Figure 4.4: *A demonstration of the phase matching in the transient grating diffraction method. See text for details.*

of the incoming beams overlap and interfere with each other and form an alignment grating in the medium, with maximal alignment at positions of constructive interference. The third beam is time-delayed with respect to the other two beams and refracts off this grating to form the signal beam.

To confirm the validity of this technique at low gas density, an alignment experiment is performed on a N_2 gas jet first. Two pump beams (as labeled in Fig. 4.4) are overlapped and used to align the molecules. Polarizations of the pumps are chosen to be orthogonal (one along the Z axis, the other one along the X axis) to form a polarization grating [73], because in the parallel case, in which an intensity grating is formed, ionization and plasma formation will disturb the measured signal [73]. The probe beam is then delayed with respect to the pumps, and the trace of the signal strength is recorded and plotted in Fig. 4.5; note that this is also a background free and homodyne measurement. For a scan up to about 80 ps, there is no clear decay of the alignment due to the lower gas density and rotational temperatures being achieved from the gas jet. However, when such measurement is applied for seeded IB, signal was detectable but no convincing revival trace was measured. This is most likely due to the complexities of the alignment grating setup in an asymmetric top sample, especially for the cross polarized pumps configuration. Taking these facts into consideration, we modified the transient grating diffraction technique and came up with a new scheme based on pump-degenerate four wave mixing (DFWM) [42], which successfully measured 1DA from seeded IB molecules and in principle can be adapted for measuring

3DA as well. The next section will described this in detail.

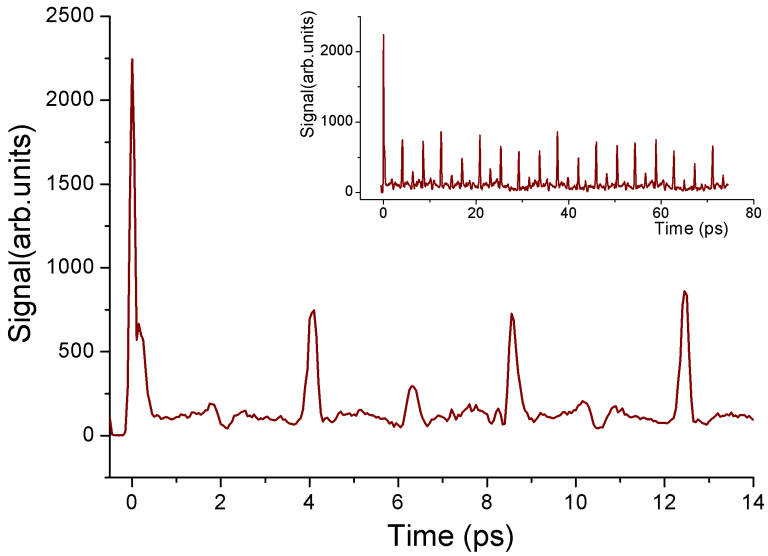

Figure 4.5: *Measured revival trace in nitrogen gas jet using transient grating. One of the probes is polarized along the Z axis, the other probe is polarized along the X axis, pump is polarized along the Z axis and signal is measured along the X axis.*

4.2 A pump-degenerate four wave mixing technique

Part of this chapter is adapted and modified from Ren *et al.,* [42].

As shown in Fig. 4.6, we use four beams instead of three for the new scheme. The three beams for generating transient grating diffraction signal are still positioned at the same places on the lens, except that all three beams are now fixed in both space and time, therefore the signal beam is present during the entire experiment. To further simplify the setup, a metal plate with three holes at the correct phase matching position is used to split an expanded probe beam into three, giving us a two beams setup rather than four, simplifying the experiment. The resulting DFWM signal is proportional to the square of the polarization of the signal's light field (see App. B for the derivation), which can be expressed as

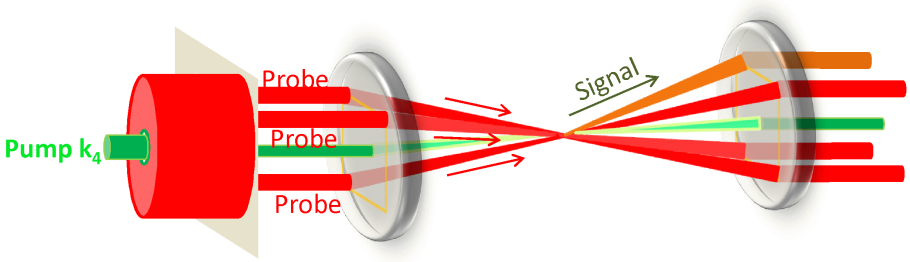

Figure 4.6: *A demonstration of the pump-degenerate four wave mixing setup, see text for details.*

$$P_i^{(3)} = \chi_{ijkl}^{(3)} E_j E_k E_l^*, \tag{4.1}$$

where i, j, k, l correspond to signal and three probes respectively, $\chi_{ijkl}^{(3)}$ is the third-order susceptibility tensor in the LF and $E_{i,j,k,l}$ are the electric field of all four pulses.

An extra pump beam is introduced in this new scheme. It aligns the molecules and causes changes to the nonlinear susceptibility in the the LF. By delaying all three probes together, such changes can be measured, which in principle is related to the alignment of all three axes. The LF third order susceptibility tensor can be obtained by rotating the MF hyper-polarizability tensor γ_{mnop} into the the LF using rotational matrices. m, n, o, p cycle through the MF x, y and z axes. See App. B for more detail.

$$\chi_{ijkl}^{(3)} = N\epsilon_0 \left\langle R_{im} R_{jn} R_{ko} R_{lp} \right\rangle \gamma_{mnop}, \tag{4.2}$$

where R_{ij} are elements of the rotational matrix, N is the number density of the molecules, ϵ_0 is the vacuum permittivity and the expression is summed over repeated indices. To get the expression for $\chi_{ijkl}^{(3)}$ and calculate the evolution of the DFWM signal, we pick out the unique nonzero elements of the hyperpolarizability tensor in the ground vibronic state [75], specifically, γ_{zzzz}, γ_{xxxx} and γ_{xxzz} for linear molecules; γ_{zzzz}, γ_{xxxx}, γ_{xxzz} and γ_{xxyy} for symmetric tops; γ_{zzzz}, γ_{xxxx}, γ_{yyyy}, γ_{xxzz}, γ_{xxyy} and γ_{yyzz} for asymmetric tops. Taking into account the molecular symmetry and the degeneracy of the frequencies in the DFWM process, all four indices of the tensor can be permuted, adding 12 more components for

linear molecules, 14 for symmetric tops and 15 for asymmetric tops. The values of those unique nonzero elements are obtained from Ref. [76] for benzene and iodobenzene and Ref. [77] for nitrogen.

For linear and symmetric tops, after interacting with the pump laser, which is linearly polarized along Z axis, the susceptibility tensor elements do not depend on the Euler angles χ and ϕ, thus we can get the analytical express for χ_{ijkl} containing only the moments of $\cos\theta$. In the experiment, the measured signal is proportional to χ^2_{ijkl}, so, for instance, the expression of the component χ^2_{ZZZZ} for N_2 molecule is as follows (in atomic units),

$$\chi^2_{ZZZZ} = (0.47411 + 1.24106\cos^2\theta + 0.67969\cos^4\theta - 0.17338\cos^6\theta + 0.00925\cos^8\theta) \times 624187, \tag{4.3}$$

where χ_{ZZZZ} is the susceptibility tensor element with all probes polarized in the LF Z axis and the signal measured along the Z axis as well. In the experiment, the measured signal is from a rotational wave packet evolving in time. Therefore the time dependent signal $\chi^2_{ZZZZ}(t)$ can be expressed by replacing $\cos^n\theta$, $n = 0, 2, 4, 8$, with the calculated expectation value $\langle\cos^n\theta\rangle(t)$ averaged over alignment distribution and thermal population.

For asymmetric tops, the interaction involves Euler angle χ, therefore expression for the χ_{ijkl} is a sum of the product of $\langle\cos^n\theta\rangle$ and $\langle\cos^m\chi\rangle$, where $m, n = 0, 2, 4, 8$.

$$\chi^l_m = N\epsilon_0 \sum_{m'} D^l_{m',m}\gamma^l_{m'}, \tag{4.4}$$

where χ^l_m and $\gamma^l_{m'}$ are spherical components of the susceptibility and hyperpolarizability tensors, respectively. $D^l_{m',m}$ are the Wigner matrices. For third-rank tensors, $l = 0, 1, 2, 3, 4$ and $m = -l, -l+1, ..., l-1, l$. In the symmetric top basis $|JKM\rangle$, the matrix elements $\langle JKM|\chi^l_m|J'K'M'\rangle$ are easy to calculate. Transforming the results back to Cartesian basis gives the matrix elements for the required Cartesian susceptibility component in the $|JKM\rangle$ basis. As discussed in Chap. 1, TDSE calculation for asymmetric tops are also performed in $|JKM\rangle$ basis, thus the time evolution of different susceptibility tensor elements can be

calculated and compared to the experiment.

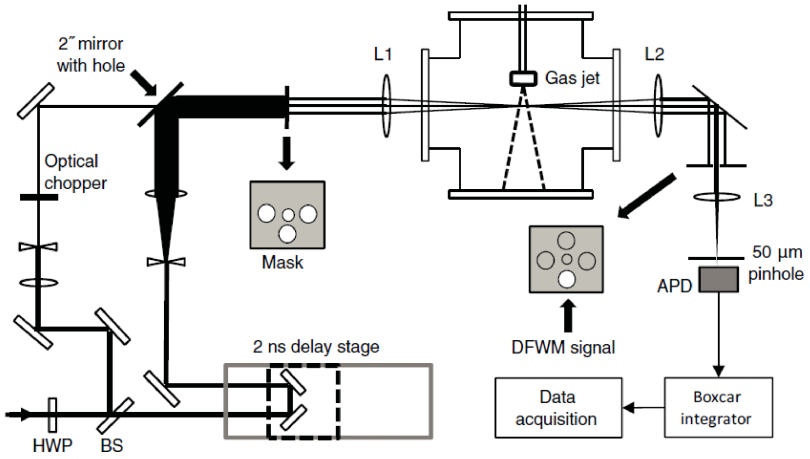

Figure 4.7: *Experimental setup for the pump-DFWM experiment, see text for details.*

The experimental setup is shown in Fig. 4.7. The KLS beam splits into pump and probe arms, the probe beam goes through an automatic delay stage and then gets expanded using a telescope to double the beam size. The expanded probe then reflects off a 2 inch mirror with a 6 mm hole in the center and lands on the 2 inch metal plate, the plate picks out 3 small beams from the probe in the correct phase matching positions for DFWM which are focused using a 35 cm lens (L1) into the chamber. The pump arm goes through the center holes on both the 2 inch mirror and metal plate to recombine with the probes non-collinearly. In order to increase gas density, we focus all the beams right in front of the jet. The pump aligns the target from the jet causing changes to the susceptibility tensor of the target, the probes are delayed to generate DFWM signal at each moment after the initial alignment. The output is filtered using another metal plate with a hole in the position of the signal beam to reduce any scattered light. The signal is then collimated by another lens (L2) and focused (by L3) into an avalanche photodiode detector. A boxcar integrator is used to collect the data, which is sent to a computer for further analysis. A 50 μm pinhole is placed at the focus, which is also the image position of the interaction region. This allows us to select signal generated from the most intense part of the pump beam where the highest

degree of alignment is obtained. The detrimental effects of focal-volume averaging are, thus, also minimized. Later on, simulations without intensity averaging are shown to agree well with the experimental data.

In order to increase the signal to noise ratio as well as normalizing the measurement. We add an optical chopper in the pump beam, which chops the beam at 500 Hz, since the laser has a repetition rate of 2 kHz and the gas jet runs at 1 kHz, we have four distinct combinations of gas and pump beams (the probe is always present): (a) Gas jet is on and pump is not blocked. (b) Gas jet is on and pump is blocked. (c) Gas jet is off and pump is not blocked. (d) Gas jet is off and pump is blocked. Thus, we have four different kinds of signals in every cycle consisting of four laser pulses: (a) DFWM signal from the aligned target gas and scattered light from both pump and probe beams, which we call signal A, where $A = (\chi_{ijkl} E_j E_k E_l^*)^2 + S_{\mathrm{pu}} + S_{\mathrm{pr}}$. (b) DFWM signal from unaligned target gas and scattered light from probe only, which we call signal B, where $B = (\chi_{ijkl-iso} E_j E_k E_l^*)^2 + S_{\mathrm{pr}}$. (c) Scattered light from both pump and probe, which we call signal C, where $C = S_{\mathrm{pu}} + S_{\mathrm{pr}}$. (d) Scattered light from only probe beams, which we call signal D, where $D = S_{\mathrm{pr}}$. By doing a simple algebra—$(A - C)/(B - D)$—we can get rid of the scattered light and get the normalized signal $S_{ijkl} = \chi^2_{ijkl}/\chi^2_{ijkl-iso}$. In this way, the average number of molecules in the laser focus, the volume of the focus and the intensity of the probe beams are all factored out providing a calibrated measurement of the third-order susceptibility of the target molecules. The data shown below were all averaged over 1000 cycles to overcome shot-to-shot fluctuations of the laser power and the gas density fluctuations.

We start with a simple linear molecule: nitrogen. The measured trace is shown in Fig. 4.8. We set all probe beams to be polarized along the LF Z axis and measure the Z axis component from the signal to extract the normalized χ^2_{ZZZZ} trace. Before the pump laser aligns the molecule, the probes see an isotropic distribution, so the normalized signal equals 1. Fig. B.1 in App.B shows that for N_2, χ^2_{ZZZZ} increases with the alignment, as observed in the experiment. By performing a TDSE calculation using the experimental

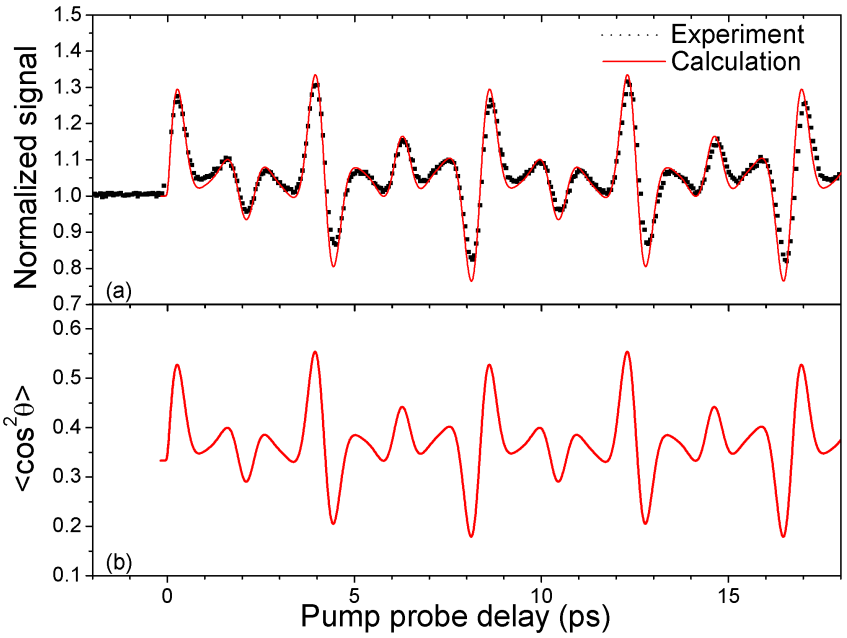

Figure 4.8: *Panel (a): Pump-DFWM trace of the normalized χ^2_{ZZZZ} component from aligned N_2 molecule. Both experiment and simulation are plotted. Panel (b): The corresponding $\langle\cos^2\theta\rangle$ trace. Both experiment and calculation use a pump laser with 60 fs and 30 TW/cm^2, a rotational temperature of 20 K gives the best agreement. No intensity averaging is included in the calculation.*

laser parameters, we can theoretically fit Eq. 4.3 to the data, with an estimated rotational temperature of 20 K, which agrees with the experiment quite nicely. The maximum value of $\langle\cos^2\theta\rangle$ occurring at the revival peak is 0.55.

The next step is to lower the gas density and try more complicated molecules. Benzene, a symmetric top, is the second target we tried. The measured and calculated revival traces are shown in Fig. 4.9. In experiment, a small amount of liquid benzene is placed inside the gas jet and carried out by 70 bar of helium gas, the vapor pressure is about 360 mbar at 50 ^{o}C, which is much lower compared to 70 bar backing pressure of neat nitrogen in the previous case. The agreement between experiment and calculation is pretty good, giving a maximum value of about 0.6 for $\langle\cos^2\theta\rangle$. There are some very tiny one-third, one-fourth and one-eighth revivals in the calculated trace, but those are too small in magnitude to be seen in the measurement. One feature that is worth mentioning is that for all the alignment traces

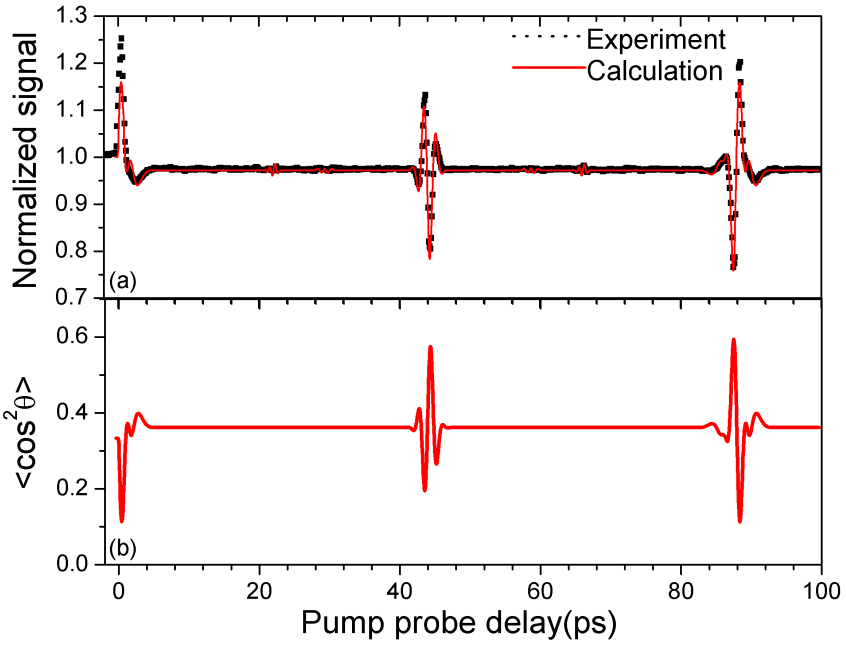

Figure 4.9: *Panel (a): Pump-DFWM trace of the normalized χ^2_{ZZZZ} component from aligned C_6H_6 molecule. Both experiment and simulation are plotted. Panel (b): The corresponding $\langle\cos^2\theta\rangle$ trace. Both experiment and calculation use a pump laser with 130 fs and 15 TW/cm^2, a rotational temperature of 35 K gives the best agreement. No intensity averaging is included in the calculation.*

shown previously (except for Fig. 1.3, which is also benzene), there is a constant baseline up shift after the initial alignment (if the initial alignment goes up). It is the incoherent alignment, which happens when the laser populates very high J states so that $\langle J^2\rangle \gg \langle M^2\rangle$ [78], therefore, the angular momentum vector of the molecules are more distributed in the XY plane or in another word, molecular axes are more confined to Z axis even at moments when there are no revivals. However, for benzene and any other oblate symmetric tops with the least polarizable axis along the symmetry axis, as previously discussed in Chap. 1, the symmetry axis is driven away from the laser polarization direction, causing $\langle\cos^2\theta\rangle$ to decrease. For linear molecules incoherent alignment results in alignment of the molecular axis with the laser polarization. However in the case of benzene, incoherent alignment leads to planar alignment—the molecular plane is weakly confined to the plane perpendicular to the laser polarization, which causes an upward shift (in the opposite direction of the initial

alignment) in $\langle\cos^2\theta\rangle$. Since χ^2_{ZZZZ} goes in the opposite direction to the alignment (see App. B), we see an incoherent down shift in the χ^2_{ZZZZ} trace.

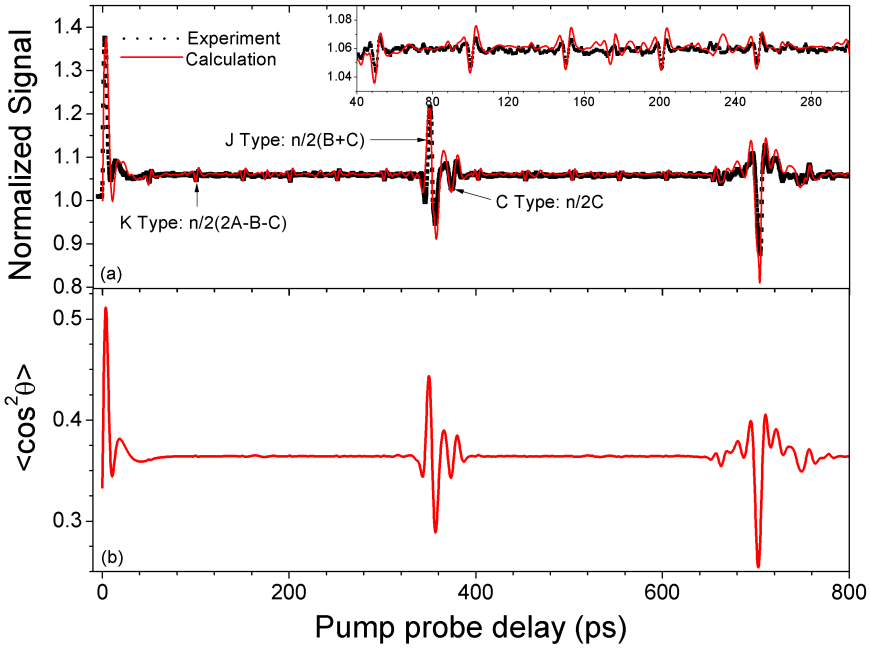

Figure 4.10: *Panel (a): Pump-DFWM trace of normalized χ^2_{ZZZZ} component from aligned C_6H_5I molecule. Both experiment and simulation are plotted. Panel (b): The corresponding $\langle\cos^2\theta\rangle$ trace. Experiment is performed with a 60 fs, 18 TW/cm^2 pump and calculation uses a pump laser with 60 fs and 15 TW/cm^2, a rotational temperature of 8 K gives the best agreement. No intensity averaging is included in the calculation, although the calculation is using a slightly lower intensity to account for a little bit of intensity averaging.*

Finally, iodobenzene molecules are investigated using this technique. Again it is a liquid and seeded in high pressure helium gas through the jet. The vapor pressure is much lower than benzene, about 18 mbar at 70 ^{o}C. Fig. 4.10 shows the measured and calculated normalized signal of the $ZZZZ$ component. $\langle\cos^2\theta\rangle$ is estimated to be about 0.51 at initial alignment peak. Other than the J-type and C-type revivals that we always see in VMI experiment (see Chap. 3), surprisingly, very clear K-type revivals also show up at the expected times (see Tab. 1.1), which indicates that this measurement is sensitive to rotations about all three axes in asymmetric top molecules and may be capable of measuring 3D alignment as well. Note that the estimated temperature is about 8 K, which is much higher than the

one in VMI (about 1 K). That is because these measurements are performed right in front of the jet and we do not expect the cooling process to be complete.

4.3 A pulse shaping setup to enhance FF1DA

In the previous section, we have demonstrated that, the pump-DFWM scheme is capable of measuring alignment from an extremely low density gas target and in principle, should be able to measure alignment from all kinds of molecules, since all molecules have susceptibility tensors that will change when alignment occurs. Furthermore, since we have one single quantity, for example χ^2_{ZZZZ}, that changes monotonically with the degree of alignment, we could shape the aligning pulse and use an optimization algorithm to improve the alignment level.

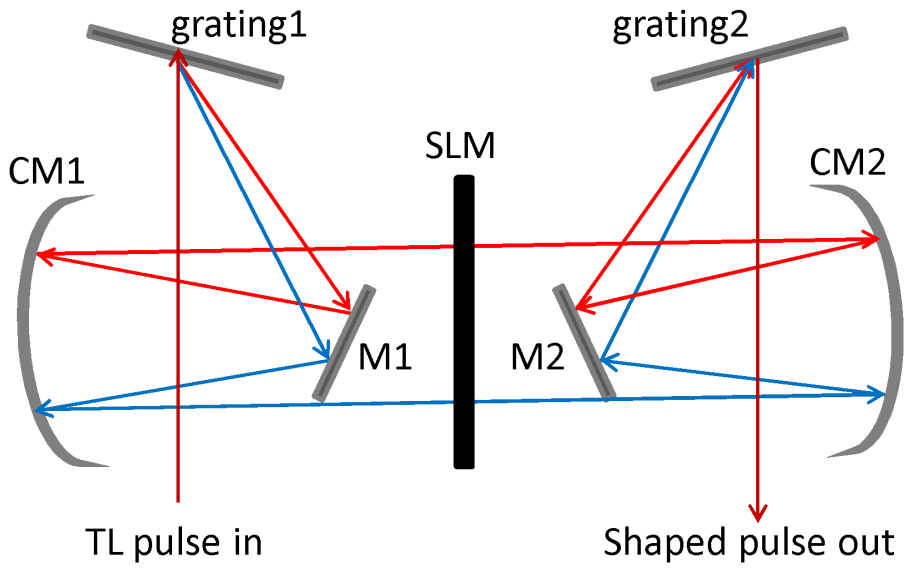

Figure 4.11: *A pulse shaper is inserted into the pump beam in the pump-DFWM setup.*

Such an optimization setup is shown in Fig. 4.11. The pulse shaper is a typical 4-f system [79, 80]. We use cylindrical mirrors instead of spherical lenses to reduce astigmatism as well as increasing the amount of power that can go into the system since cylindrical mirrors only

focus in one direction. A transform limited (TL) and collimated laser pulse goes into the system, a grating with 1200 lines/mm groove density disperses the frequencies within the laser bandwidth. Grating 1 is set to be tilted so that the dispersed beam goes down and hits mirror 1 (M 1), then the beam gets raised and lands on the 35 cm focal length cylindrical mirror 1 (CM 1). By doing so, we get horizontal dispersion on CM 1. The distance from grating 1 to CM 1 is 35 cm. CM 1 collimates the dispersed beam as well as focusing each frequency component 35 cm away, where a spatial light modulator (SLM) is placed.

Our SLM is a dual mask 640-pixel model, allowing phase, intensity and polarization to be shaped. The basic idea is that both masks contain an array of 640 liquid crystals with optical axes all along 45 degree (for mask 1) and –45 degrees (for mask 2) with respect to the LF Z axis. When a Z polarized (more efficient on the grating) pulse comes in, by adding voltages on each of the 640 liquid crystals on both masks, the refractive index of the crystals along their optical axes will be modified. If the voltages on both masks are the same, laser components along $+45$ and -45 degrees see the same amount of refractive index change, therefore a constant phase will be added on the frequency component within every single liquid crystal pixel while still maintaing the polarization of the laser. If the voltages on both masks are not the same, there will be a phase difference between the $+45$ and -45 degree components, polarization shaping is therefore achieved. By careful design and calibration of the system, we can change the phase of each frequency component within the laser bandwidth to great precision.

After the SLM, all the modified frequencies go through the reversed setup (focused using CM 2, reflected on M 2 and combined on grating 2) and get converted back to time domain to form the shaped laser pulse. The phase changes in the frequency domain will result in changes of the laser pulse in the time domain. For instance, a linear phase will result in a time shift of the output pulse, a second order phase will cause broadening of the pulse and so on. A test of how different phases on our SLM affects the output laser pulses is plotted in Fig. 4.12. Second harmonic (SH) traces are obtained by performing

cross-correlation measurements of the pump pulse (shaped or unshaped) and the transform limited (TL) probe pulse. Features corresponding to the effect of adding linear phase (time-delayed pulse), second-order phase (pulse broadening), third-order phase (ringing structure on one side) and fourth-order phase (side peaks) can be seen in panels (a), (b), (c) and (d) respectively.

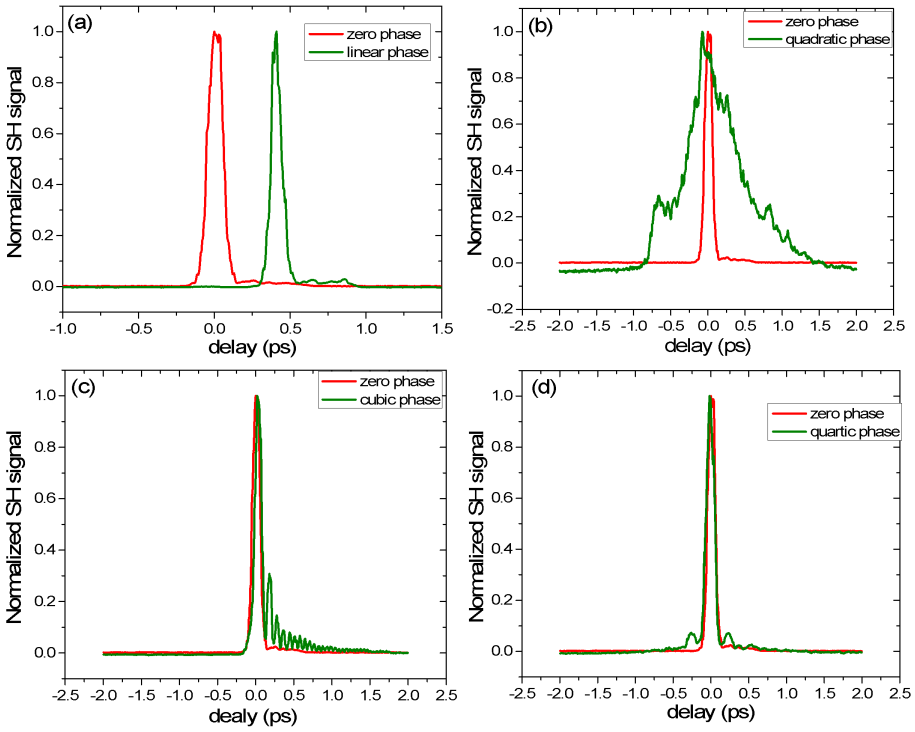

Figure 4.12: *The cross-correlation of the output pump pulse and a transform limited probe pulse with (a) first order, (b) second order, (c) third order, (d) forth order phases on the our SLM. All the second harmonic signals have been normalized to their peak values.*

After building a working pulse shaping setup, we attempted some optimization experiments. Before jumping directly into alignment optimization, we started with optimizing the laser pulse duration. First, the shaper was aligned so that the system had minimum dispersion—a TL pulse (∼30 fs) goes in, a near TL pulse will come out. Then, dispersive optics were introduced in the beam path after the shaper to stretch the output pulse. The stretched pulse was focused together with the TL probe pulse into a BBO crystal to gen-

erate a SH signal at the overlap. In order to shorten the pulse, we feed this SH signal into a genetic algorithm as the fitness function. Using the phase at each pixel as the gene, an interpolated array of 640 phases as the genome of one individual we iterate the algorithm to try and increase the fitness. Within about 100 generations, we successfully compressed the stretched 200 fs pulse down to about 50 fs, as shown in Fig. 4.13.

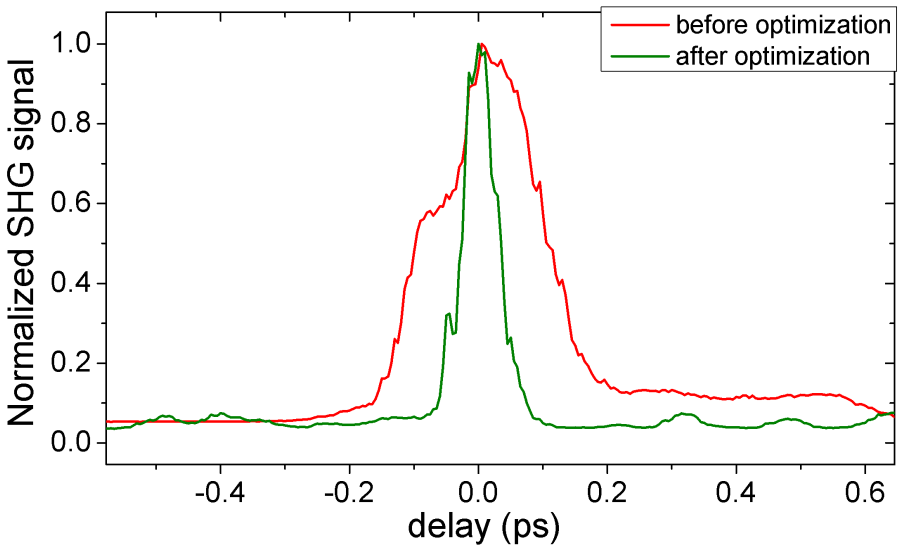

Figure 4.13: *The cross correlation of laser pulses before and after the optimization are shown.*

In order to optimize alignment, we replace the fitness with the DFWM signal from a molecular gas and try to increase or reduce it. However experiments with nitrogen and iodobenzene proved unsuccessful. The former requires a lot of pulse energy for better alignment, which we are unable to supply due to the damage threshold of the SLM. The latter has poor signal to noise ratio due to the low gas density resulting in too much signal variation with changing number density precluding a long enough optimization run. Therefore, we chose the asymmetric top toluene molecule as the target, which has higher vapor pressure and is still reasonably polarizable requiring less pulse energy than nitrogen to align well.

Since the alignment trace has a huge spike at zero-delay signifying pulse overlap, the χ^2_{ZZZZ} component cannot be used as the fitness as it will cause the algorithm to opti-

mize the time overlap of the pump and probe rather than alignment from the pump. Instead we measure the χ^2_{XXXX} component by rotating polarizations of all beams to X axis, since the zero-delay spike goes up while χ^2_{XXXX} goes down at alignment peak, we use $1-\chi^2_{XXXX}/\chi^2_{XXXX-iso}$ at the alignment peak as the fitness and the results are shown in Fig. 4.14.

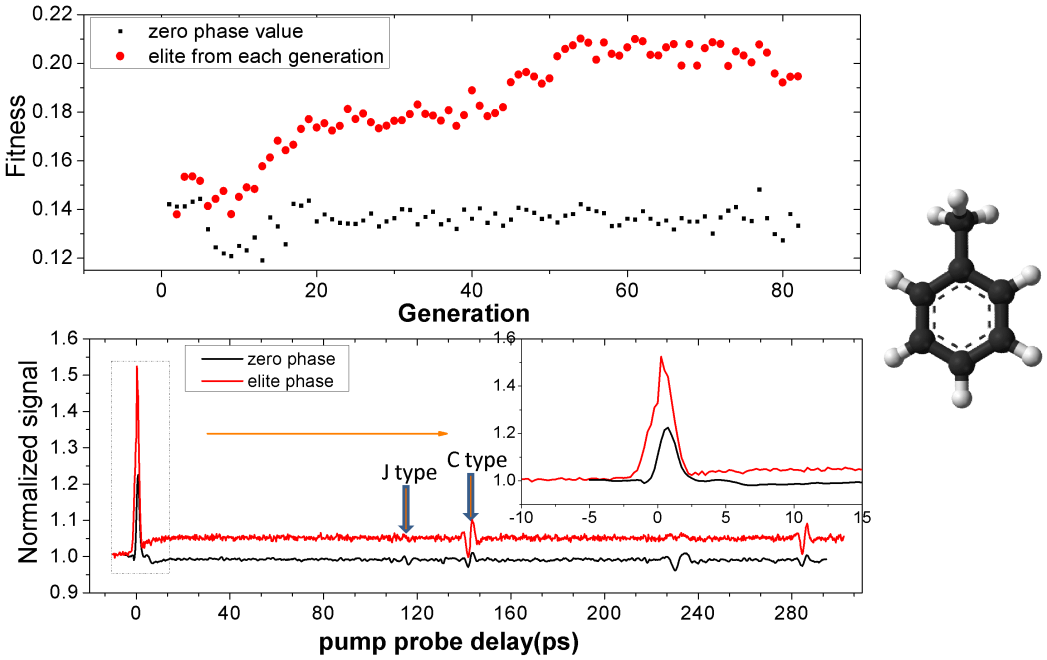

Figure 4.14: *Results from optimizing alignment of toluene molecules using our pulse shaping setup. Top panel shows how the value of* $(1-\chi^2_{XXXX}/\chi^2_{XXXX-iso})$ *changes as a function of generation numbers, zeros phase values are also plotted at the same generation. Lower panel shows both scans from the unshaped pump pulse and the pulse that gives the best fitness. The unshaped pulse has a pulse duration of 60 fs and intensity of 18* TW/cm^2*. The structure of the toluene molecule is shown on the right side.*

We can see from the figure that within 80 generations, the best value of each generation — the elite — shows a clear increasing trend until it reaches about a factor of 1.4 greater than the unshaped pulse value. In each generation, a value of the unshaped pump pulse, or the zero phase value, is also recorded, which tells us that it is actually the alignment that is improving and this is not an effect of the number density fluctuations. We also measured the normalized χ^2_{ZZZZ} trace for laser pulses with both zero phase and elite phase. The

increment of alignment level in the latter case is obvious and dramatic. The initial alignment peak increases from 1.2 to almost 1.55. The more convincing features that indicate better alignment are the big DC jump after initial alignment and the enhancement of the C type revival along with a reduction in the J type revivals, which all indicate a higher population of rotational states, therefore better alignment [81].

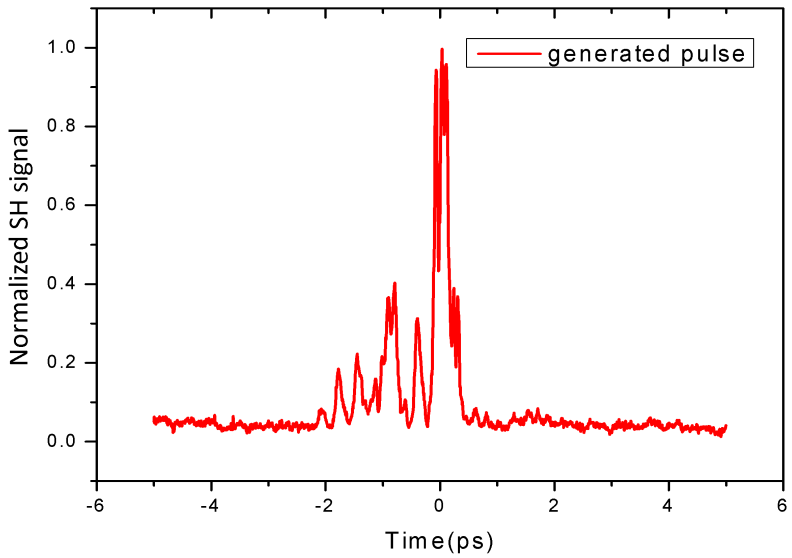

Figure 4.15: *Cross-correlation of a TL pulse and the optimum pulse from the optimization.*

The cross-correlation of the optimum pulse with a TL pulse is shown in Fig. 4.15. Even though we can not explain it fully, it does have features that have been proven to be able to increase alignment, such as a pulse train with a cubic like phase, whose pulse energy gradually increases [82]. More theoretical work needs to be done to find out why this particular pulse gives much better alignment.

As mentioned at the end of Sec. 4.1, since DFWM measures rotations about all three axes of an asymmetric top molecule, in principle, it could be used to measure 3DA. Ideally, we want to find a single quantity, like χ_{ZZZZ} for 1DA, to represent 3DA. There are totally four independent non-zero third-order susceptibility tensor elements that could be measured in an experiment: χ_{ZZZZ}, χ_{XXXX}, χ_{ZZXX} and χ_{XXZZ} (those including the Y axis require a cross pump probe setup which can be done but is cumbersome). Can we somehow find

3DA information in one of those components? Or is it hidden in combinations of those components? Those are questions that require further investigation and the answers might be able to link the proposed metric for 3DA (see Chap. 3) to an observable that can be measured in experiment.

So far, all that has been discussed is how to induce and measure FF1DA and FF3DA, which merely serves as a tool for many other experiments. The next few chapters will demonstrate some of the applications of aligned molecular distributions emphasizing experiments on high harmonic generation with aligned molecules carried out in our lab.

Chapter 5

High Harmonic Generation from aligned molecules

5.1 Introduction to high harmonic generation

High harmonic generation (HHG) [11, 12], the process of generating new frequencies that are high order integer multiples of the driving laser frequency, has been studied extensively over the past two decades since the development of high intensity femtosecond lasers. It is often referred to as a table top soft X ray source. As a result of the extremely broad spectrum, it also initiated the whole field of attosecond laser science [83–86].

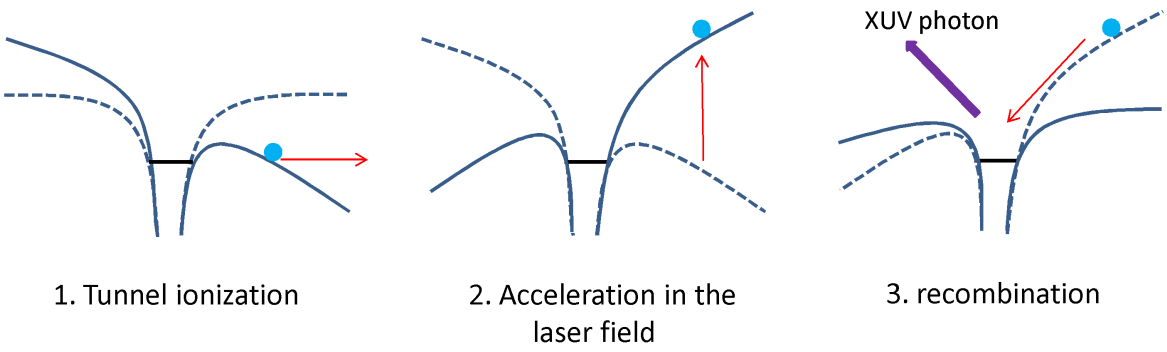

Figure 5.1: *Three step model for HHG, adapted from [87].*

The generation of high order harmonics can be explained by the well known semi-classical three-step model [11, 12] as illustrated in Fig. 5.1. When an intense laser interacts with an atomic or molecular target, beyond a certain intensity limit in the so called tunneling regime,

the Coulomb potential of the atomic or molecular ions will bend causing the outermost electron to tunnel out through the barrier. In the second step, the ionized electron is accelerated by the electric field. As the electric field reverses direction, the electron will move back towards the parent ion. In the third step, the returning electron recombines with the parent ion releasing the energy gained in the laser field as Extreme Ultraviolet (EUV/XUV) photons, referred to as harmonics.

There are several properties of HHG:

1. Harmonics are emitted every half cycle of the laser field. A Fourier transformation of such a pulse sequence to the frequency domain gives harmonic orders that are spaced by $2\omega_0$, where ω_0 is the fundamental frequency of the driving field. Thus, starting from the fundamental, there are only odd order harmonics. However, if we overlap the fundamental with its second harmonic field, for example by using a phase synchronized 800 nm+400 nm two-color field, we can break the symmetry of the electric field and generate harmonics once every cycle, thus even order harmonics are obtained [88–90]. Another way of obtaining even order harmonics is to break symmetry of the molecular target, this has also been demonstrated recently by generating harmonics from oriented carbon monoxide molecules [28].

2. For harmonics in the perturbative regime, for instance, third order, fifth order and so on, the intensity of those harmonics will reduce dramatically with increasing harmonic order. However, in the non-perturbative regime or higher order harmonics, surprisingly a plateau region is formed with the harmonic intensity staying flat for many orders. The region following the plateau where the harmonics die away quickly is called the cutoff. The maximum photon energy that can be generated is calculated from the cutoff law [11],

$$E_{\mathrm{c}} = I_{\mathrm{p}} + 3.2U_{\mathrm{p}} = I_{\mathrm{p}} + 3.2\frac{e^2E_0^2}{4m_{\mathrm{e}}\omega_0^2}, \tag{5.1}$$

where I_{p} is the ionization potential from a certain orbital. U_{p} is the ponderomotive energy, which is the average kinetic energy that an electron can gain in the laser field.

3. Depending on the initial phase of the electric field at which the electrons are tunneled out, different electrons with different propagation times in the laser field can recombine with the parent ion with the same energy. Electrons which recombine earlier travel short trajectories, and those that recombine later travel long trajectories. In general, harmonics from those two quantum paths interfere and this interference has been studied [91–94]. Geometrically, short trajectory harmonics are more collimated than long trajectory ones.

4. HHG is a macroscopic process, each atom or molecule in the laser interaction region will emit XUV photons with different phases, when the fields add up constructively, the harmonics are phase matched. Phase matching is a very complicated and sensitive process. Laser focusing condition, laser beam profile (Gaussian, Bessel, truncated or others), gas density and gas profile will all affect phase matching [95–97].

5. Harmonic generation provides a train of attosecond pulses [98]. Fervent research in the past few years has been focused on generating isolated attosecond pulses in order to drive the ultrafast science into a regime where electron dynamics can be directly probed. Various techniques have been developed, such as harmonic generation from phase stabilized, few cycle laser pulses with the polarization gating technique [99], in which two opposite handed circularly polarized pulses are partially time overlapped so that harmonics are generated at the overlap region. By adding a weak two color field, the so called double optical gating technique, can be used with multi-cycle driving pulses [100, 101].

6. Harmonic intensities are strongly dependent on the driving field wavelength λ. It has been established that harmonic intensities scale as $\lambda^{-5} \sim \lambda^{-6}$ [102–106], therefore, as the wavelength decreases, harmonics will get much more intense. This is useful to obtain more pulse energy for the attosecond bursts. However, as we can see in Eq. 5.1, the cutoff energy will be greatly reduced with the use of short wavelength lasers. In order to generate high cutoff or high energy photons, we actually need to use a long wavelength laser. So far, photon energy beyond 500 eV has been achieved using near-infrared 800 nm source on a helium target [107]. By going into the 1.5 μm $\sim$ 3 μm regime, multi-keV photons can be

obtained from helium [108].

Soon after the three-step model was proposed, a quantum mechanical treatment was used to simulate the HHG process [109]—the Lewenstein model or, more commonly, the strong field approximation (SFA). This model neglects the interaction of the electrons in the continuum with the parent ion and agrees well with experiments for near cutoff harmonics but not for lower plateau harmonics [110]. A quantitative rescattering (QRS) theory developed by Chii-Dong Lin's group [111] expresses the harmonic dipole as a product of a returning electron wave packet and the photorecombination cross section (PRCS) of the laser-free continuum electron coupling back to the initial ground state. Since photorecombination is the time-reversed process of the photoionization under field-free conditions, we can use the photoionization cross section (PICS) instead of PRCS in the model.

In the case of a fixed-in-space molecule, under the assumption of QRS, we can write down the expression for the energy and angle dependent induced dipole moment as follows [112]

$$D(\omega,\theta) = \sqrt{N(\theta)}W(\omega)d(\omega,\theta). \tag{5.2}$$

where θ is the angle between the laser polarization axis and molecular axis, $N(\theta)$ is the molecular frame tunneling ionization rate, $W(\omega)$ is the returning electron wave packet and $d(\omega,\theta)$ is the photorecombination transition dipole. Both $N(\theta)$ and $W(\omega)$ can be calculated using molecular SFA [113, 114] while $d(\omega,\theta)$ is independent of laser conditions and can be calculated using a state of the art molecular photoionization code [115, 116]. Depending on whether the parallel component $D_{\parallel}(\omega,\theta)$ or perpendicular component $D_{\perp}(\omega,\theta)$ (with respect to the driving field polarization direction) is calculated, $d_{\parallel}(\omega,\theta)$ and $d_{\perp}(\omega,\theta)$ should be used correspondingly. So far, this theory is able to reproduce numerous measured features of HHG including intensity, phase and polarization [111, 117, 118].

Apart from the development of theory, the experimental side has been divided mostly into two parts. One focuses on developing new sources, either shorter or more intense

attosecond pulses or XUV photons with very high photon energies. This part of the research is focused on the study of HHG from noble gas molecules. The other part focuses on studying properties of the target such as molecular electronic orbital structure and dynamics using HHG, especially in aligned molecules. The underlying mechanism is that HHG from molecules strongly depends on the electron density distributions, which in the LF depend on how the molecules are oriented. Furthermore, the radiation of different harmonic orders happens when electrons spend various amounts of time in the laser field before recombining to the parent ion, thus the change in geometry of the parent ion, if there is any, will be encoded in different harmonic orders. To date, multi-orbital structures of various molecules have been successfully measured or retrieved [31, 32, 119, 120] along with a few experiments that probe molecular dynamics [37, 121]. Since QRS suggests that the recombination step is simply related to PICS, using HHG to extract PICS has recently become a very interesting topic in the field [122–124].

The amount of information that can be extracted from HHG measurements and its quality depends strongly on the degree of alignment that can be achieved. In most previous work, the degree of alignment — $\langle \cos^2 \theta \rangle$ — obtained with single non-ionizing laser pulses ranges from 0.5 to 0.65 for molecules like N_2, O_2 and CO_2 [32, 119, 120]. Information of the highest occupied molecular orbital (HOMO) or even lower ones has been successfully measured or retrieved with these degrees of alignment. However, sharp features in the PICS such as shape resonances and Cooper-like minima often tend to be washed out. Fig. 5.2 shows the calculated parallel component of PICS from the N_2 HOMO. The strong peak around 30 eV is a shape resonance, which is due to a resonant transition from ground $3\sigma_g$ state to continuum $k\sigma_u$ states. The dip around 55 eV corresponds to a Cooper minimum, resulting from the fact that the wave-function of a continuum electron can be written as a coherent superposition of partial waves, among which the p (l=1) and f (l=3) partial waves interfere destructively [124]. It is clear that both features are very narrow in angle, especially the Cooper minimum. So far, no direct observations have been reported although

some of the features can be obtained indirectly after some theoretical analysis [124, 125]. In order to directly observe those features, we use two laser pulses to improve the alignment of N_2 molecules (see Chap. 1 for more detail). Details of the experiment and the results will be discussed in the following sections.

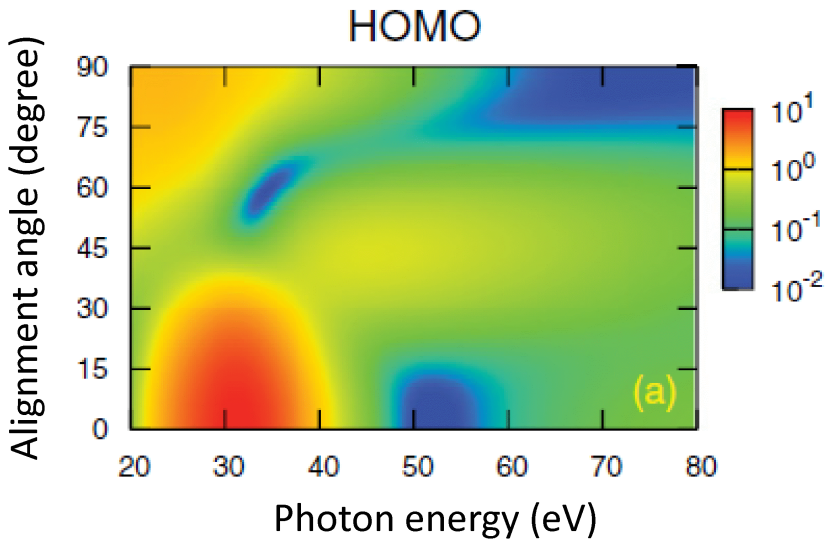

Figure 5.2: *Calculated angle and energy dependent photoionization cross section and phase from N_2 HOMO, only parallel component is shown, adapted from [126].*

5.2 Experiment and calibration of HHG spectrometer

The experimental setup is shown in Fig. 5.3. The experiment is performed right in front of the gas jet—the same position as in the DFWM experiment, where gas density is high. Pulses from KLS are again split into pump and probe arms. The probe arm goes through the motorized 2 ns delay stage, reflects off a half inch mirror in the center of a 2 inch aluminum block and focuses into the dense gas target through a 35 cm lens to generate harmonics. The generated harmonics travel into another chamber, passing through a 1 mm slit — which is used to filter most of the IR light — and then diffracted off a grazing incidence flat-field grating to form a HHG spectrum, which is then detected using a microchannel plate with a phosphor screen and a 14-bit CMOS camera. A typical HHG spectrum for N_2 is shown

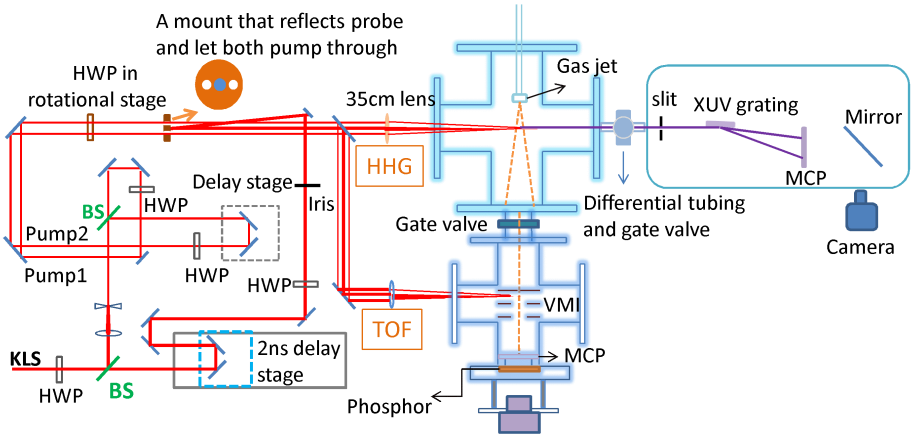

Figure 5.3: *Experimental setup for HHG experiment, see text for details.*

in Fig. 5.4. Since the harmonics in the top panel of the figure are spatially collimated, we identify them as short trajectory harmonics. Those in the bottom panel spread in the vertical direction and therefore result from long trajectories. In the experiment, we move the focus of the probe with respect to the position of the gas jet in order to pick out harmonic spectra that are dominated by either short or long trajectories [127]. We use long trajectories or a mixture of both in order to have a higher cutoff. In the spectrum there sub-peaks around the lower order harmonics. These are from second order diffraction off the grating and we discover that they can actually be used to calibrate our spectrometer. Details will be discussed in the following section.

The pump arm goes through a telescope and gets shrunk to half of the original beam size, in this way, the focal spot will be bigger than the probe focus, ensuring that the harmonics are only generated from aligned molecules. The pump beam, then, gets split again using another broadband beam splitter. The reflected beam goes though a manual delay stage and is recombined non-colinearly with the transmitted one; both beams then go through the two side holes on the 2 inch aluminum plate and recombine with the probe non-colinearly. The pumps are focused using the same 35 cm lens to align the molecules. One of the pumps is delayed by about 4 ps to kick the nitrogen molecules again at the half revival due to the

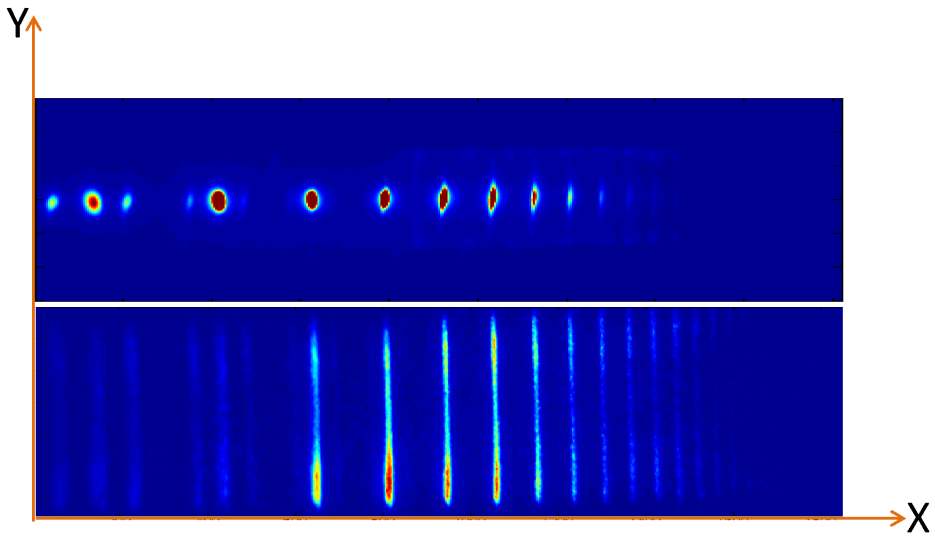

Figure 5.4: *HHG spectrum measured from N_2 molecules. Top graph shows the short trajectory and the lower one shows the long trajectory. X axis corresponds to photon energies and the Y axis shows the divergence of the harmonics.*

previous pump in order to enhance the alignment. The harmonics are then recorded at each pump probe delay to form a revival trace, an example of such trace is shown in Fig. 5.5.

In Fig. 5.5, the dips around 0 and 4 ps are due to the saturation of ionization, therefore, depletion of HHG, at the pump probe overlap. Fractional revivals at 1/2, 1/4 and 1/8 of the rotational period are clearly seen after the second pump, indicate very good alignment and confirm the sensitivity of HHG to higher order moments [41]. Due to the symmetry of the molecular orbital, Ramakrishana *et al.* [128] suggest that for the N_2 HOMO, which is a σ_g orbital, the parallel HHG component can be written as

$$S_{\parallel}(t) = \left[\sum_n a_n \left\langle \cos^{2n}\theta \right\rangle (t)\right]^2, \tag{5.3}$$

where a_n are the coefficients of different orders and $n = 1, 2, 3....$ The series is dominated by the lowest order term: $\langle \cos^4\theta \rangle$, which is averaged over the alignment distribution and initial thermal populations. The trace of $\langle \cos^4\theta \rangle$ is calculated and shown in Fig. 5.5 using experimental conditions. We can see that its structure agrees with the experiment quite

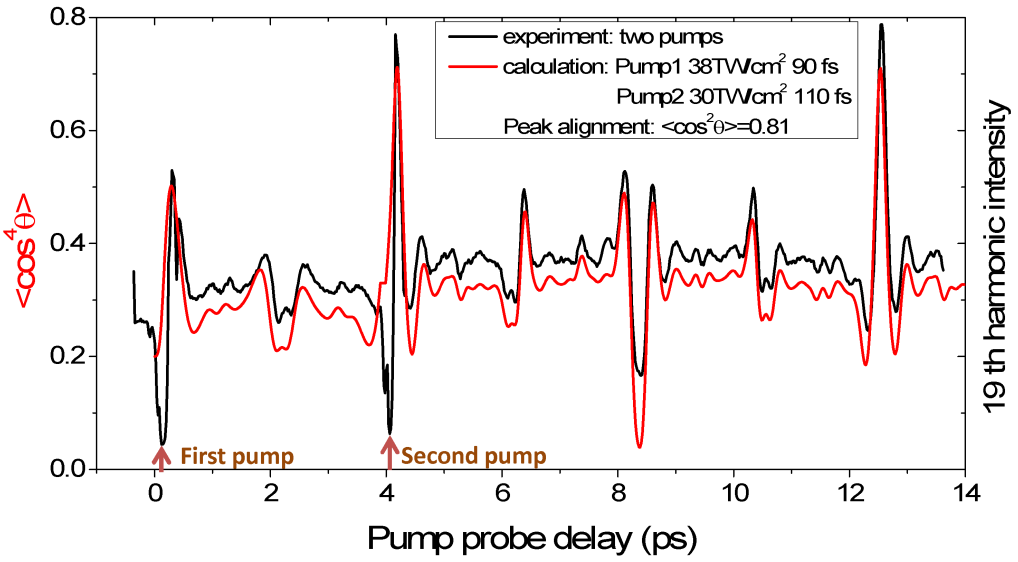

Figure 5.5: *Black line: Measured yield of harmonic 19 from aligned N_2 as a function of pump probe delay, the dips around 0 and 4 ps indicate the time when the two pumps overlap with the probe. HHG yield has been rescaled and is in arbitrary units. Red line: calculated $\langle \cos^4 \theta \rangle$ trace using the laser parameters listed in the figure.*

well. Note that even small features such as the $1/8^{\text{th}}$ fractional revivals occurring at 1.5 and 3.0 ps, are reproduced by the calculation. From the calculation a maximum $\langle \cos^2 \theta \rangle$ value of about 0.81 is achieved at around 12.5 ps. On the other hand, for an orbital of different symmetry, for instance, π_g HOMO orbital of O_2, HHG will be dominated by the lowest order of the following series,

$$S_{\parallel}(t) = \left[\left\langle \sin^2 \theta \sum_n b_n \cos^{2n} \theta \right\rangle (t) \right]^2 . \tag{5.4}$$

In order to obtain the energy axis of Fig. 5.4, we need to calibrate our HHG spectrometer. A traditional way is to use the grating equation: $d(\sin\theta_i + \sin\theta_m) = m\lambda$, where d is the grating groove density, θ_i is the incident angle, θ_m is the diffraction angle of harmonic order m, λ is the fundamental wavelength. By calculating the displacement between harmonic order m and $m-1$ on the detector and comparing it with the displacement of neighboring harmonics in experiment, we can identify the harmonic orders and therefore, calibrate the energy axis. However, this is very sensitive to the incident angle and the distance between

the grating and detector; for example, a shift in the incident angle by less than 5 degrees will shift the spectrum by one harmonic order. In order to get more precise calibration, we follow Farrell's report [129], in which plasma emission lines are used to identify each harmonic.

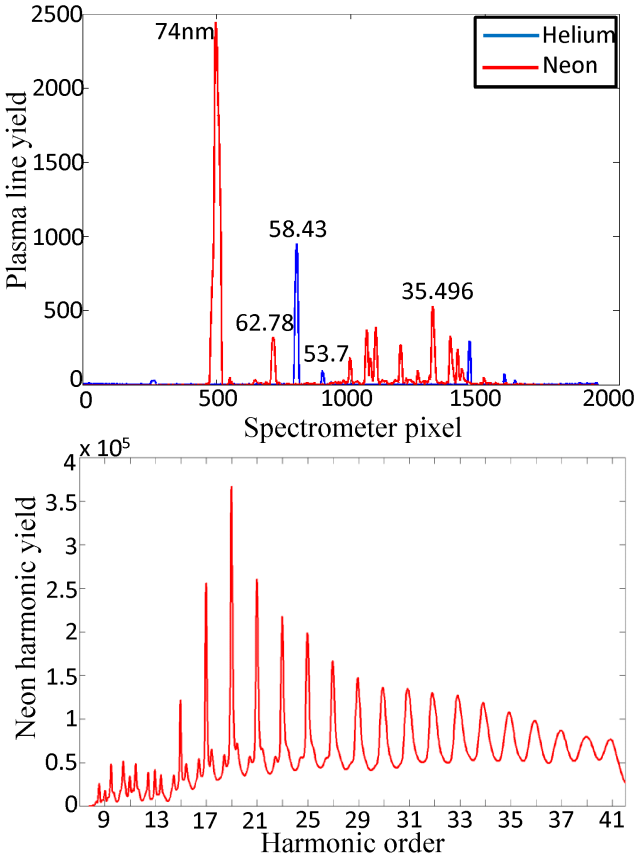

Figure 5.6: *Top panel: plasma emission lines for calibrating our spectrometer, both neon and helium gases are used. Bottom panel: calibrated harmonic spectrum from Neon.*

We add a quarter wave plate in the probe beam to make it circularly polarized in order to get rid of the harmonics and leave only the plasma lines. For circularly polarized light or light with large enough ellipticities, the electric field will drive the electrons away, causing them to miss the parent ion. Both plasma emission lines from neon and helium gas are measured and plotted in Fig. 5.6. The peaks are identified by searching through the atomic spectra from the NIST atomic spectra database [130]. The calibrated energy axis is then

used to plot the harmonic spectrum from neon. Each harmonic is identified starting from harmonic 9.

Sometimes, identifying the emission energies for different species can be a little bit tricky, because there are so many different emission energies from differently charged ions that are quite close to each other. However, we also discover a more precise way to calibrate our spectrometer by comparing the revival structures measured from the second order diffraction to the corresponding first order in a nitrogen HHG spectrum. A demonstration is shown in Fig. 5.7. We choose the peak to the left of the harmonic centered around the 600^{th} spectrometer pixel as our second order diffraction to study. By using either of the previous methods, the harmonic orders can be roughly determined within an error of one or two harmonics, so depending on whether the harmonic at pixel 600 is the 13^{th} or the 15^{th}, this second order will be associated with either the 25^{th} or 29^{th} harmonic under the corresponding energy calibration. The notation $i?j$ in Fig. 5.7 indicates ambiguity in the order of the labeled harmonic. For example, the harmonic at pixel 600 is labeled 13?15 as the previously described calibration methods identify it as *either* the 13^{th} or the 15^{th} harmonic. We plot the revival structures of the three labeled harmonics together in the bottom panel of Fig. 5.7.

By comparing the structures of the 1/8 and 1/4 revivals near 5 and 6 ps respectively, we can see that the structure of the second order match better with the structure from harmonic 25?27. For example, there is a revival at around 5 ps and a dip at the positive peak around 6 ps for harmonic 27?29, but not in the other two. Therefore, we conclude that the second order originates from harmonic 25?27, which means that the harmonic at pixel 600 is the 13^{th} harmonic.

Identifying this harmonic is very important, because there are some disagreements between two papers, one by McFarland *et al.* [120], the other one by Soifer *et al.* [131]. Both papers see strange behavior in the second harmonic (centered at pixel No. 400 in our spectrum) on their measured spectrum and we observe this as well. Briefly, for that particular harmonic, at high intensity direction of all the revivals are reversed compared to the other

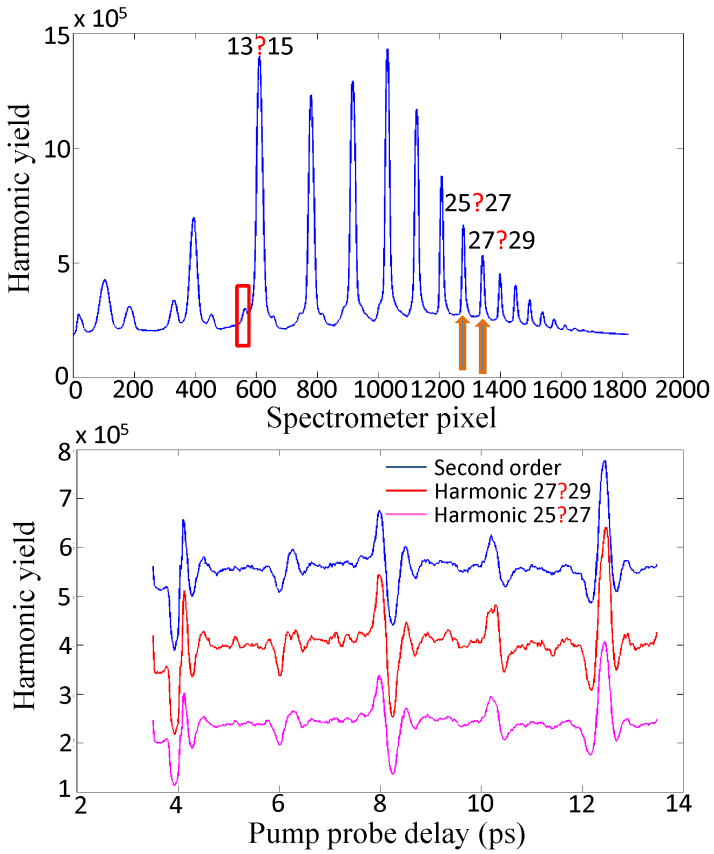

Figure 5.7: *Top panel: In this particular nitrogen spectrum, the second order to the left of the harmonic at pixel 600 is selected to compare with its corresponding first order, either the 25*$^{\text{th}}$ *or the 29*$^{\text{th}}$*. Bottom panel: Revival structures of all three, only revivals after the second kick are shown.*

plateau harmonics. As we reduce the intensity, the structure changes and finally becomes the same as the other plateau harmonics, see Fig. 5.8. Mcfarland treats it as harmonic 13 while Soifer claims it is harmonic 11. The explanation in Soifer's paper for the abnormal behavior is that harmonic 11 is very close to the N_2 ionization potential: 15.7 eV, and by changing the laser intensity, it can be shifted to below or above the ionization threshold. However, if this harmonic is the 13$^{\text{th}}$, it will be about 5 eV above the threshold, and a reduced laser intensity will not be able to shift it below the threshold. Based on our calibration, the strange harmonic is the 11$^{\text{th}}$, in agreement with Soifer's result.

The reason we can do this calibration is because H25 and H27 have distinguishable

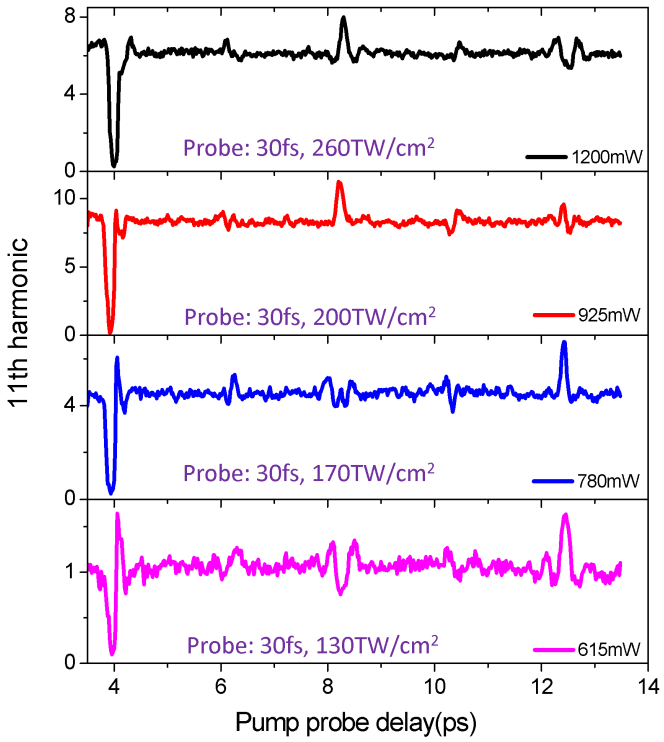

Figure 5.8: *The abnormal behavior of harmonic 11 in N_2. The revival structures after the second kick are shown for different probe intensities, at the highest intensity, the structures are reversed comparing to other harmonics, as shown in Fig. 5.7. As we go to lower probe intensities, the structure gradually reverses.*

revival structures. In fact, the differences are not only in these two harmonics, they are visible across the whole spectrum and in nearly every harmonic. These differences will be discussed in detail in the next section.

5.3 HHG from well aligned nitrogen molecules

Fig. 5.9 shows our experimental revival scans from aligned N_2 for several different harmonics orders. The time axis starts at 3.5 ps, slightly before the second pump pulse which is at 3.94 ps. This timing is chosen such that the harmonic yield (proportional to molecular alignment degree) is maximized after the second pump.

It can be clearly seen that the revival structures are different for all the harmonics.

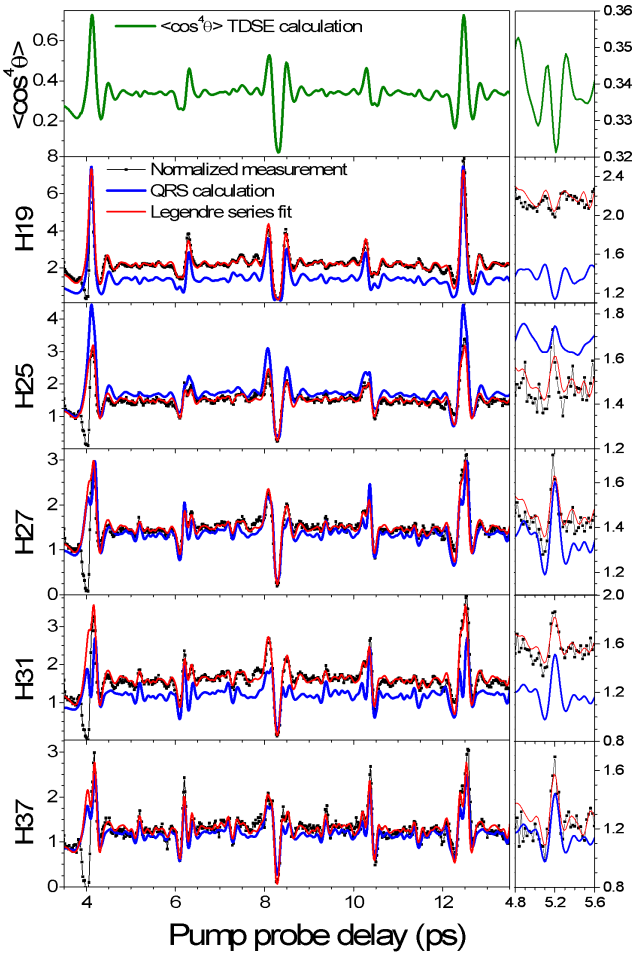

Figure 5.9: *Delay scans after the second pump. Black line shows the experimental revivals normalized to the isotropic spectrum. Blue lines show the QRS calculations and red lines show theoretical fits to the data. A* $\langle \cos^4 \theta \rangle$ *trace is also shown on the top. The right small sections are zoomed in the* $1/8^{\text{th}}$ *revivals. First pump is 80 fs, 48 TW/cm*^{2}*, second pump is 80 fs, 56 TW/cm*^{2} *and the separation between the pumps is 3.94 ps. Probe is measured to be 30 fs, 200 TW/cm*^{2}*. Molecular rotational temperature is estimated to be about 30 K.*

In particular, with increasing harmonic order, the structure of the half revival (near 8 ps) becomes sharper, the $1/4^{\text{th}}$ (near 6 ps), $3/4^{\text{th}}$ (near 10 ps) and full (near 12 ps) revivals begin to split near the alignment peak, and the direction of the $1/8^{\text{th}}$ revivals reverses gradually. All those features indicate a strong departure from the $\langle \cos^4 \theta \rangle$ trace, which is also plotted in Fig. 5.9 under the same laser conditions. It is clear that for higher order harmonics, at such a high degree of alignment, high order terms in Eq. 5.3 can not be neglected.

In order to reproduce the revival structures of higher order harmonics as well as to estimate the degree of alignment more precisely (which is previously estimated by comparing the $\langle \cos^4 \theta \rangle$ trace to the experiment), we perform theoretical fittings to all the delay scans. Instead of fitting an expansion using Eq. 5.3 [41], we fit our delay scans to an expansion of a series of Legendre polynomials [119], which in the case of linear molecules are equivalent to the Wigner D-functions with m=0. Because the laser focuses are moved away from the center of the jet in order to achieve good phase matching for the long trajectories [127], which makes it harder for measuring experimental laser focusing conditions. Therefore, we fit the laser parameters and molecular temperature as well to obtain the correct rotational wave packet. We start with fitting only H19. The harmonic intensity can be written in the form

$$I(\omega, t) = \Big[\sum_j a_j \left\langle D^j_{00}(\theta) \right\rangle (t) \Big]^2, \tag{5.5}$$

where ω is the harmonic energy, D^j_{00} are Wigner D-functions with $j = 0, 2, 4, 6$ and a_j are real coefficients. While fitting, molecular rotational temperature T, pump laser peak intensities I_1 and I_2, pulse durations τ_1 and τ_2 and the separation t_{sep} are all set to be variable within a certain window. For each combination of $(T, I_1, I_2, \tau_1, \tau_2, t_{\text{sep}})$, we solve the TDSE in the rigid rotor approximation and get the rotational wave packet. A Levenberg-Marquardt algorithm [132] is then used to fit the experimental H19 revivals and find one set of a_j coefficients. We loop through all different combinations of temperature and laser parameters to find an optimum solution, as plotted in Fig. 5.9 for H19. Therefore, we get the optimum rotational wave packet, which is then used to fit all the other harmonics. All of them fit well as shown in Fig. 5.9, the coefficients obtained from fitting all harmonics are listed in App. C. From this procedure, we get $\langle \cos^2 \theta \rangle \approx 0.82$ at the full revival after the second kick. Such a high degree of alignment is, to the best of our knowledge, the highest achieved for HHG experiments.

Note that we use real coefficients for the fitting, but the harmonic field is a complex field

with both amplitude and phase, and one should use complex coefficients in order to take into account of the phase [41]. However, mathematically it is not possible to retrieve phase from a 1D intensity scan, because there are infinite combinations of phase and amplitude that will give the same intensity. Nevertheless, Vozzi *et al.* [33] suggested that such a phase retrieval can actually work if one can fit all harmonics simultaneously and somehow link the phase for each harmonic, but this method is still under debate. In order to get the correct amplitude and phase, an additional measurement of the harmonic phase is required [32, 133]. However, we will show that, by fitting using real numbers, or in another words, assuming the phase is independent of angle, the retrieved harmonic angular distributions and PICS are actually not very much different from the theory, which suggests two possible explanations, first, the harmonics we detect at each delay are mainly coming from those molecules within a narrow ranges of angles; second, the phase of harmonics is weakly dependent on angle. Since calculation shows that the phase of the PICS is very angle dependent [126], that leaves the former explanation.

We also perform calculations using QRS theory and compare them with the measured delay scans. Good agreement is found between theory and measurement, as shown in Fig. 5.9. Therefore, we attribute the differences in all harmonics to the rich features in PICS of N_2 HOMO (see Fig. 5.2), which is included in the QRS theory. Overall most of the structures are reproduced, including the direction change in $1/8^{\text{th}}$ revivals. However, the greatest disagreement is in H19 ($\sim$ 30 eV) and H31 ($\sim$ 50 eV), which are right at the center of the shape resonance and Cooper minimum respectively. QRS predicts a much higher value at the alignment peak — almost double — for the shape resonance (the QRS calculation for H19 has been scaled by a factor of 0.5 in Fig. 5.9 for display purposes) and a lower value for the Cooper minimum. Our explanation is that QRS uses a single molecule while experimentally HHG is a macroscopic process, and each molecule will emit harmonics with a phase. At the shape resonance and Cooper minimum position, those phases will not add up perfectly constructively, which washes out both features to some extent. A

macroscopic propagation calculation is needed in order to reproduce the experiment more precisely.

5.4 Extracting Photoionization Cross Section from N_2

To see a more direct picture of the effect from PICS, we perform an angle scan at the full revival after the second pump at the alignment peak by rotating both pumps with respect to the probe using a half wave plate and measure the HHG spectrum at each angle. Scan from 0 to 360 degrees with a step size of 4 degrees is shown in Fig. 5.10,

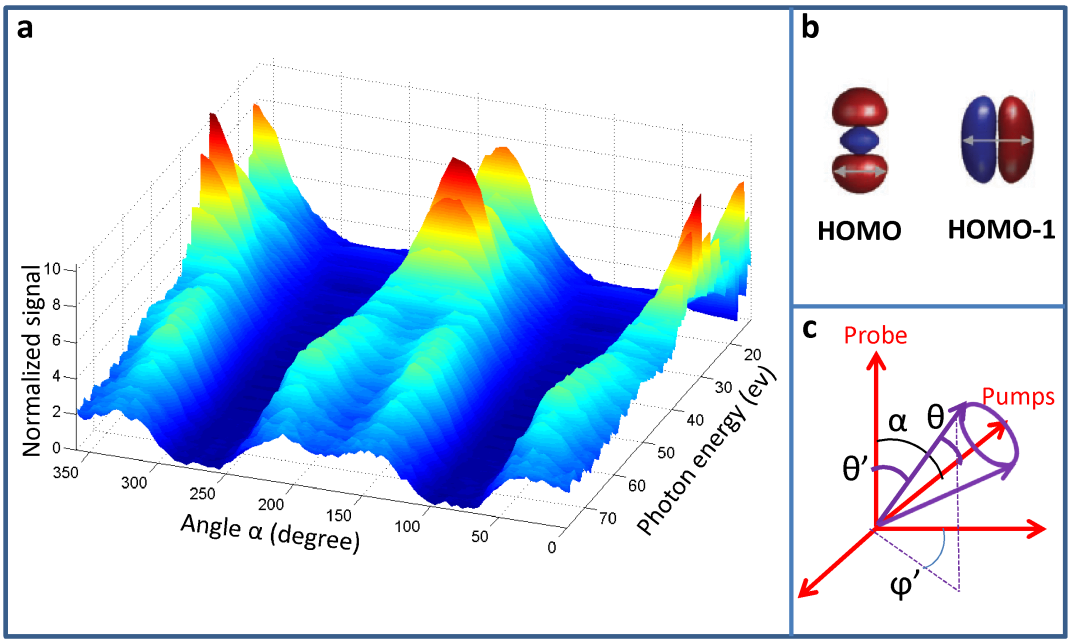

Figure 5.10: *Panel (a): angle scans at alignment peak for different harmonics as a function of photon energy and pump probe angle α, signal has been normalized to isotropic spectrum. Panel (b): orbital structures of both HOMO and HOMO–1 of N_2, adapted from [120]. Panel (c) shows the definition of several angles.*

It is clear that for plateau harmonics, the angle scans generally follow the structure of the HOMO. A very pronounced peak shows up around 30 eV, corresponding to the shape resonance in the PICS. For harmonics after about 50 eV, the angle scans no longer follow the structure of the HOMO. Specifically, dips start to show up at zero degree, which is a

direct expression of the Cooper minimum in the PICS. Note that, this is not coming from HOMO–1 as we do not observe any peaks at 90 degrees [120]. A QRS calculation with the alignment distribution is plotted in panel (b) of Fig. 5.11 to compare both features to experiment; the two show good agreement. This is the first time that both features can be directly seen in the HHG experiment, which is a result of the high degree of alignment in our experiment.

There are a few angles that need to be clarified. We use angle α as the angle between the pump and probe polarizations. For a certain degree of alignment, molecules will have a distribution inside the cone around the pump polarization, and we use angles θ and ϕ (ϕ not shown) as the polar and azimuthal angles of the alignment distribution with respect to the pump polarization. θ' and ϕ' represent the polar and azimuthal angles of a single molecule with respect to probe polarization. QRS suggests that at angle α, the induced dipole moment can be modified from Eq. 5.2 and written as [111]

$$D(\omega,\alpha) = \int_0^{2\pi}\int_0^{\pi} \rho(\theta',\phi')\sqrt{N(\theta')}W(\omega)d(\omega,\theta')\sin\theta' d\theta' d\phi', \tag{5.6}$$

where θ' and ϕ' are functions of (θ,ϕ,α) and $\rho(\theta',\phi')$ is the alignment angular distribution about the probe polarization. Since harmonics are emitted in both directions parallel and perpendicular to the driving field [134], we can calculate the molecular frame induce dipole $D(\omega,\theta') = \sqrt{D_{\parallel}^2(\omega,\theta') + \cos^2\phi' D_{\perp}^2(\omega,\theta')}$. In our case, the alignment distribution is so narrow that we can treat $\phi' \approx 0$, therefore, there is no ϕ dependence and we can write the MF dipole as an expansion of $\sum_j b_j D_{00}^j(\theta')$, where b_j are the coefficients of different orders of Wigner D-functions D_{00}^j.

We get the alignment angular distribution $\rho(\theta,\phi)$ at the alignment peak—the same peak that is used for experimental angle scans—using the same laser parameters that we get from fitting the delay scans. In order to get $\rho(\theta',\phi')$, we rotate $\rho(\theta,\phi)$ using a rotational matrix $R(\alpha)$. The rotation is done on each $|lm\rangle$ state

$$R(\alpha)\,|lm\rangle = \sum_{m'} D^{l}_{m'm}(\alpha)\,|lm'\rangle, \tag{5.7}$$

where $D^{l}_{m'm}$ are the Wigner D-functions. The alignment angular distribution $\rho(\theta,\phi)$ can be expressed as

$$\rho(\theta,\phi) = C^{*}_{l'm'} C_{lm}\,\langle l'm'|lm\rangle\,, \tag{5.8}$$

where C_{lm} are coefficients of each $|lm\rangle$ state. Expectation values of $\left\langle D^{j}_{00}(\theta')\right\rangle$ are then calculated in the (θ',ϕ') coordinates and those are fitted to the measured angle scans at each photon energy. The fitted angle scans are plotted in panel (c) of Fig. 5.11, it is almost identical to the measured one (panel (a) of Fig. 5.11), the coefficients obtained from the fittings are listed in App. C.

Note that, we also use real coefficients b_j as we did for delay scan fittings. In this case, since the degree of alignment is so high, we make the approximation that within the alignment distribution, dipole phase from each molecule changes slowly [124], therefore, we assume again an angle independent phase for fitting.

In both delay and angle fittings, we fit to delay and angle scans that are normalized to the isotropic spectrum, therefore, the returning electron wave packet $W(\omega)$ can be canceled out. By further deconvolving the alignment distribution, the extracted signal S_{Ext} can be expressed as

$$S_{\mathrm{Ext}}(\omega,\theta') = \frac{N(\theta')d^{2}(\omega,\theta')}{A(\omega)}, \tag{5.9}$$

where $A(\omega)$ is an energy dependent factor from normalizing to the isotropic harmonic spectrum. The extracted harmonic yield $S_{\mathrm{Ext}}(\omega,\theta')$ are plotted in Fig. 5.11 from both fitting methods. In order to extract the PICS $d^{2}(\omega,\theta')$, we need to factor out the angle dependent tunneling ionization rate $N(\theta')$, however, because we have an energy dependent constant, $A(\omega)$, we can only determine PICS for each harmonic order separately.

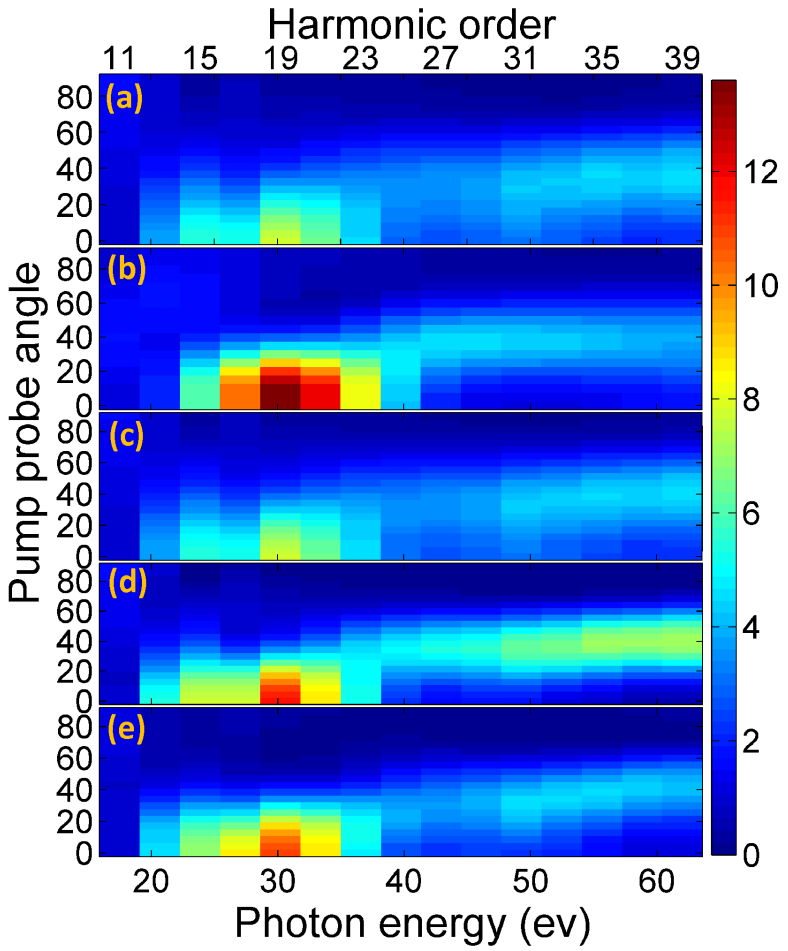

Figure 5.11: *Panel (a): Measured angle and energy dependent harmonic yield (2D projection of panel (a) from Fig. 5.10). Panel (b): QRS calculation using the alignment distribution getting from fitting delay scans. Panel (c): Fitted angle scans for each harmonic order. Panel (d): Extracted molecular frame harmonic yield from fitting angle scans. Panel (e): Extracted molecular frame harmonic yield from fitting delay scans. Only data between 0 and 90 degrees are shown for all the figures.*

The experiment for measuring the angle dependent tunneling ionization rate is performed using the same setup as in Fig. 5.3, except that all the beams are now focused into the VMI spectrometer. Probe focusing conditions are kept as close as possible to the conditions in the HHG experiment. Meanwhile pumps fluence are reduced a little bit in order to provide similar degree of alignment in the VMI interaction region where the molecular rotational temperature is expected to be lower. To ensure that the process is in the tunneling regime, we

examine the Keldysh parameter [135]—$\gamma = \sqrt{\frac{I_p}{2U_p}}$—for our system. With a probe (centered at 800 nm) intensity of 200 TW/cm^2, for N_2, whose ionization potential is 15.6 eV, γ equals 0.8. The criteria for justifying if a process is in the tunneling regime is by comparing γ to one, with $\gamma \ll 1$ and $\gg 1$ corresponding to tunneling ionization and multi-photon ionization, respectively. We follow the literatures [35, 136, 137] and treat the value of 0.8 as in the tunneling regime.

The tunneling ionization rate of N_2 is measured by operating the VMI in the time of flight (TOF) mode, in which ion fragments with different mass to charge ratio will hit the MCP detector at different time. A voltage gate is then applied on the MCP detector with the trigger and gate time set so that only signal from N_2^+ is recorded by a boxcar integrator. The integrated ion yield of N_2^+ at each pump-probe delay is recorded to extract the angle dependent tunneling ionization rate.

In order to reduce the noise in the measurement and to normalize the ionization rate to its isotropic value, an optical chopper is introduced in the pump arm. Similar to scenario in the pump-DFWM measurement discussed in Chap. 4, we also have four different kinds of signals for every four laser shots. These are: (a) Jet and background gas N_2^+ signal from both the pump and probe pulses, referred to as A. (b) Background gas N_2^+ signal from both the pump and probe pulses, referred to as B. (c) Jet and background gas N_2^+ signal from just the probe pulse, referred to as C. (d) Background gas N_2^+ signal from just the probe pulse, referred to as D. By factoring out the background and normalizing the signal to the isotropic, we can get the normalized ion yield trace as a function of the pump probe delay–$S_{\text{ion}} = \frac{A-B}{C-D}$. Such measurements are shown in Fig. 5.12, with alignment from pump 1, pump 2 and both pumps are recorded separately.

To extract the angle dependent tunneling ionization rate, we follow the procedures as discussed previously and fit the measured delay scans to an expansion of Wigner D-functions with $m = 0$. Different from the HHG case, for ionization, we do not need to worry about the phase, and the ionization yield can be written as [119]:

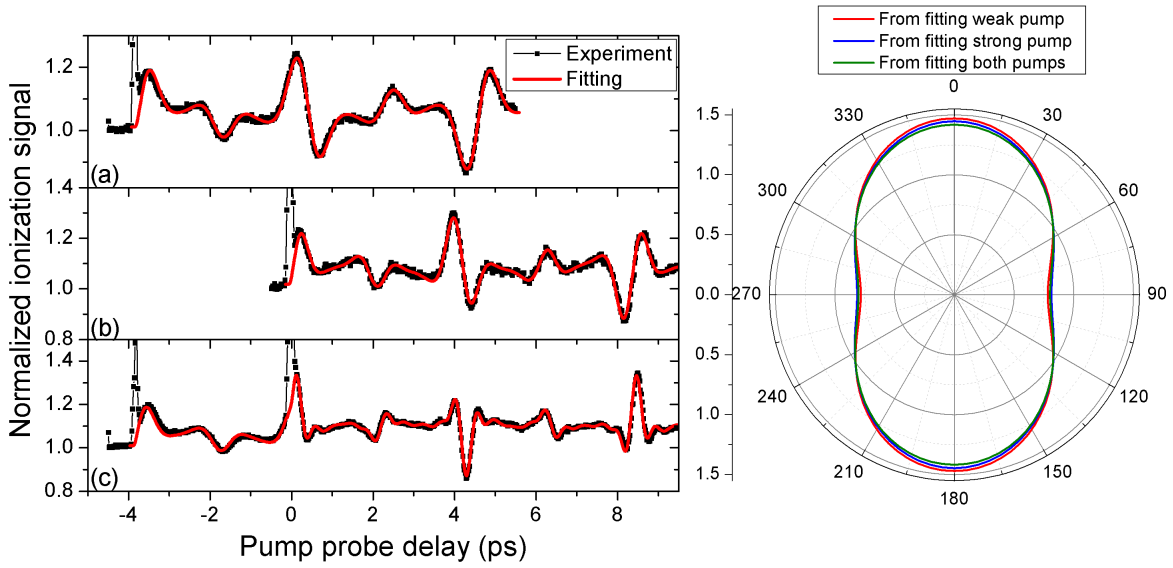

Figure 5.12: *Left panel: measured delay scans and fittings for the (a) pump 1 (b) pump 2 (c) both pumps. Right panel: Extracted Molecular Frame tunneling ionization rates from those fittings.*

$$S_{\text{ion}}(t) = \sum_j a_j \left\langle D_{00}^j \right\rangle (t), \tag{5.10}$$

where a_j are real coefficients with $j = 0, 2, 4, 6, 8....$ During the fitting, the Levenberg-Marquardt algorithm searches for the optimum combination of $(T, \tau_1, I_1, \tau_2, I_2, t_{\text{sep}})$ to give the minimum least squares between experiment and calculation, where τ_1, I_1, τ_2, I_2 correspond to pulse durations and intensities of pump 1 and pump 2, t_{sep} is the time separation between the two. As shown in Fig. 5.12, all revival scans are less structured compared to the HHG delay scans (Fig. 5.9), therefore, higher orders of $\left\langle D_{00}^j \right\rangle$ are not necessary for this fitting. This is examined by checking the error bars on the retrieved coefficients within certain confidence level. For example, in the two pumps case, where the degree of alignment is estimated to be about 0.86 for $\langle \cos^2 \theta \rangle$ at the full revival peak after the second pump—if we fit up to $\left\langle D_{00}^6 \right\rangle (t)$, the coefficients turn out to be $a_0 = 1.0093 \pm 0.0012, a_2 = 0.4119 \pm 0.0056, a_4 = 0.0038 \pm 0.0113, a_6 = 0.0007 \pm 0.0141$ with a 80% confidence level. The confidence intervals for a_4 and a_6 are consistent with zero values for these coefficients.

Different pumps	T	τ_1	I_1	τ_2	I_2	t_{sep}	a_0	a_2	a_4	$\langle\cos^2\theta\rangle$
Weak pump	10	50	40	/	/	/	1.0111±0.0008	0.4589±0.0028	0.0003±0.0099	0.65
Strong pump	10	/	/	50	60	/	1.0176±0.0011	0.4159±0.0046	0.0121±0.0105	0.75
Both pumps	10	60	40	60	64	3.84	1.0093±0.0012	0.412±0.0055	-0.0035±0.009	0.86

Table 5.1: *List of retrieved rotational temperatures, laser parameters and coefficients of* D^0_{00}, D^2_{00} *and* D^4_{00} *for three different aligning pump pulses.* T *is in units of Kelvin,* τ *and* I *are in units of* fs *and* TW/cm^2 *respectively and* t_{sep} *is in units of* ps.

Moreover, the presence of the $\langle D^6_{00}\rangle(t)$ term also does not effect the retrieved angular distribution very much since the overall contribution is negligibly small. Therefore, we decide to fit only up to the $\langle D^4_{00}\rangle(t)$ term. The fitted delay scans for all three cases are shown in Fig. 5.12 and the retrieved laser parameters and coefficients are shown in table 5.1 along with the best degree of alignment in each case.

We can see that the extracted laser parameters in the case of both pumps deviate somewhat from those extracted with each pump alone, which may be due to small changes in the experimental conditions, such as laser power fluctuating or a drift of the spatial overlap of the pump and probe. But the overall agreement between the experimental delay scans and the calculated ones is quite good. The angle dependent MF tunneling ionization rate $S(\theta)$ can then be obtained by replacing D^j_{00} coefficients with the corresponding Legendre polynomials $P_j(\cos\theta)$. In this case, $S(\theta) = a_0P_0(\cos\theta) + a_2P_2(\cos\theta) + a_4P_4(\cos\theta)$. Those are also shown in Fig. 5.12. $S(\theta)$ from all three cases look almost identical, which proves that our extraction is consistent and reliable.

Thus, this angle dependent ionization rate is then used for extracting the angle dependent PICS from the HHG measurements. The result from fitting harmonic angle scans is shown in the middle panel of Fig. 5.13. We compare it with the calculated PICS, which is similar to the one in Fig. 5.2, except that now both parallel and perpendicular components are included. Very good overall agreement is seen between the two. We also plot the extracted PICS from fitting harmonic delay scans. Surprisingly, even though the angle independent phase approximation is not quite applicable in this case, the agreement with calculation is still quite good. Again, the possible explanation is that in delay scans, the dominant

contribution for each harmonic still comes from a narrow range of angles.

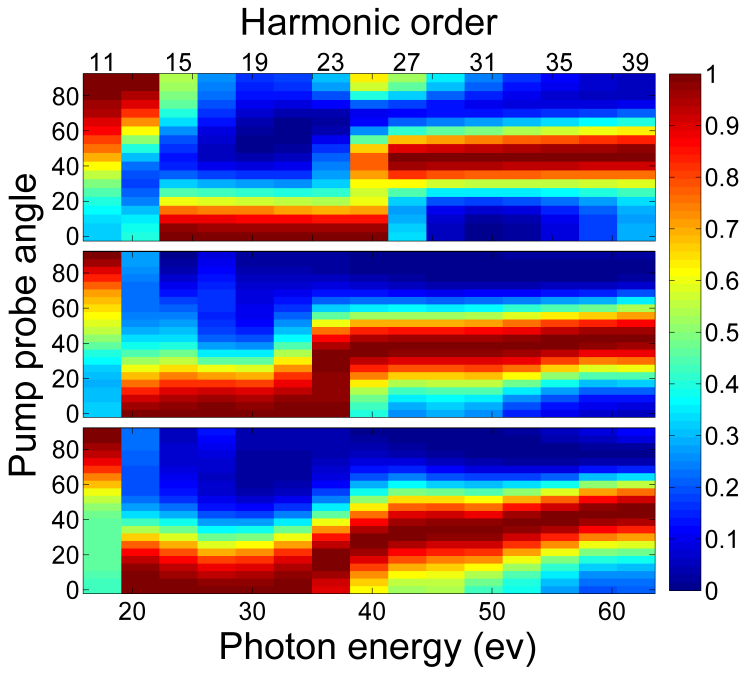

Figure 5.13: *Top panel: Theoretical molecular-frame PICS of the HOMO (The PICS which are responsible for both parallel and perpendicular components of HHG are included). Middle and bottom panels: PICS retrieved from the experimental angle and delay scans, respectively. All results are normalized to peak value for each harmonic order individually.*

Even though the extracted ionization rate gives a PICS that is very similar to the one theory predicts, we still want to comment more how reliable the extract ionization rate is. Different from tunneling ionization rate from atoms, which have been well studied and found to be in good agreement with existing tunneling ionization theories [138, 139], such as the strong field approximation (SFA) [140] and the Ammosov-Delone-Krainov (ADK) [138] theory, the study of tunneling ionization from molecules have been struggled a lot for the past decade. To date, many measurements still show significant deviation from existing molecular tunneling theories, such as molecular-SFA (MO-SFA) [113, 114] and molecular-ADK (MO-ADK) theory [141]. For example, in the case of aligned molecules, the molecular frame angle dependent tunneling ionization from aligned CO_2 was extracted from experiment [35]

and showed very sharp peak at 45 degrees with respect to the molecular axis, which can not be reproduced by current tunnel ionization theories. Similar experiments were performed on aligned carbonyl sulphide molecules [137], in which an ionization peak was observed at 0 degree while MO-ADK predicted a dip. Moreover, the ratios of the ionization rate along molecular axis versus its perpendicular axis that has also been reported are very different and show strong departure from the theory. For instance, for the N_2 molecule, a ratio of 3.3 was reported by Pavičić *et al.* [35] while 4.5 was reported by Litvinyuk *et al.* [136], however, SFA predicts 5 and MO-ADK predicts 10. In our case, the ratio is even lower—about 1.8. One possible reason might be the participation of lower orbitals, such as HOMO–1, which will peak at 90 degrees with respect to the molecular axis, thus reduce the ratio. Another possibility is that we may be underestimating the intensity of the ionizing pulse; the ratio is expected to decrease with increasing intensity [35, 137]. While both experiment and theory in this field need further improvement in order to solve this problem, our extracted angle dependent ionization rate serves as part of debates.

In conclusion, we show that HHG can be utilized as a viable tool for photoionization measurements if the molecules are well aligned. A high degree of alignment is essential to extract narrow angular features. In particular, such inversion can be done without any prior knowledge of the electronic structure of the molecular and thus has the potential to reveal new molecular frame features. Furthermore, the fact that delay scans can also be used to extract PICS suggests that this method can be extended to asymmetric tops, for which angle scan measurement about the angle χ (the angle that a molecule rotates about its own axis) is not accessible even if the molecules are 3D aligned. Yet, by fitting delay scans for different harmonic orders from such molecules, it should be possible to extract the fully differential PICS with dependence on both angle θ and χ. Such experiments and analysis are in progress.

Chapter 6

Alignment-assisted orientation of molecules

6.1 Introduction to molecular orientation

Different from molecular alignment, where the head and tail of heteronuclear molecules are not distinguished, molecular orientation further confines this freedom. This is useful in the sense that for heteronuclear molecules, any measured information on the aligned samples will be averaged over the two opposite orientations, a real molecular frame measurement can not be achieved without orienting the molecules.

It is generally accepted that producing molecular orientation is much more challenging than producing molecular alignment. The conventional ways of inducing molecular orientation are to use hexapole focusing [21, 142, 143] or brute force [22, 144] methods. Briefly a hexapole works as a state selector. Due to the first order stark effect when the field from the hexapole interacts with the molecule, any rotational states with quantum number $M < 0$ (linear molecule) or $K \times M < 0$ (symmetric top) will be pulled into the center and focused some distance away. A single $|JKM\rangle$ state can then be selected and oriented by adding another DC electric field. This method is able to generate the strongest possible degree of orientation compared to other methods. However, it only works for linear and symmetric tops and not for asymmetric tops. Furthermore, the complicated experimental design and the extremely low gas density that remains limit the practical application of this method.

Brute force orientation is simple experimentally. Two charged plates with very high DC electric field will orient polar molecules via the permanent dipole interaction. However, the degree of orientation that can be achieved is rather poor and the required DC field is extremely high.

Laser induced molecular orientation was first developed by combining an adiabatic non-resonant laser field with a moderately strong electrostatic field. Molecules can be aligned by the laser pulse and then oriented by the electrostatic field through interaction with the molecule's permanent dipole moment [23, 145]. Experimentally, both linear [146] and asymmetric top [147] molecules have been oriented using this method and the degree of orientation can be enhanced by increasing the laser intensity or static field strength, or by lowering molecules' rotational temperature. Even though this method gives strong orientation, it fails to produce orientation under field free conditions which will affect many further experiments. A small change to this scheme is able to provide field free orientation. For example, the combination of an electrostatic field with a slow-turn-on and rapid-turn-off laser pulse [148], or with an intense ultrashort non-resonant laser field [149]. However, the electrostatic field is still always present, which may affect experiments involving low energy electrons and so on. Therefore, an all optical field free orientation technique is desired.

To serve this purpose, two techniques have been proposed. One uses few cycle terahertz pulses [24, 150, 151], the other uses dual color pulses [25, 152]. The fundamental idea in both cases is the same—producing an asymmetric driving field. The former uses few or single cycle terahertz pulses to reduce cycle averaging on the permanent dipole interaction. An experiment has been reported on orienting room temperature OCS molecules with few cycle THz pulses, which gives only weak orientation [151]. No experiments have been performed on rotationally cooled molecules yet. The dual pulse technique consists of a phase synchronized fundamental and its second harmonic field. Two scenarios are involved when the field interacts with the molecules—when the field intensity is high, it selectively ionizes molecules with their axes pointing along one direction versus the other, therefore, it depletes one

orientation and leaves an oriented ensemble [28, 153]. However, because of the strong two-color field, molecules are very likely to be excited to higher vibrational or electronic states which will complicate the interpretation of further experiments. On the other hand, when the two-color field intensity is relatively low, it interacts with the molecular hyper-polarizability tensor and causes molecules to orient. Due to the fact that molecules with high ionization potentials normally have weak hyper-polarizabilities, the orientation degree in this case tends to be low [153]. Since the first experimental demonstration of this technique [26], many groups proposed various methods of trying to increase the orientation such as using two time separated two-color pulses [154], or a combination of time separated single and two-color pulses [155]. The former provides control of the rotational wavepacket and gives an increment of less than a factor of 2. The latter has been proved to be very effective on both low [156] and high [157] temperature molecules. An increment of more than a factor of 3 is simulated when the single-color field is appropriately delayed with respect to the two-color field.

In this chapter, I will describe the first experimental demonstration of this technique. An increment from $\langle\cos\theta\rangle$=0.055 to 0.13 is achieved from rotationally cooled CO molecules by adding the single-color field, where θ is the angle between the laser polarization axis and molecular axis.

6.2 Orienting molecules using two-color laser field

Before examining the case of combined single and two-color laser pulses, we orient gaseous CO molecules with just a two-color beam. For our laser with a center wavelength of about 800 nm, that is a combination of 800 nm and 400 nm pulses.

The electric field of such a two-color pulse can be expressed as $E(t) = \varepsilon_\omega(t)e^{i\omega t} + \varepsilon_{2\omega}(t)e^{i2\omega t+\varphi}$, where ε_ω and $\varepsilon_{2\omega}$ are amplitudes of the the fundamental (800 nm) and its second harmonic (400 nm), and φ is the relative phase between the two. When the field interacts with the molecule via its hyper-polarizability, the interaction Hamiltonian can be

written as

$$H = B\hat{J}^2 - \mu E(t)\cos\theta - \frac{1}{2}[(\alpha_\parallel - \alpha_\perp)\cos^2\theta + \alpha_\perp]E(t)^2 - \frac{1}{6}[(\beta_\parallel - 3\beta_\perp)\cos^3\theta + 3\beta_\perp\cos\theta]E(t)^3, \tag{6.1}$$

where B is the rotational constant of the molecule, $\hat{J}$ is the angular momentum operator, $\alpha_\parallel$ ($\beta_\parallel$) and $\alpha_\perp$ ($\beta_\perp$) are parallel and perpendicular components of the polarizability (hyper-polarizability). Under slowly varying envelope approximation, the Hamiltonian can be further cycle averaged over the electric field which gives,

$$\bar{H} = B\hat{J}^2 - \frac{1}{4}[(\alpha_\parallel - \alpha_\perp)\cos^2\theta + \alpha_\perp][\varepsilon_\omega^2(t) + \varepsilon_{2\omega}^2(t)] - \frac{1}{8}[(\beta_\parallel - 3\beta_\perp)\cos^3\theta + 3\beta_\perp\cos\theta]\varepsilon_\omega^2(t)\varepsilon_{2\omega}(t)\cos\varphi. \tag{6.2}$$

By solving the TDSE for a rigid rotor [1], we can get both alignment and orientation revival traces, which can be quantified by $\langle\cos^2\theta\rangle$ and $\langle\cos\theta\rangle$, respectively, as mentioned in the previous chapters.

The experimental setup is shown in Fig. 6.1. We split the output from KLS into pump and probe arms using a broadband 80/20 beam spliter, 20% goes to probe arm and focuses into the VMI spectrometer using a 25 cm focusing mirror. 80% goes to the pump arm in which a telescope is used to shrink the pump beam size by a factor of 2 in order to increase the efficiency of second harmonic generation as well as reducing the pump intensity at the focus so that it does not ionize the molecule, this is confirmed by examining the time of flight spectrum of the pump in which no ion fragments are observed. The pump beam is split again by a 70/30 beam spliter. 70% goes through a 200 μm BBO crystal to generate the second harmonic. Three 600 μm calcite plates and a pair of wedges are used to overlap the fundamental and the second harmonic. One of the calcite plates is mounted on an automatic rotational stage to control the relative phase φ. The two-color beam then recombines with

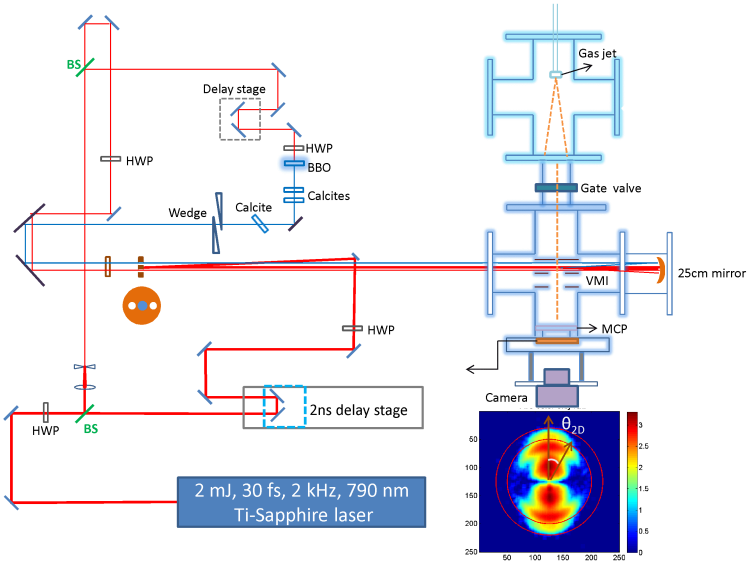

Figure 6.1: *Experimental setup for orienting CO molecules using two-color laser pulse. The inset shows how a typical momentum distribution for C^{2+} and the region in between the two red circles is the channel we gate on. θ_{2D} is also marked.*

the single-color beam and the probe beam non-colinearly and all are focused together by the same focusing mirror. Our target CO molecules are produced by the 1 kHz supersonic Even-Lavie valve with a 500 psi mixture of 20% CO and 80% helium as the backing gas, which will be shown to cool the rotational temperature of CO down to 3 K. In the interaction region, which is about 50 cm away from the jet, the pumps align and orient the CO molecules, the probe Coulomb explodes the molecules and the momentum distribution of the fragments are recorded shot by shot by a microchannel plate, a fast phosphor screen and a 1 kHz CMOS camera at every pump-probe delay. In this section, we will investigate orientation from just the two-color beam, the single-color beam—referred to as the infrared (IR) beam—will be blocked.

In order to synchronize blue (second harmonic) and red (IR), the asymmetry of the electron spectrum of CO is measured [158]. When blue and red are overlapped, the total electric field becomes asymmetric. Depending on the relative phase between the two, the electric field will be stronger in the positive Z direction ($\varphi = 0$) or the negative Z direction

($\varphi = \pi$), therefore, the electron spectrum will be up-down asymmetric when the two-color pulse is polarized parallel to the detector plane. The asymmetry parameter γ can be calculated using $(N_{\text{up}} - N_{\text{down}})/(N_{\text{up}} + N_{\text{down}})$, where N_{up} and N_{down} are the number of electrons above and below the center of the electron distribution. The overlap of the blue and red is found by rotating the calcite in the rotational mount. By changing the angle of the calcite, the optical path length will change therefore, blue and red will have different phase shifts. By recording γ for each angle position, the maximum and minimum γ can be found which correspond to $\varphi = 0$ and $\varphi = \pi$.

For both phases we record momentum distribution images from the C^{2+} fragment at each pump-probe delay. $\langle \cos\theta_{2D} \rangle$ and $\langle \cos^2\theta_{2D} \rangle$ traces are then measured by gating on the channel with the highest kinetic energy, as marked by the region in between the two circles in the inset of Fig. 6.1. Again, θ_{2D} is the angle between the probe polarization direction and the vector of individual ion hit on the 2D image with respect to the image center. The traces are shown in scatter plots in Fig. 6.2.

An orientation level of $\langle \cos\theta_{2D} \rangle \approx 0.08$ is achieved at about 3.8 ps near half of the rotational period. There are two important features that need to be clarified in this data set. First, the peak of the orientation near the full revival (~8.2 ps) is a little bit before the peak of the anti-alignment (~8.4 ps). This indicates that the orientation is coming from the hyper-polarizability interaction rather than ionization depletion [153]. In the case of ionization depletion, the peak of orientation should match with the peak of the alignment. Second, we see both alignment at quarter revivals and orientation at half revivals. Both levels are actually comparable to the ones at the full revival, which is not the case in S. De's report [26], where no alignment is seen at quarter revivals and no orientation at half revivals. The explanation is that in their case, the rotational temperature of CO is estimated to be about 60 K and at this temperature the populations in the even and odd J states are equal. $\langle \cos^2\theta \rangle$ and $\langle \cos\theta \rangle$ values from even and odd initial J states have a π phase difference at quarter and half revivals correspondingly, resulting in a cancelation of the alignment and

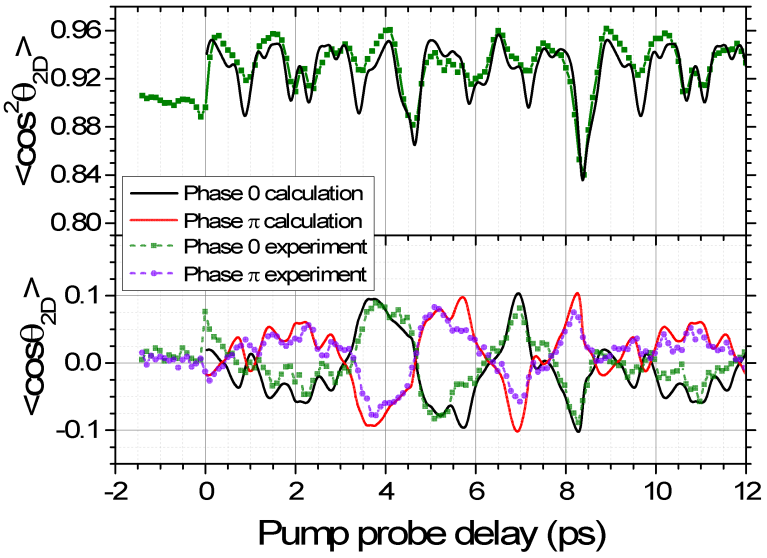

Figure 6.2: *Experimental measurements and calculations of* $\langle \cos\theta_{2D} \rangle$ *and* $\langle \cos^2\theta_{2D} \rangle$ *with just the two-color pulse. The experimental momentum distribution images at each delay have been background subtracted and gaussian smoothed. For the calculations, 2D projection of the calculated 3D angular distribution are convolved with the measured probe selectivity. The pump pulses duration are about 70 fs for both IR and blue, the total intensity is estimated to be around 52 TW/cm*^{2} *with a blue to IR intensity ratio of 2.*

orientation. However, if the temperature is very low, the initial population of J states is significantly smaller, and populations in even and odd J states will not match, resulting in the occurrence of alignment at quarter revivals and orientation at half revivals (see Fig. 6.5). Furthermore, calculations show that only when the rotational temperature is below 5 K, half revivals give comparable orientation to full revivals. In our case, we estimate a rotational temperature of 3 K to get the best agreement between calculation and experiment.

In order to compare experiment with calculation, two factors are taken into account. First, in the experiment, we measure $\langle \cos\theta_{2D} \rangle$ while theoretically we calculate $\langle \cos\theta \rangle$ from a 3D distribution. To calculate the 2D value, we solve the TDSE to get the angular probability distribution ρ as a function of Euler angles θ and ϕ at each time delay. Note that there is no ϕ dependence because the interaction with the driving field is cylindrically symmetric. The 2D projections of these 3D distributions — ρ_{2D} — are then calculated to give the corresponding

$\langle \cos\theta_{2D} \rangle$ values. The axial recoil approximation is assumed in order to compare with the measurement. Second, pump and probe are both polarized parallel to the detector plane. Even without the pump beam, because the probe beam preferentially dissociates molecules that are pointing along its polarization direction, we measure a $\langle \cos^2\theta_{2D} \rangle$ value much higher than the isotropic value, which is 0.5. To take this probe selectivity into account, we measure a probe only image with high statistics and invert it using an iterative procedure [53]. The same kinetic energy channel is then gated on the inverted image to calculate the probe selectivity S as a function of angle θ for that particular channel. This selectivity is then convolved with the calculated 3D angular distribution and the final $\langle \cos^n\theta_{2D} \rangle$ (n=1,2) values are then calculated on the 2D projections using the following equation,

$$\langle \cos^n\theta_{2D} \rangle = \int_0^{2\pi} \int_0^{\pi} \left[\frac{2\cos\theta}{\sqrt{\cos^2\theta + \sin^2\theta\cos^2\phi}} \right]^n \rho(\theta,\phi) \cdot S(\theta) \sin^2\theta d\theta d\phi. \qquad (6.3)$$

The calculated traces are plotted using solid lines in Fig. 6.2 for both $\varphi = 0$ and π. The structures of both alignment and orientation traces show good agreement between calculation and measurement, except for a peak around 5.7 ps that shows up in calculation but not in experiment.

6.3 Enhanced molecular orientation using a combination of IR and two color-laser field

The next step is to position the IR pump before the two-color pump. The optimum separation between the two pumps has been estimated as around 1/4 or 3/4 of the rotational period [156, 157]. However, this number is very sensitive to rotational temperature and laser parameters. Especially for a kick at the 1/4 revival, the optimum separation varies from 1/5 of the rotational period at 3 K to 1/4 at 30 K. However, for a kick at the 3/4 revival, the optimal timing does not change much with temperature and covers a broader range (see Fig. 6.6). Therefore, experimentally, we choose a separation of about 6.4 ps. Alignment and orientation traces are recorded and shown in scatter plots of Fig. 6.3 for both $\varphi = 0$

and π along with the calculation of both $\langle\cos^2\theta_{2D}\rangle$ and $\langle\cos\theta_{2D}\rangle$ with probe selectivity. A measured orientation level of $\langle\cos\theta_{2D}\rangle \approx 0.25$ is achieved at 11.1 ps with respect to the IR pump. The overall agreement is good except for features near 9.5 ps, 13.2 ps and 17.1 ps that show up in the calculated $\langle\cos\theta_{2D}\rangle$ but not in the experiment.

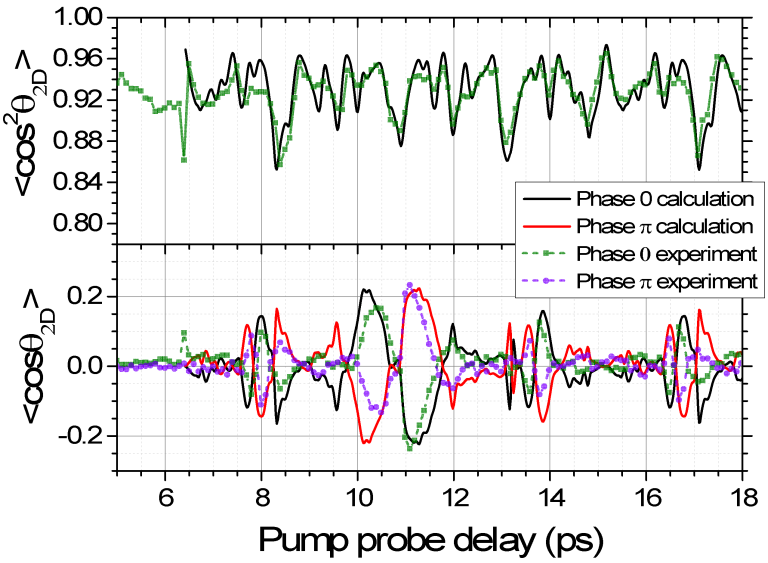

Figure 6.3: $\langle\cos\theta_{2D}\rangle$ *and* $\langle\cos^2\theta_{2D}\rangle$ *with both IR and the two-color pulses. The same image processing is performed as the two-color only case. Two-color pulse parameters are the same, the IR pulse is 85 fs and 40 TW/cm*^{2}.

The momentum distribution images at the peak orientation with no pumps, the two-color pump only and both pumps are also acquired with high statistics and inverted; center slices are shown in Fig. 6.4. A substantial increment of asymmetry can be seen from the images, indicating an enhancement of the orientation. The measured $\langle\cos\theta\rangle$ values from those images are 0, 0.064 and 0.194 correspondingly. Compared to the previous experimentally measured value [26], of about 0.06 obtained from an inverted image, we measure a much higher orientation level. The calculated angular distributions at these three moments are also plotted in Fig. 6.4, this increment in orientation as well as in alignment can clearly be seen.

The $\langle\cos^2\theta\rangle$ and $\langle\cos\theta\rangle$ traces without probe selectivity are plotted in Fig. 6.5 for our

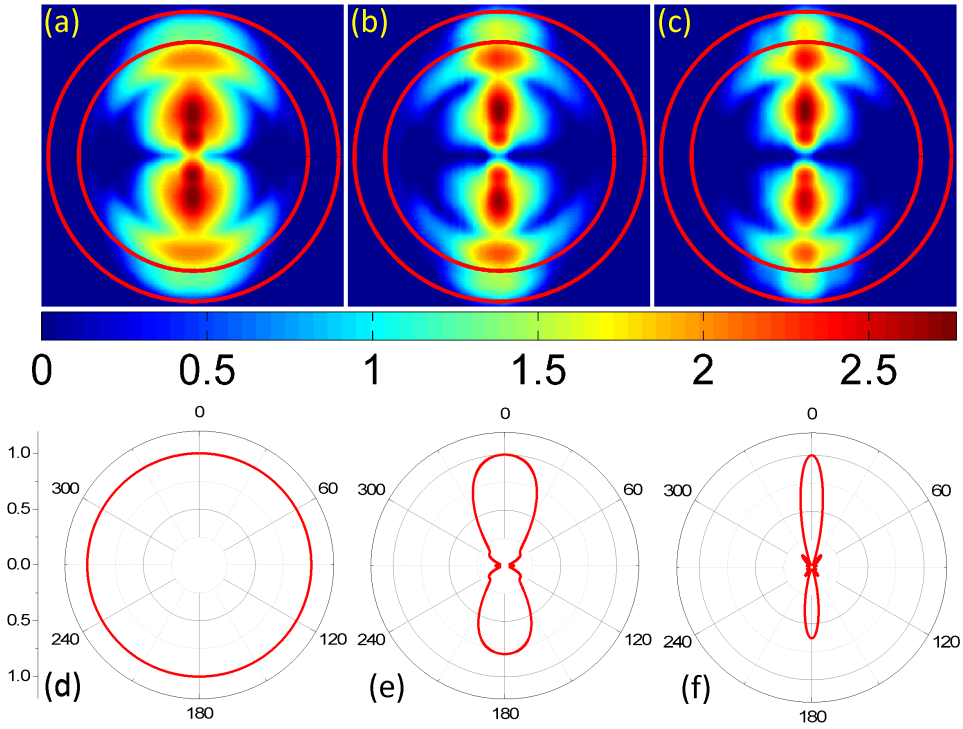

Figure 6.4: *Up panel shows the momentum distribution with (a) no orientation, (b) peak orientation with the two-color only pump and (c) peak orientation with both pumps respectively. Images (d), (e) and (f) in the lower panel show the calculated angular distribution in the corresponding cases. All experimental images are inverted from background subtracted and smoothed raw images. Images are shown in logarithmic scale. All calculated angular distributions are normalized to their peak values.*

experimental conditions. According to the calculation, we have achieved an orientation level of about 0.055 for the two-color only and enhanced to 0.13 by adding the aligning pulse. Note that both 2D projection and probe selectivity will cause the measured orientation level to be much higher than the actual level. For the Abel inverted images, probe selectivity still plays a role, thus the measured orientation is still higher than the actual one.

In order to understand the mechanism of this technique, we also plot the calculated orientation traces for even and odd J states separately for both two-color only and with the extra aligning pulse. As shown in panel (b) of Fig. 6.5, with only the two-color beam, even and odd J states alone give strong orientation at the half revival ($\approx 4\ ps$) but they are out

of phase, resulting in weak orientation or even no orientation when the temperature is about 2 K higher. At the full revival, even though even and odd J states are in phase, they both give very weak orientation, therefore, the sum of the two is still weak. However, if one can manipulate even and odd J states so that the stronger orientation peaks match up in phase or even eliminate the orientation from one parity of states, it will result in much stronger orientation. This was proved to be feasible by Kevin F. Lee *et al.* [159], who showed that the rotational wave packets in gas-phase molecules can be controlled by modifying the phase of the wave packet components using a laser pulse that kicks at a fractional revival. Therefore, the extra IR pulse is introduced in our setup, which initiates a rotational wave packet. The following two-color pulse modulates the rotational wave packet from even and odd J states differently, allowing control of the time when orientation appears and its strength. At the optimum separation, as shown in panel (d) of Fig. 6.5, the orientation from even J states gets enhanced, while the overall modulation in the orientation from odd J states becomes much smaller, therefore, the resulting orientation trace follows the even J states and produces much stronger orientation at the half revival after a single two-color pulse.

We also calculated the population of rotational J states for each thermally populated initial state for a single IR pump, a two-color pump and both pumps for our experimental conditions as shown in Fig. 6.5. In the IR only plot, since there are only $\cos^2\theta$ terms in the interaction potential, the population of higher J states from each initial state follows the selection rule of $\Delta J = 0, \pm 2$, resulting in alignment. When the two-color only pulse interacts with the molecule, $\cos\theta$ and $\cos^3\theta$ terms allow extra transitions for $\Delta J = \pm 1, \pm 3$, which result in orientation. We can see that with just the two-color pulse, a few odd states are populated for the initial $J = 0$ state. An even smaller number of even states are populated for initial $J = 1$ state, which indicates that initial even states will give a better degree of orientation than the initial odd states which agrees with the $\langle\cos\theta\rangle$ traces in panel (b) of Fig. 6.5. When we use both pumps, odd states populated from the initial $J = 0$ state are greatly enhanced while even states populated from the initial $J = 1$ state are suppressed

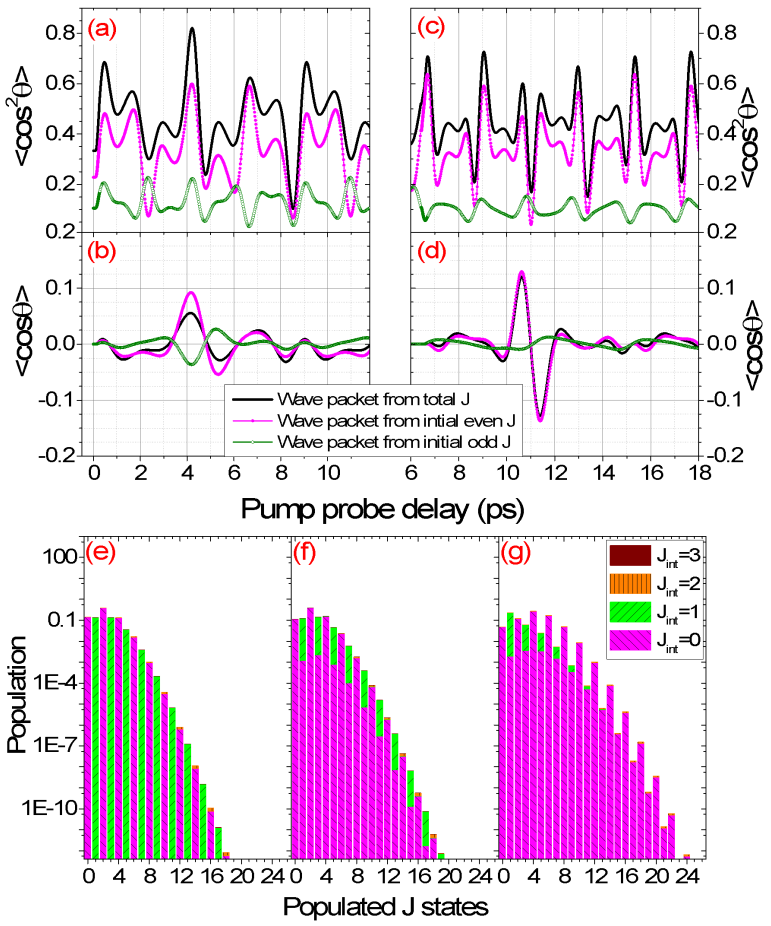

Figure 6.5: *Upper graph: Calculation of alignment and orientation traces for only the two color pump (Panel (a) and (b)) and both pumps (panel (c) and (d)). The time evolution of orientation from even and odd J states are also plotted separately. Lower graph: calculated population of rotational J states for each thermally populated initial state for the case of using just the IR pump (panel (e)), two-color only pump (panel (f)) and both pumps (panel (g)). The populations are in logarithmic scales.*

indicating that orientation from even initial states is enhanced while orientation from odd initial states is suppressed as seen in panel (d) of Fig. 6.5.

We further investigate the possibility of increasing the degree of orientation that we have achieved. The effect of blue to IR ratio, total two-color intensity, molecular rotational temperature and pumps separation are all explored and plotted in Fig. 6.6. The upper panel shows the calculated maximum $\langle \cos\theta \rangle$ values with different combinations of blue-IR ratio

and pumps separation. All the other parameters are the same as in the experiment. As we can see, we are clearly using too much blue in the experiment, reducing the ratio from 2 to 0.5 while keeping intensity constant will increase the orientation degree from 0.13 to about 0.16. The middle panel fixes all the other experimental conditions except for the total two-color intensity and the pumps separation. A blue-IR ratio of 0.5 is used. We can see that, as we increase the total two-color intensity, the orientation increases up to above 0.25 at the highest intensity of 70 TW/cm^2. Furthermore, if we can stretch the pulse duration and increase the energy in the two-color beam while still maintaining negligible levels of ionization, the orientation level can be made even higher [156]. However, practically, it is not trivial to stretch the pulse durations while still maintaining a reasonable blue to IR ratio in the two-color beam. The good orientation degree we get is also a result of the extremely low rotational temperature of our jet. In most cases, this is very hard to achieve. For example, for experiments like high harmonic generation from oriented molecules [28], which require a much higher gas density, measurements are normally performed right in front of the jet, where the molecules are not fully cooled down. The rotational temperature in this case is closer to 30 K as shown in the DFWM experiment [42]. To test the effectiveness of this technique at this temperature, a similar calculation is also shown in the bottom panel of Fig. 6.6, which shows that a reasonable degree of orientation is also achievable at slightly higher temperatures.

In conclusion, we successfully demonstrate the alignment-assisted field free orientation technique in experiment for the first time. By using rotationally cold CO molecules, an increment of orientation by more than a factor of two compared to a single two-color pulse is achieved. The effectiveness of this technique depends strongly on the molecular rotational temperature, pump laser parameters and pumps separation. Without knowing all these parameters, especially the temperature, experimentally a searching and optimizing algorithm is well suited for finding the optimum combination to give the best orientation. To perform such an experiment, the pump separation can be set near the 1/4 or 3/4 revivals, and the

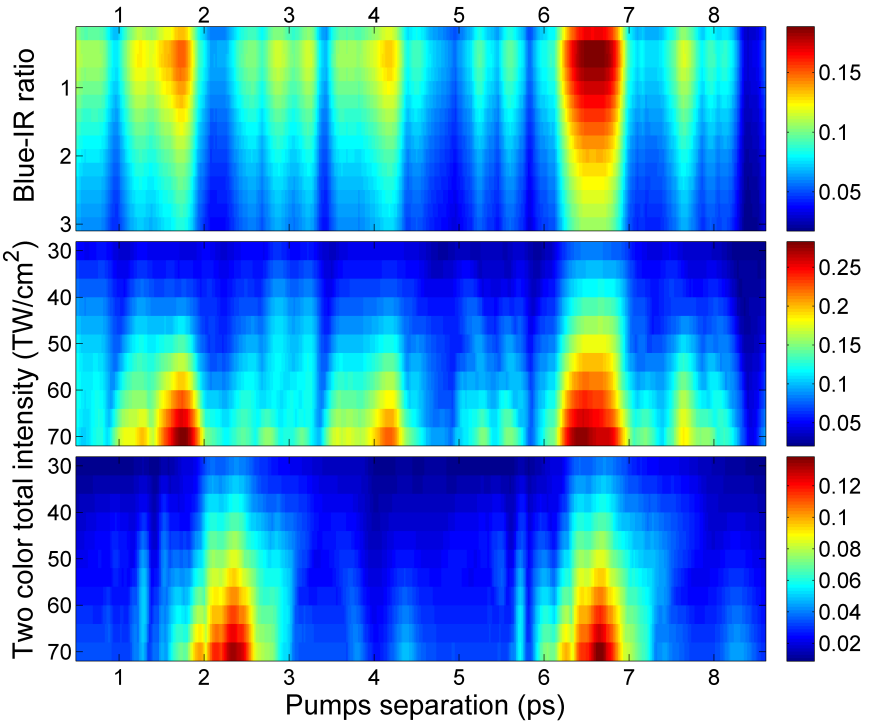

Figure 6.6: *Top panel: Calculated maximum* $\langle \cos\theta \rangle$ *for pump separations from 0.5 ps to 8.6 ps and blue-IR ratio from 0.2 to 3 with a step size of 0.2 at 3 K and a fixed intensity. Middle panel: Calculated maximum* $\langle \cos\theta \rangle$ *with a blue-IR ratio of 0.5 at 3 K. The two-color intensity is varied from 30 TW/cm*^{2} *to 70 TW/cm*^{2} *with a step size of 4 TW/cm*^{2} *and the pump seperation is vaired as in the top panel. Bottom panel: the same calculation as the middle panel except for a rotational temperature of 30 K.*

two-color pulse can be shaped. Due to the fact that SHG outputs blue pulses polarized perpendicular to the input, both S and P polarization shaping will be required. For example, one can generate two independently controlled orthogonally polarized pulses from the shaper and use them for SHG. After carefully filtering out one polarization after SHG, time overlapped IR and blue pulses with the same polarization can be obtained with the phase and intensity ratio of the two can be controlled to great precision by the shaper. However, the amount of laser power that can be obtained after the shaper without damaging the spatial light modulator can limit the orientation degree that can be achieved.

Chapter 7

Summary

In this thesis, I described some of our successful and complete experiments and computations, those are listed as following:

First, a single metric for characterizing 3DA is proposed by Makhija *et al.* [Phys. Rev. A **85**,033425 (2012)]. This is important for identifying when 3DA is induced in molecules, especially in the theory. This is also useful for future exploration of 3DA optimization. Based on this quantity, our scheme for improving FF3DA is stimulated, explored and demonstrated experimentally. A VMI, implemented single shot at 1 kHz, is used for measuring the best FF3DA achieved so far using our multi-pulse scheme. This is a big step forward because with enough pulse energy, FF3DA degree close to that of adiabatic 3DA degree can be achieved for future experiments.

Second, a pure optical method to measure alignment is developed independent of the axial recoil approximation as is required for VMI measurements. The third order nonlinear effect provides a strong background free signal, makes it useful to measure alignment from low density complex asymmetric tops without damaging the molecules. The theory is developed to reproduce the measured alignment trace. This method is also fast, making it suitable for feedback optimization experiments. It is sensitive to rotations about all molecular axis, indicating its potential for measuring 3DA. 1DA from iodobenzene molecules is successfully measured and shows K-type revivals that have not been previously measured from an aligned rotational wavepacket.

Third, high order harmonic generation experiments have been performed on nitrogen molecules with the highest degree of alignment so far. Many features are observed directly for the first time from nitrogen molecules, including high order fractional revivals, drastic changes in revival structures as a function of harmonic order, a shape resonance and cooper minimum in the PICS of the nitrogen HOMO. By deconvolving the alignment distribution, angle dependent PICS from the HOMO orbital can be extracted.

Fourth, the scheme for increasing field-free molecular orientation is demonstrated experimentally for the first time. By using an aligning pulse before the orienting two-color pulse, almost a factor of three higher orientation is achieved for rotationally cold CO molecules. Good agreement between measurement and theory is achieved by calculating 2D alignment distribution and convolving it with the measured probe selectivity.

In the thesis, there are also works that raise questions or require further investigations, those are listed in the following paragraphs:

First, the proposed single measure for 3DA $\cos^2\delta$ is mostly useful for theoretical investigation. Can it be linked with experimental observables, or in another words, can we measure $\cos^2\delta$ in experiment directly? If we can find single or even multiple quantities proportional to $\cos^2\delta$, experimental optimization of 3DA will be more feasible.

Second, the laser pulse separations and the ellipticities of the pulse sequence used for our FF3DA experiment are mostly obtained by trial and error. Is there an optimal pulse sequence that will give the best FF3DA and can we actually solve the problem to get the optimal pulse sequence? These merit further theoretical investigation.

Third, for the optical experiment, what will the measured trace look like if a 3DA sample is introduced? Can it actually measure all A, K, J and C-type revivals? Can it be linked to $\cos^2\delta$ in some way? The optimization experiment with toluene successfully enhanced the C-type and suppressed the J-type revival, which means alignment is better, but how good is the alignment? Is the output pulse optimum? If an optimization is performed in theory, does it give the same kind of output pulse? These are not easy questions to answer, but

will be quite valuable if solved.

Fourth, in the harmonic generation experiment, we assumed that the harmonic phase to be flat for fitting both delay and angle scans. This assumption is reasonable for angle scans, but not very suitable for fitting delay scans. We know from theory that recombination phase from HOMO PICS are very structured, for example, it has phase jump at both the shape resonance and Cooper minimum. However a flat phase still gives about the correct amplitude after fitting. Does that mean in the process the phase accumulated in the propagation step dominates over the recombination phase? What will propagation in the gas medium do to the final harmonic phase? Can we actually retrieve the recombination phase from the measured harmonic intensities? A direct measurement of the phase might be able to answer those questions. This can be achieved using interference from two different gas targets[160] and interference from the same gas target but two different harmonic sources, one aligned and one not [32].

Fifth, in the tunneling ionization experiment, why is the probe effect so large in our case? Is there actually a HOMO–1 contribution? How will it differ if we measure electrons directly? Many questions can be asked in this experiment and agreement between experiment and theory is still very poor.

Based on those contributions to the strong field physics, exciting future projects can be conceptualized:

First, harmonic generation from asymmetric top molecules with good FF3DA. By combining our multi-pulse FF3DA technique with harmonic generation we can measure and track structure or dynamics in more complex molecules. The low ionization potential of most asymmetric tops will preclude the generation of a large spectrum of high order harmonics using a 800 nm laser pulse, thus requiring longer wavelength laser pulses.

Second, the imaging of a single molecule using the electron diffraction technique on a field-free 3D aligned sample. An experiment has already been demonstrated of imaging a single CF_3I molecule with 1DA [29]. The bond lengths and bond angles can be retrieved,

however, the position of three F atoms cannot be determined due to their spinning around the C-I axis. In the case of an asymmetric top molecule, using our technique, this kind of spinning can be ceased to allow full reconstruction of the molecular structure.

Third, harmonic generation from strongly oriented molecules. By using the alignment assisted orientation technique, with enough laser pulse energy, even at high temperature, good orientation can be achieved. Harmonic generation from such molecules will provide even order harmonics, give more energy resolutions, and more features in the molecular PICS may be obtained.

Bibliography

[1] H. Stapelfeldt and T. Seideman. Colloquium: Aligning molecules with strong laser pulses. *Reviews of Modern Physics*, 75(2):543–557, 2003.

[2] Jonathan G. Underwood, Benjamin J. Sussman, and Albert Stolow. Field-Free Three Dimensional Molecular Axis Alignment. *Physical Review Letters*, 94:143002, 2005.

[3] A. Rouzée, S. Guérin, O. Faucher, and B. Lavorel. Field-free molecular alignment of asymmetric top molecules using elliptically polarized laser pulses. *Physical Review A*, 77:043412, 2008.

[4] Maxim Artamonov and Tamar Seideman. Theory of three-dimensional alignment by intense laser pulses. *The Journal of Chemical Physics*, 128:154313, 2008.

[5] Maxim Artamonov and Tamar Seideman. Optimal-control approach to field-free three-dimensional alignment of polyatomic molecules. *Physical Review A*, 82:023413, 2010.

[6] JH Posthumus, J Plumridge, MK Thomas, K Codling, LJ Frasinski, AJ Langley, and PF Taday. Dynamic and geometric laser-induced alignment of molecules in intense laser fields. *Journal of Physics B: Atomic, Molecular and Optical Physics*, 31(13): L553–L562, 1998.

[7] Bretislav Friedrich and Dudley Herschbach. Alignment and Trapping of Molecules in Intense Laser Fields. *Physical Review Letters*, 74:4623–4626, 1995.

[8] Tamar Seideman. Rotational excitation and molecular alignment in intense laser fields. *The Journal of Chemical Physics*, 103(18):7887–7896, 1995.

[9] Jakob Juul Larsen, Hirofumi Sakai, CP Safvan, Ida Wendt-Larsen, and Henrik

Stapelfeldt. Aligning molecules with intense nonresonant laser fields. *The Journal of Chemical Physics*, 111(17):7774–7781, 1999.

[10] Lotte Holmegaard, Jens H. Nielsen, Iftach Nevo, Henrik Stapelfeldt, Frank Filsinger, Jochen Küpper, and Gerard Meijer. Laser-Induced Alignment and Orientation of Quantum-State-Selected Large Molecules. *Physical Review Letters*, 102:023001, 2009.

[11] Jeffrey L. Krause, Kenneth J. Schafer, and Kenneth C. Kulander. High-order harmonic generation from atoms and ions in the high intensity regime. *Physical Review Letters*, 68:3535–3538, 1992.

[12] P. B. Corkum. Plasma perspective on strong field multiphoton ionization. *Physical Review Letters*, 71:1994–1997, 1993.

[13] Abdossamad Talebpour, Simon Larochelle, and See-Leang Chin. Non-sequential and sequential double ionization of NO in an intense femtosecond ti: sapphire laser pulse. *Journal of Physics B: Atomic, Molecular and Optical Physics*, 30(7):L245–L250, 1997.

[14] Simon Larochelle, Abdossamad Talebpour, and See-Leang Chin. Non-sequential multiple ionization of rare gas atoms in a Ti:Sapphire laser field. *Journal of Physics B: Atomic, Molecular and Optical Physics*, 31(6):1201, 1998.

[15] F. Rosca-Pruna and M. J. J. Vrakking. Experimental Observation of Revival Structures in Picosecond Laser-Induced Alignment of I_2. *Physical Review Letters*, 87: 153902, 2001.

[16] Lotte Holmegaard, Simon S Viftrup, Vinod Kumarappan, Christer Z Bisgaard, Henrik Stapelfeldt, Edward Hamilton, and Tamar Seideman. Control of rotational wavepacket dynamics in asymmetric top molecules. *Physical Review A*, 75(5):051403, 2007.

[17] Jakob Juul Larsen, Kasper Hald, Nis Bjerre, Henrik Stapelfeldt, and Tamar Seideman.

Three Dimensional Alignment of Molecules Using Elliptically Polarized Laser Fields. *Physical Review Letters*, 85(12):2470, 2000.

[18] S. S. Viftrup, V. Kumarappan, S. Trippel, H. Stapelfeldt, E. Hamilton, and T. Seideman. Holding and spinning molecules in space. *Physical Review Letters*, 99(14): 143602, 2007.

[19] K. F. Lee, D. M. Villeneuve, P. B. Corkum, A. Stolow, and J. G. Underwood. Field-free three-dimensional alignment of polyatomic molecules. *Physical Review Letters*, 97 (17):173001, 2006.

[20] A. Rouzée, S. Guérin, O. Faucher, and B. Lavorel. Field-free molecular alignment of asymmetric top molecules using elliptically polarized laser pulses. *Physical Review A*, 77(4):043412, 2008.

[21] K. H. Kramer and R. B. Bernstein. Focusing and orientation of symmetric-top molecules with the electric six-pole field. *The Journal of Chemical Physics*, 42(2): 767–770, 1965.

[22] H. J. Loesch and A. Remscheid. Brute force in molecular reaction dynamics: A novel technique for measuring steric effects. *The Journal of Chemical Physics*, 93(7):4779–4790, 1990.

[23] Bretislav Friedrich and Dudley Herschbach. Enhanced orientation of polar molecules by combined electrostatic and nonresonant induced dipole forces. *The Journal of Chemical Physics*, 111(14):6157–6160, 1999.

[24] Mette Machholm and Niels E. Henriksen. Field-free orientation of molecules. *Physical Review Letters*, 87:193001, 2001.

[25] Tsuneto Kanai and Hirofumi Sakai. Numerical simulations of molecular orientation

using strong, nonresonant, two-color laser fields. *The Journal of Chemical Physics*, 115(12):5492–5497, 2001.

[26] S. De, I. Znakovskaya, D. Ray, F. Anis, Nora G. Johnson, I. A. Bocharova, M. Magrakvelidze, B. D. Esry, C. L. Cocke, I. V. Litvinyuk, and M. F. Kling. Field-free orientation of CO molecules by femtosecond two-color laser fields. *Physical Review Letters*, 103:153002, 2009.

[27] R. Torres, N Kajumba, Jonathan G Underwood, JS Robinson, S Baker, JWG Tisch, R De Nalda, WA Bryan, R Velotta, C Altucci, et al. Probing orbital structure of polyatomic molecules by high-order harmonic generation. *Physical Review Letters*, 98 (20):203007, 2007.

[28] E. Frumker, C. T. Hebeisen, N. Kajumba, J. B. Bertrand, H. J. Wörner, M. Spanner, D. M. Villeneuve, A. Naumov, and P. B. Corkum. Oriented rotational wave-packet dynamics studies via high harmonic generation. *Physical Review Letters*, 109:113901, 2012.

[29] Christopher J. Hensley, Jie Yang, and Martin Centurion. Imaging of isolated molecules with ultrafast electron pulses. *Physical Review Letters*, 109:133202, 2012.

[30] S. Pabst, P.J. Ho, and R. Santra. Computational studies of x-ray scattering from three-dimensionally-aligned asymmetric-top molecules. *Physical Review A*, 81(4):043425, 2010.

[31] J. Itatani, J. Levesque, D. Zeidler, H. Niikura, H. Pépin, JC Kieffer, P.B. Corkum, and DM Villeneuve. Tomographic imaging of molecular orbitals. *Nature*, 432(7019): 867–871, 2004.

[32] O. Smirnova, Y. Mairesse, S. Patchkovskii, N. Dudovich, D. Villeneuve, P. Corkum, and M.Y. Ivanov. High harmonic interferometry of multi-electron dynamics in molecules. *Nature*, 460(7258):972–977, 2009.

[33] C Vozzi, M Negro, F Calegari, G Sansone, M Nisoli, S De Silvestri, and S Stagira. Generalized molecular orbital tomography. *Nature Physics*, 7(10):822–826, 2011.

[34] Vinod Kumarappan, Lotte Holmegaard, Christian Martiny, Christian B Madsen, Thomas K Kjeldsen, Simon S Viftrup, Lars Bojer Madsen, and Henrik Stapelfeldt. Multiphoton Electron Angular Distributions from Laser-Aligned CS_2 Molecules. *Physical Review Letters*, 100(9):93006, 2008.

[35] Domagoj Pavičić, Kevin F. Lee, D. M. Rayner, P. B. Corkum, and D. M. Villeneuve. Direct measurement of the angular dependence of ionization for n_2, o_2, and co_2 in intense laser fields. *Physical Review Letters*, 98:243001, 2007.

[36] Cosmin I Blaga, Junliang Xu, Anthony D DiChiara, Emily Sistrunk, Kaikai Zhang, Pierre Agostini, Terry A Miller, Louis F DiMauro, and CD Lin. Imaging ultrafast molecular dynamics with laser-induced electron diffraction. *Nature*, 483(7388):194–197, 2012.

[37] S. Baker, J. S. Robinson, C. A. Haworth, H. Teng, R. A. Smith, C. C. Chirila, M. Lein, J. W. G. Tisch, and J. P. Marangos. Probing Proton Dynamics in Molecules on an Attosecond Time Scale. *Science*, 312(5772):424–427, 2006.

[38] Richard N. Zare. *Angular Momentum: Understanding Spatial Aspects in Chemistry and Physics*. Wiley-Interscience, 1988.

[39] John Charles Butcher. *The numerical analysis of ordinary differential equations: Runge-Kutta and general linear methods*. Wiley-Interscience, 1987.

[40] Robynne M. Lock. *High Harmonic Generation from Rotationally Excited Molecules*. PhD thesis, University of Colorado, 2005.

[41] R. M. Lock, S. Ramakrishna, X. Zhou, H. C. Kapteyn, M. M. Murnane, and T. Sei-

deman. Extracting continuum electron dynamics from high harmonic emission from molecules. *Physical Review Letters*, 108:133901, 2012.

[42] Xiaoming Ren, Varun Makhija, and Vinod Kumarappan. Measurement of field-free alignment of jet-cooled molecules by nonresonant femtosecond degenerate four-wave mixing. *Physical Review A*, 85:033405, 2012.

[43] Peter M. Felker. Rotational coherence spectroscopy: studies of the geometries of large gas-phase species by picosecond time-domain methods. *The Journal of Physical Chemistry*, 96(20):7844–7857, 1992.

[44] U. Even, J. Jortner, D. Noy, N. Lavie, and C. Cossart-Magos. Cooling of large molecules below 1 K and He clusters formation. *Journal of Chemical Physics*, 112 (18):8068–8071, 2000.

[45] Lotte Holmegaard, Jens H. Nielsen, Iftach Nevo, Henrik Stapelfeldt, Frank Filsinger, Jochen Kupper, and Gerard Meijer. Laser-Induced Alignment and Orientation of Quantum-State-Selected Large Molecules. *Physical Review Letters*, 102(2):023001–4, 2009.

[46] M. Leibscher, I. Sh. Averbukh, and H. Rabitz. Molecular alignment by trains of short laser pulses. *Physical Review Letters*, 90:213001, 2003.

[47] Christer Z. Bisgaard, Mikael D. Poulsen, Emmanuel Péronne, Simon S. Viftrup, and Henrik Stapelfeldt. Observation of enhanced field-free molecular alignment by two laser pulses. *Physical Review Letters*, 92:173004, 2004.

[48] James P. Cryan, Philip H. Bucksbaum, and Ryan N. Coffee. Field-free alignment in repetitively kicked nitrogen gas. *Physical Review A*, 80:063412, 2009.

[49] A.T.J.B. Eppink and D.H. Parker. Velocity map imaging of ions and electrons using

electrostatic lenses: Application in photoelectron and photofragment ion imaging of molecular oxygen. *Review of Scientific Instruments*, 68:3477, 1997.

[50] Reinhard Dörner, Volker Mergel, Ottmar Jagutzki, Lutz Spielberger, Joachim Ullrich, Robert Moshammer, and Horst Schmidt-Böcking. Cold target recoil ion momentum spectroscopy: a momentum microscope to view atomic collision dynamics. *Physics Reports*, 330(2):95–192, 2000.

[51] Itzik Ben-Itzhak, Pengqian Wang, Jiangfan Xia, A Max Sayler, Mark A Smith, JW Maseberg, Kevin D Carnes, and Brett D Esry. Dissociation and ionization of molecular ions by ultra-short intense laser pulses probed by coincidence 3D momentum imaging. *Nuclear Instruments and Methods in Physics Research Section B: Beam Interactions with Materials and Atoms*, 233(1):56–61, 2005.

[52] Bor-Yu Chang, Rama C. Hoetzlein, Julie A. Mueller, Joseph D. Geiser, and Paul L. Houston. Improved two-dimensional product imaging: The real-time ion-counting method. *Review of Scientific Instruments*, 69(4):1665–1670, 1998.

[53] Marc J. J. Vrakking. An iterative procedure for the inversion of two-dimensional ion/photoelectron imaging experiments. *Review of Scientific Instruments*, 72(11): 4084–4089, 2001.

[54] Gabor T Herman. *Fundamentals of computerized tomography: image reconstruction from projections*. Springer, 2009.

[55] Richard N Zare. Dissociation of H by Electron Impact: Calculated Angular Distribution. *The Journal of Chemical Physics*, 47:204, 1967.

[56] Vinod Kumarappan, Christer Z Bisgaard, Simon S Viftrup, Lotte Holmegaard, and Henrik Stapelfeldt. Role of rotational temperature in adiabatic molecular alignment. *The Journal of Chemical Physics*, 125:194309, 2006.

[57] Iftach Nevo, Lotte Holmegaard, Jens H. Nielsen, Jonas L. Hansen, Henrik Stapelfeldt, Gerard Filsinger, Frankand Meijer, and Jochen Kupper. Laser-induced 3D alignment and orientation of quantum state-selected molecules. *Physical Chemistry Chemical Physics*, 11(42):9912, 2009.

[58] L. Holmegaard, J.L. Hansen, L. Kalhøj, S.L. Kragh, H. Stapelfeldt, F. Filsinger, J. Küpper, G. Meijer, D. Dimitrovski, M. Abu-Samha, et al. Photoelectron angular distributions from strong-field ionization of oriented molecules. *Nature Physics*, 6 (6):428–432, 2010.

[59] Takuya Horio and Toshinori Suzuki. Multihit two-dimensional charged-particle imaging system with real-time image processing at 1000 frames/s. *Review of Scientific Instruments*, 80(1):013706, 2009.

[60] Andres Huertas and Gerard Medioni. Detection of intensity changes with subpixel accuracy using laplacian-gaussian masks. *Pattern Analysis and Machine Intelligence, IEEE Transactions on*, (5):651–664, 1986.

[61] James Lee, R Haralick, and Linda Shapiro. Morphologic edge detection. *Robotics and Automation, IEEE Journal of*, 3(2):142–156, 1987.

[62] Daniel R Baum and James M Winget. Real time radiosity through parallel processing and hardware acceleration. In *ACM SIGGRAPH Computer Graphics*, volume 24, pages 67–75. ACM, 1990.

[63] T Wittmann, B Horvath, W Helml, MG Schätzel, X Gu, AL Cavalieri, GG Paulus, and R Kienberger. Single-shot carrier–envelope phase measurement of few-cycle laser pulses. *Nature Physics*, 5(5):357–362, 2009.

[64] F. Sussmann, S. Zherebtsov, J. Plenge, Nora G. Johnson, M. Kubel, A. M. Sayler, V. Mondes, C. Graf, E. Ruhl, G. G. Paulus, D. Schmischke, P. Swrschek, and M. F.

Kling. Single-shot velocity-map imaging of attosecond light-field control at kilohertz rate. *Review of Scientific Instruments*, 82(9):093109, 2011.

[65] Stefan Pabst and Robin Santra. Alignment of asymmetric-top molecules using multiple-pulse trains. *Physical Review A*, 81(6):065401, 2010.

[66] Varun Makhija, Xiaoming Ren, and Vinod Kumarappan. Metric for three-dimensional alignment of molecules. *Physical Review A*, 85:033425, 2012.

[67] Du Q. Huynh. Metrics for 3D rotations: Comparison and analysis. *Journal of Mathematical Imaging and Vision*, 35:155–164, 2009. ISSN 0924-9907.

[68] H. Goldstein. *Classical Mechanics*. Addison-Wesley, 2nd edition, 1980.

[69] Gabor T Herman. *Fundamentals of computerized tomography: image reconstruction from projections*. Springer, 2009.

[70] Matthew Comstock, Vahan Senekerimyan, and Marcos Dantus. Ultrafast Laser Induced Molecular Alignment and Deformation: Experimental Evidence from Neutral Molecules and from Fragment Ions. *The Journal of Physical Chemistry A*.

[71] V. Renard, M. Renard, A. Rouzée, S. Guérin, H. R. Jauslin, B. Lavorel, and O. Faucher. Nonintrusive monitoring and quantitative analysis of strong laser-field-induced impulsive alignment. *Physical Review A*, 70:033420, 2004.

[72] Sze-cheng Yang and Richard Bersohn. Theory of the angular distribution of molecular photofragments. *The Journal of Chemical Physics*, 61:4400, 1974.

[73] A. Rouzee, V. Renard, S. Guerin, O. Faucher, and B. Lavorel. Optical gratings induced by field-free alignment of molecules. *Physical Review A*, 75(1):013419, 2007.

[74] Douglas A Greenhalgh. Comments on the use of BOXCARS for gas-phase CARS spectroscopy. *Journal of Raman Spectroscopy*, 14(3):150–153, 1983.

[75] Ryan P. Davis, Andrew J. Moad, G. Scott Goeken, Ronald D. Wampler, and Garth J. Simpson. Selection Rules and Symmetry Relations for Four-Wave Mixing Measurements of Uniaxial Assemblies. *The Journal of Physical Chemistry B*, 112(18):5834–5848, 2008.

[76] Nobuyuki Matsuzawa and David A. Dixon. Density functional theory predictions of polarizabilities and first- and second-order hyperpolarizabilities for molecular systems. *The Journal of Physical Chemistry*, 98(10):2545–2554, 1994.

[77] G. Maroulis and D. Bishop. Electric polarizabilities and hyperpolarizabilities for the ground state of the nitrogen molecule. *Molecular Physics*, 58(2):273–283, 1986.

[78] Tamar Seideman. Revival Structure of Aligned Rotational Wave Packets. *Physical Review Letters*, 83:4971–4974, 1999.

[79] A. M. Weiner, J. P. Heritage, and J. A. Salehi. Encoding and decoding of femtosecond pulses. *Optics Letters*, 13(4):300–302, 1988.

[80] A. M. Weiner, D. E. Leaird, J. S. Patel, and J. R. Wullert. Programmable femtosecond pulse shaping by use of a multielement liquid-crystal phase modulator. *Optics Letters*, 15(6):326–328, 1990.

[81] Lotte Holmegaard, Simon S. Viftrup, Vinod Kumarappan, Christer Z. Bisgaard, Henrik Stapelfeldt, Edward Hamilton, and Tamar Seideman. Control of rotational wavepacket dynamics in asymmetric top molecules. *Physical Review A*, 75:051403, 2007.

[82] Shian Zhang, Chenhui Lu, Junhui Shi, Tianqing Jia, Zugeng Wang, and Zhenrong Sun. Field-free molecular alignment by shaping femtosecond laser pulse with cubic phase modulation. *Physical Review A*, 84:013408, 2011.

[83] Philippe Antoine, Anne L'Huillier, and Maciej Lewenstein. Attosecond pulse trains using high–order harmonics. *Physical Review Letters*, 77(7):1234–1237, 1996.

[84] Ivan P Christov, Margaret M Murnane, and Henry C Kapteyn. High-harmonic generation of attosecond pulses in the single-cycle regime. *Physical Review Letters*, 78(7): 1251–1254, 1997.

[85] PM Paul, ES Toma, P Breger, Genevive Mullot, F Augé, Ph Balcou, HG Muller, and P Agostini. Observation of a train of attosecond pulses from high harmonic generation. *Science*, 292(5522):1689–1692, 2001.

[86] PB Corkum and Ferenc Krausz. Attosecond science. *Nature Physics*, 3(6):381–387, 2007.

[87] Carsten Winterfeldt, Christian Spielmann, and Gustav Gerber. Colloquium: Optimal control of high-harmonic generation. *Reviews of Modern Physics*, 80:117–140, 2008.

[88] E. Cormier and M. Lewenstein. Optimizing the efficiency in high order harmonic generation optimization by two-color fields. *The European Physical Journal D - Atomic, Molecular, Optical and Plasma Physics*, 12(2):227–233, 2000. ISSN 1434-6060.

[89] Yu Oishi, Masanori Kaku, Akira Suda, Fumihiko Kannari, and Katsumi Midorikawa. Generation of extreme ultraviolet continuum radiation driven by a sub-10-fs two-color field. *Optics Express*, 14(16):7230–7237, 2006.

[90] I Jong Kim, Chul Min Kim, Hyung Taek Kim, Gae Hwang Lee, Yong Soo Lee, Ju Yun Park, David Jaeyun Cho, and Chang Hee Nam. Highly efficient high-harmonic generation in an orthogonally polarized two-color laser field. *Physical Review Letters*, 94: 243901, 2005.

[91] M. Bellini, C. Lyngå, A. Tozzi, M. B. Gaarde, T. W. Hänsch, A. L'Huillier, and C.-G. Wahlström. Temporal Coherence of Ultrashort High-Order Harmonic Pulses. *Physical Review Letters*, 81:297–300, 1998.

[92] G. Sansone, C. Vozzi, S. Stagira, and M. Nisoli. Nonadiabatic quantum path analysis of high-order harmonic generation: Role of the carrier-envelope phase on short and long paths. *Physical Review A*, 70:013411, 2004.

[93] Xiaoshi Zhang, Amy L Lytle, Tenio Popmintchev, Xibin Zhou, Henry C Kapteyn, Margaret M Murnane, and Oren Cohen. Quasi-phase-matching and quantum-path control of high-harmonic generation using counterpropagating light. *Nature Physics*, 3(4):270–275, 2007.

[94] W Cao, G Laurent, Cheng Jin, H Li, Z Wang, CD Lin, I Ben-Itzhak, and CL Cocke. Spectral splitting and quantum path study of high-harmonic generation from a semi-infinite gas cell. *Journal of Physics B: Atomic, Molecular and Optical Physics*, 45(7): 074013, 2012.

[95] Yusuke Tamaki, Jiro Itatani, Yutaka Nagata, Minoru Obara, and Katsumi Midorikawa. Highly efficient, phase-matched high-harmonic generation by a self-guided laser beam. *Physical Review Letters*, 82:1422–1425, 1999.

[96] Charles G. Durfee, Andy R. Rundquist, Sterling Backus, Catherine Herne, Margaret M. Murnane, and Henry C. Kapteyn. Phase matching of high-order harmonics in hollow waveguides. *Physical Review Letters*, 83:2187–2190, 1999.

[97] I. P. Christov, R. Bartels, H. C. Kapteyn, and M. M. Murnane. Attosecond time-scale intra-atomic phase matching of high harmonic generation. *Physical Review Letters*, 86:5458–5461, 2001.

[98] P. M. Paul, E. S. Toma, P. Breger, G. Mullot, F. Aug, Ph. Balcou, H. G. Muller, and P. Agostini. Observation of a Train of Attosecond Pulses from High Harmonic Generation. *Science*, 292(5522):1689–1692, 2001.

[99] G. Sansone, E. Benedetti, F. Calegari, C. Vozzi, L. Avaldi, R. Flammini, L. Poletto,

P. Villoresi, C. Altucci, R. Velotta, S. Stagira, S. De Silvestri, and M. Nisoli. Isolated Single-Cycle Attosecond Pulses. *Science*, 314(5798):443–446, 2006.

[100] Hiroki Mashiko, Steve Gilbertson, Chengquan Li, Sabih D. Khan, Mahendra M. Shakya, Eric Moon, and Zenghu Chang. Double optical gating of high-order harmonic generation with carrier-envelope phase stabilized lasers. *Physical Review Letters*, 100: 103906, 2008.

[101] Ximao Feng, Steve Gilbertson, Hiroki Mashiko, He Wang, Sabih D. Khan, Michael Chini, Yi Wu, Kun Zhao, and Zenghu Chang. Generation of isolated attosecond pulses with 20 to 28 femtosecond lasers. *Physical Review Letters*, 103:183901, 2009.

[102] EL Falcão-Filho, VM Gkortsas, Ariel Gordon, and Franz X Kärtner. Analytic scaling analysis of high harmonic generation conversion efficiency. *Optics Express*, 17(13): 11217–11229, 2009.

[103] AD Shiner, C Trallero-Herrero, N Kajumba, H-C Bandulet, D Comtois, F Légaré, M Giguère, J-C Kieffer, PB Corkum, and DM Villeneuve. Wavelength scaling of high harmonic generation efficiency. *Physical Review Letters*, 103(7):073902–1, 2009.

[104] Vasileios-Marios Gkortsas, Siddharth Bhardwaj, Edilson L Falcão-Filho, Kyung-Han Hong, Ariel Gordon, and Franz X Kärtner. Scaling of high harmonic generation conversion efficiency. *Journal of Physics B: Atomic, Molecular and Optical Physics*, 44(4):045601, 2011.

[105] MV Frolov, NL Manakov, TS Sarantseva, M Yu Emelin, M Yu Ryabikin, and Anthony F Starace. Analytic description of the high-energy plateau in harmonic generation by atoms: can the harmonic power increase with increasing laser wavelengths? *Physical Review Letters*, 102(24):243901, 2009.

[106] MV Frolov, NL Manakov, and Anthony F Starace. Wavelength scaling of high-

harmonic yield: threshold phenomena and bound state symmetry dependence. *Physical review letters*, 100(17):173001, 2008.

[107] M. Schnürer, Ch. Spielmann, P. Wobrauschek, C. Streli, N. H. Burnett, C. Kan, K. Ferencz, R. Koppitsch, Z. Cheng, T. Brabec, and F. Krausz. Coherent 0.5-kev X-ray emission from Helium Driven by a sub-10-fs laser. *Physical Review Letters*, 80: 3236–3239, 1998.

[108] Ariel Gordon and Franz Kärtner. Scaling of kev hhg photon yield with drive wavelength. *Optics Express*, 13(8):2941–2947, 2005.

[109] M Lewenstein, Ph Balcou, M Yu Ivanov, Anne Luillier, and Paul B Corkum. Theory of high-harmonic generation by low-frequency laser fields. *Physical Review A*, 49(3): 2117, 1994.

[110] JP Marangos*, C Altucci, R Velotta, E Heesel, E Springate, M Pascolini, L Poletto, P Villoresi, C Vozzi, G Sansone, et al. Molecular orbital dependence of high-order harmonic generation. *Journal of Modern Optics*, 53(1-2):97–111, 2006.

[111] Anh-Thu Le, R. R. Lucchese, S. Tonzani, T. Morishita, and C. D. Lin. Quantitative rescattering theory for high-order harmonic generation from molecules. *Physical Review A*, 80:013401, 2009.

[112] Cheng Jin. *Theory of nonlinear propagation of high harmonics generated in a gaseous medium*. PhD thesis, Kansas State University, 2012.

[113] J. Muth-Böhm, A. Becker, and F. H. M. Faisal. Suppressed molecular ionization for a class of diatomics in intense femtosecond laser fields. *Physical Review Letters*, 85: 2280–2283, 2000.

[114] Thomas Kim Kjeldsen and Lars Bojer Madsen. Strong-field ionization of diatomic

molecules and companion atoms: Strong-field approximation and tunneling theory including nuclear motion. *Physical Review A*, 71:023411, 2005.

[115] Robert R. Lucchese, Georges Raseev, and Vincent McKoy. Studies of differential and total photoionization cross sections of molecular nitrogen. *Physical Review A*, 25: 2572–2587, 1982.

[116] RE STRATMANN and RR LUCCHESE. A graphical unitary-group approach to study multiplet specific multichannel electron correlation-effects in the photoionization of O-2. *JOURNAL OF CHEMICAL PHYSICS*, 102(21):8493–8505, 1995.

[117] Zhangjin Chen, Anh-Thu Le, Toru Morishita, and C. D. Lin. Quantitative rescattering theory for laser-induced high-energy plateau photoelectron spectra. *Physical Review A*, 79:033409, 2009.

[118] Anh-Thu Le, R. R. Lucchese, and C. D. Lin. Polarization and ellipticity of high-order harmonics from aligned molecules generated by linearly polarized intense laser pulses. *Physical Review A*, 82:023814, 2010.

[119] T. Kanai, S. Minemoto, and H. Sakai. Quantum interference during high-order harmonic generation from aligned molecules. *Nature*, 435(7041):470–474, 2005.

[120] Brian K. McFarland, Joseph P. Farrell, Philip H. Bucksbaum, and Markus Ghr. High harmonic generation from multiple orbitals in N2. *Science*, 322(5905):1232–1235, 2008.

[121] H. J. Worner, J. B. Bertrand, D. V. Kartashov, P. B. Corkum, and D. Villeneuve. Following a chemical reaction using high-harmonic interferometry. *Nature*, 466:604?07, 2010.

[122] Anh-Thu Le, RR Lucchese, MT Lee, and CD Lin. Probing molecular frame photoionization via laser generated high-order harmonics from aligned molecules. *Physical Review Letters*, 102(20):203001, 2009.

[123] Guoli Wang, Cheng Jin, Anh-Thu Le, and CD Lin. Conditions for extracting photoionization cross sections from laser-induced high-order-harmonic spectra. *Physical Review A*, 86(1):015401, 2012.

[124] J. B. Bertrand, H. J. Wörner, P. Hockett, D. M. Villeneuve, and P. B. Corkum. Revealing the cooper minimum of $\mathbf{n}_2$ by molecular frame high-harmonic spectroscopy. *Physical Review Letters*, 109:143001, 2012.

[125] A. Rupenyan, J. B. Bertrand, D. M. Villeneuve, and H. J. Wörner. All-optical measurement of high-harmonic amplitudes and phases in aligned molecules. *Physical Review Letters*, 108:033903, 2012.

[126] Cheng Jin, Julien B. Bertrand, R. R. Lucchese, H. J. Wörner, Paul B. Corkum, D. M. Villeneuve, Anh-Thu Le, and C. D. Lin. Intensity dependence of multiple orbital contributions and shape resonance in high-order harmonic generation of aligned N_2 molecules. *Physical Review A*, 85:013405, 2012.

[127] Maciej Lewenstein, Pascal Salieres, and Anne Lhuillier. Phase of the atomic polarization in high-order harmonic generation. *Physical Review A*, 52(6):4747, 1995.

[128] S. Ramakrishna and Tamar Seideman. Information content of high harmonics generated from aligned molecules. *Physical Review Letters*, 99:113901, 2007.

[129] J. P. Farrell, B. K. McFarland, P. H. Bucksbaum, and M. Gühr. Calibration of a high harmonicspectrometer by laser induced plasma emission. *Optics Express*, 17(17): 15134–15144, 2009.

[130] Yu Ralchenko, FC Jou, DE Kelleher, AE Kramida, A Musgrove, J Reader, WL Wiese, and K Olsen. NIST atomic spectra database (version 3.1. 0). *NIST Atomic Spectra Database, NIST Standard Reference Database*, (78), 2006.

[131] Hadas Soifer, P Botheron, D Shafir, A Diner, O Raz, BD Bruner, Yann Mairesse, Bernard Pons, and Nirit Dudovich. Near-threshold high-order harmonic spectroscopy with aligned molecules. *Physical Review Letters*, 105(14):143904, 2010.

[132] Donald W Marquardt. An algorithm for least-squares estimation of nonlinear parameters. *Journal of the Society for Industrial & Applied Mathematics*, 11(2):431–441, 1963.

[133] JB Bertrand, HJ Wörner, P Salières, DM Villeneuve, and PB Corkum. Linked attosecond phase interferometry for molecular frame measurements. *Nature Physics*, 2013.

[134] Xibin Zhou, Robynne Lock, Nick Wagner, Wen Li, Henry C. Kapteyn, and Margaret M. Murnane. Elliptically Polarized High-Order Harmonic Emission from Molecules in Linearly Polarized Laser Fields. *Physical Review Letters*, 102:073902, 2009.

[135] LV Keldysh. Ionization in the field of a strong electromagnetic wave. *Sov. Phys. JETP*, 20(5):1307–1314, 1965.

[136] I. V. Litvinyuk, Kevin F. Lee, P. W. Dooley, D. M. Rayner, D. M. Villeneuve, and P. B. Corkum. Alignment-dependent strong field ionization of molecules. *Physical Review Letters*, 90:233003, 2003.

[137] Jonas L Hansen, Lotte Holmegaard, Jens H Nielsen, Henrik Stapelfeldt, Darko Dimitrovski, and Lars Bojer Madsen. Orientation-dependent ionization yields from strong-field ionization of fixed-in-space linear and asymmetric top molecules. *Journal of Physics B: Atomic, Molecular and Optical Physics*, 45(1):015101, 2012.

[138] Maxim V Ammosov, Nikolai B Delone, and Vladimir P Krainov. Tunnel ionization of complex atoms and atomic ions in electromagnetic field. In *1986 Quebec Symposium*, pages 138–141. International Society for Optics and Photonics, 1986.

[139] S. Augst, D. Strickland, D. D. Meyerhofer, S. L. Chin, and J. H. Eberly. Tunneling ionization of noble gases in a high-intensity laser field. *Physical Review Letters*, 63: 2212–2215, 1989.

[140] M. Lewenstein, Ph. Balcou, M. Yu. Ivanov, Anne L'Huillier, and P. B. Corkum. Theory of high-harmonic generation by low-frequency laser fields. *Physical Review A*, 49:2117–2132, 1994.

[141] X. M. Tong, Z. X. Zhao, and C. D. Lin. Theory of molecular tunneling ionization. *Physical Review A*, 66:033402, 2002.

[142] T. Peter Rakitzis, Alrik J. van den Brom, and Maurice H. M. Janssen. Directional dynamics in the photodissociation of oriented molecules. *Science*, 303(5665):1852–1854, 2004.

[143] Omair Ghafur, Arnaud Rouzee, Arjan Gijsbertsen, Wing Kiu Siu, Steven Stolte, and Marc J. J. Vrakking. Impulsive orientation and alignment of quantum-state-selected NO molecules. *Nature Physics*, 5(4):289–293, 2009.

[144] JJ ávan Leuken et al. Hexapole state selection and focusing vs. brute force orientation of beam molecules. *Journal of the Chemical Society, Faraday Transactions*, 91(2): 205–214, 1995.

[145] Long Cai, Jotin Marango, and Bretislav Friedrich. Time-dependent alignment and orientation of molecules in combined electrostatic and pulsed nonresonant laser fields. *Physical Review Letters*, 86:775–778, 2001.

[146] Hirofumi Sakai, Shinichirou Minemoto, Hiroshi Nanjo, Haruka Tanji, and Takayuki Suzuki. Controlling the orientation of polar molecules with combined electrostatic and pulsed, nonresonant laser fields. *Physical Review Letters*, 90:083001, 2003.

[147] Lotte Holmegaard, Jens H. Nielsen, Iftach Nevo, Henrik Stapelfeldt, Frank Filsinger, Jochen Küpper, and Gerard Meijer. Laser-induced alignment and orientation of quantum-state-selected large molecules. *Physical Review Letters*, 102:023001, 2009.

[148] Yu Sugawara, Akihisa Goban, Shinichirou Minemoto, and Hirofumi Sakai. Laser-field-free molecular orientation with combined electrostatic and rapidly-turned-off laser fields. *Physical Review A*, 77:031403, 2008.

[149] Omair Ghafur, Arnaud Rouzée, Arjan Gijsbertsen, Wing Kiu Siu, Steven Stolte, and Marc JJ Vrakking. Impulsive orientation and alignment of quantum-state-selected NO molecules. *Nature physics*, 5(4):289–293, 2009.

[150] Chaochao Qin, Ying Tang, Yanmei Wang, and Bing Zhang. Field-free orientation of CO by a terahertz few-cycle pulse. *Physical Review A*, 85:053415, 2012.

[151] Sharly Fleischer, Yan Zhou, Robert W. Field, and Keith A. Nelson. Molecular orientation and alignment by intense single-cycle THz pulses. *Physical Review Letters*, 107:163603, 2011.

[152] R. Tehini and D. Sugny. Field-free molecular orientation by nonresonant and quasiresonant two-color laser pulses. *Physical Review A*, 77:023407, 2008.

[153] Michael Spanner, Serguei Patchkovskii, Eugene Frumker, and Paul Corkum. Mechanisms of two-color laser-induced field-free molecular orientation. *Physical Review Letters*, 109:113001, 2012.

[154] Jian Wu and Heping Zeng. Field-free molecular orientation control by two ultrashort dual-color laser pulses. *Physical Review A*, 81:053401, 2010.

[155] Shian Zhang, Chenhui Lu, Tianqing Jia, Zugeng Wang, and Zhenrong Sun. Controlling field-free molecular orientation with combined single- and dual-color laser pulses. *Physical Review A*, 83:043410, 2011.

[156] Katsuhiro Nakajima, Hiroya Abe, and Yukiyoshi Ohtsuki. Optimal control simulation of field-free molecular orientation: Alignment-enhanced molecular orientation. *The Journal of Physical Chemistry A*, 116(46):11219–11227, 2012.

[157] R. Tehini, Md Z. Hoque, O. Faucher, and D. Sugny. Field-free molecular orientation of $^1\Sigma$ and $^2\Pi$ molecules at high temperature. *Physical Review A*, 85:043423, 2012.

[158] Dipanwita Ray. *Photo-electron Momentum Distribution and Electron Localization Studies from Laser-Induced Atomic and Molecular Dissociations*. PhD thesis, Kansas State University, 2010.

[159] Kevin F. Lee, D. M. Villeneuve, P. B. Corkum, and E. A. Shapiro. Phase control of rotational wave packets and quantum information. *Physical Review Letters*, 93: 233601, 2004.

[160] W Boutu, S Haessler, H Merdji, P Breger, G Waters, M Stankiewicz, LJ Frasinski, R Taieb, J Caillat, A Maquet, et al. Coherent control of attosecond emission from aligned molecules. *Nature Physics*, 4(7):545–549, 2008.

[161] Kirk A Peterson and Thom H Dunning. The CO molecule: the role of basis set and correlation treatment in the calculation of molecular properties. *Journal of Molecular Structure: THEOCHEM*, 400:93–117, 1997.

[162] Andrew A Quong and Mark R Pederson. Density-functional-based linear and nonlinear polarizabilities of fullerene and benzene molecules. *Physical Review B*, 46(19):12906, 1992.

[163] Magdalena Pecul. Density functional and coupled cluster calculations of dynamic hyperpolarizabilities and their geometry derivatives. *Chemical Physics Letters*, 404 (1):217–226, 2005.

[164] Robert W Boyd. *Nonlinear optics*. Academic press, 2003.

Appendix A

List of rotational constants, polarizabilities, spin statistics and hyperpolarizabilities for different molecules.

For $\langle\cos^2\theta\rangle$, $\langle\cos\theta\rangle$ and $\langle D^j_{00}\rangle$ calculations, rotational constants, polarizabilities and spin statistics for different molecules used in this thesis are listed in Tab. A.1 [111, 161] and Tab. A.2 [76, 162, 163]:

Molecule	B	$\alpha_{\parallel}$	$\alpha_{\perp}$	$\text{Spin}_{\text{even}}$	Spin_{odd}
N_2	1.99824	15	9.8	2/3	1/3
O_2	1.43768	14.41	7.32	0	1
CO_2	0.39021	27.25	13.1	1	0
N_2O	0.41901	23.693	11.921	1/2	1/2
CO	1.93128	15.53	11.82	1/2	1/2

Table A.1: *List of rotational constants, polarizabilities and spin statistics for different linear molecules. Rotational constants are in units of cm^{-1}, polarizabilities are in atomic units. In addition, the perpendicular and parallel components of the first order hyper-polarizability of CO are $\beta_{\parallel}$=29.9 and $\beta_{\perp}$=7.9 in atomic units.*

For χ_{ijkl} calculations, second order hyper-polarizabilities for different molecules used in this thesis are listed in Tab. A.3 [76, 77, 162]:

Molecule	A	B	C	α_{xx}	α_{yy}	α_{zz}	$\text{Spin}_{\text{even}}$	Spin_{odd}
C_6H_6	0.1896	0.1896	0.0948	12.45	12.46	6.55	1/2	1/2
C_6H_5I	0.189	0.025	0.022	15.3	10.2	21.5	5/8	3/8

Table A.2: *List of rotational constants, polarizabilities and spin statistics for symmetric top and asymmetric top molecules. Rotational constants are in units of cm^{-1}, polarizabilities are in atomic units. A, B and C correspond to the fastest axis, intermediate axis and the slowest axis, x, y and z are the corresponding polarizabilities.*

Molecule	γ_{xxxx}	γ_{yyyy}	γ_{zzzz}	γ_{xxzz}	γ_{xxyy}	γ_{yyzz}
N_2	544	544	1180	300	544	300
C_6H_6	1.71	1.71	0.39	0.4	0.51	0.4
C_6H_5I	9.775	17.303	33.076	5.011	3.981	3.599

Table A.3: *List of hyper-polarizabilities for different molecules, values for N_2 are in atomic units and the other two are in units of 10^{-36} esu.*

Appendix B

Derivation of the expression of the third order susceptibility tensor element χ_{ZZZZ} for nitrogen and benzene.

In DFWM process, the electric field of the three input probe beams can be expressed as: $E_i(r,t) = A_i(r)\exp[i(k_i \cdot r - \omega t)]$, where i=1,2,3, and $r = X, Y, Z$. $A_i(r)$ is the amplitude of the field, k_i is the wave vector and ω is the frequency of the pulse, in a fully degenerated case, all the probes have the same frequency, so we can get the nonlinear third order polarization as following:

$$P_i^{(3)} = 6\chi_{ijkl}^{(3)}(-\omega;\omega,\omega,-\omega)E_j E_k E_l^*. \tag{B.1}$$

The wave equation for the signal beam is (Eq. (2.1.23) from Boyd Nonlinear Optics [164]):

$$\bigtriangledown^2 E_4(r) + \frac{\omega^2\epsilon^{(1)}(\omega)}{c^2}E_4(r) = -\frac{\omega^2}{\epsilon_0 c^2}P_4^{(3)}(r), \tag{B.2}$$

where $\epsilon^{(1)}(\omega)$ is the dielectric tensor and c is the speed of light. For the $ZZZZ$ component, where all probes are polarized in Z axis, from Eq. B.1 and B.2, we can get,

$$[\frac{d^2A_4}{dz^2} + 2ik_4\frac{dA_4}{dz} - k_4^2A_4 + \frac{\omega^2\epsilon^{(1)}(\omega)}{c^2}E_4]\exp(ik_4z)$$
$$= -\frac{6\omega^2}{\epsilon_0 c^2}\chi^{(3)}_{ZZZZ}A_1A_2A_3^*\exp[i(k_1+k_2-k_3)z]. \quad \text{(B.3)}$$

Notice that $k_4^2 = \frac{\omega^2\epsilon^{(1)}(\omega)}{c^2}$, and $k_1 + k_2 - k_3 - k_4 = 0$ (phase matching condition), use slowly varying amplitude approximation, we have:

$$\frac{dA_4}{dz} = \frac{i3\chi^{(3)}_{ZZZZ}\omega^2}{k_4\epsilon_0 c^2}A_1A_2A_3^*. \quad \text{(B.4)}$$

Assuming no depletion of the three probes and use boundary condition $A_4(0) = 0$, do the integration, we get,

$$A_4 = \frac{i3L\chi^{(3)}_{ZZZZ}\omega^2}{k_4\epsilon_0 c^2}A_1A_2A_3^*, \quad \text{(B.5)}$$

where L is the length of target gas along the laser propagation direction assuming a uniform gas density distribution. In the case of a gas jet, where the gas density produced by the jet is not uniform along the laser propagation direction, A_4 will be integrated along the z axis. In experiment, we are measuring A_4^2, therefore we get the signal is proportional to the square of the polarization of the signal beam: $P_i^{(3)}$.

In order to derive the expression of χ_{ZZZZ}, we start with Eq. 4.2, rotational matrix R can be found by multiplying the rotational matrix about all three azimuth angles θ, ϕ and χ. Those are Eq. 3.33-3.35 from Zare [38]:

$$R(\theta) = \begin{pmatrix} \cos\theta & 0 & -\sin\theta \\ 0 & 1 & 0 \\ \sin\theta & 0 & \cos\theta \end{pmatrix} \quad \text{(B.6)}$$

$$R(\phi) = \begin{pmatrix} \cos\phi & \sin\phi & 0 \\ -\sin\phi & \cos\phi & 0 \\ 0 & 0 & 1 \end{pmatrix} \quad \text{(B.7)}$$

$$R(\chi) = \begin{pmatrix} \cos\chi & \sin\chi & 0 \\ -\sin\chi & \cos\chi & 0 \\ 0 & 0 & 1 \end{pmatrix} \quad \text{(B.8)}$$

Then $R = R(\theta).R(\phi).R(\chi)$, use Eq. 4.2 and the hyper-polarizability values listed in Appendix A, χ_{ijkl} can be expressed in terms of $\cos\theta$ for linear and symmetric top molecules. Since in pump-DFWM experiment, we are measuring $\chi^2_{ZZZZ}/\chi^2_{ZZZZ-iso}$, we can calculate $\chi^2_{ZZZZ-iso}$ by integrating over all angles, χ^2_{ZZZZ} is integrated over ϕ and χ to give the θ dependence, for nitrogen:

$$\frac{\chi^2_{ZZZZ}}{\chi^2_{ZZZZ-iso}}(\theta) = 0.47411 + 1.24106\cos^2\theta + 0.67969\cos^4\theta - 0.17338\cos^6\theta + 0.00925\cos^8\theta \tag{B.9}$$

For benzene:

$$\frac{\chi^2_{ZZZZ}}{\chi^2_{ZZZZ-iso}}(\theta) = 1.55064 - 1.73388\cos^2\theta - 0.15537\cos^4\theta + 0.35654\cos^6\theta + 0.06712\cos^8\theta \tag{B.10}$$

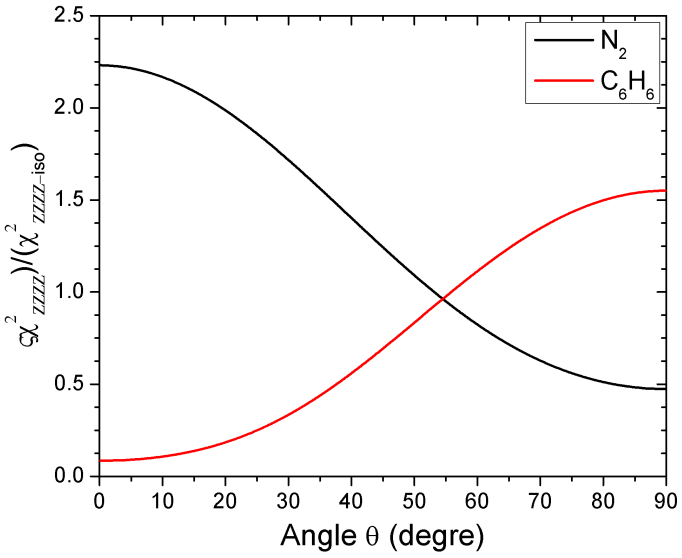

Figure B.1: *The trace of $\chi^2_{ZZZZ}/\chi^2_{ZZZZ-iso}$ as a function of θ for both nitrogen (black) and benzene (red).*

Fig. B.1 shows $\chi^2_{ZZZZ}/\chi^2_{ZZZZ-iso}$ as a function of angle θ, we can see that for N_2, as the molecules get aligned, or as θ go towards 0, it has a maximum value, therefore, we expect

the measured signal to go up at alignment moment. In the case of benzene, we expect the measured signal to go up at anti-alignment moment (explained in Chap. 4).

When averaging over alignment distribution, $\langle \cos^{2n}\theta \rangle$ $(n = 1, 2, 3, 4)$ can be calculated by solving TDSE, from which $\left\langle \chi^2_{ZZZZ}/\chi^2_{ZZZZ-iso}(\theta) \right\rangle$ is obtained and compared to the measurement.

Appendix C

Coefficients obtained from fitting harmonic delay and angle scans.

In the case of fitting harmonic delay scans, the harmonic intensities S are fitted using,

$$S(\omega, t) = \left[\sum_j a_j \left\langle D^j_{00} \right\rangle (t)\right]^2. \tag{C.1}$$

With a molecular rotational temperature of 30 K, pump1 of 80 fs and 48 TW/cm^2, pump2 of 80 fs and 56 TW/cm^2 and a separation of 3.94 ps, the extracted coefficients a_j are listed in Tab. C.1 along with an error bar within 80% confident level,

In the case of fitting harmonic angle scans, the harmonic intensities S are fitted using,

$$S(\omega, \alpha) = \left[\sum_j b_j \left\langle D^j_{00} \right\rangle (\alpha)\right]^2. \tag{C.2}$$

Using the same molecular rotational temperature and laser conditions as in the case of the delay scan fittings, the extracted coefficients b_j are listed in Tab. C.2 along with an error bar within 80% confident level,

Harmonic order	a_0	a_2	a_4	a_6
H9	0.9845± 0.0045	0.408± 0.0241	0.0495± 0.0527	-0.1508± 0.0762
H11	1.0309± 0.0016	-0.1329± 0.0082	0.13± 0.0186	-0.0131± 0.0279
H13	1.0395± 0.0035	0.9± 0.0195	0.4529± 0.0424	-0.188± 0.0588
H15	1.0477± 0.0055	1.4193± 0.0313	0.3977± 0.0673	-0.1362± 0.0907
H17	1.0848± 0.0061	1.3205± 0.035	0.8204± 0.0755	-0.243± 0.1013
H19	1.036± 0.0069	1.8433± 0.0403	0.8891± 0.0871	-0.3717± 0.114
H21	1.0004± 0.0071	1.747± 0.0412	0.6548± 0.0889	-0.4084± 0.1171
H23	0.9851± 0.0066	1.5393± 0.0374	0.0876± 0.0802	-0.3606± 0.1079
H25	1.0014± 0.0063	1.3708± 0.0351	-0.4737± 0.0745	-0.2618± 0.1027
H27	1.0116± 0.0058	1.3773± 0.0318	-0.7671± 0.0671	-0.1556± 0.0933
H29	1.0126± 0.0065	1.4852± 0.0359	-0.8464± 0.0756	-0.1553± 0.1046
H31	1.0246± 0.0072	1.6905± 0.04	-1.0238± 0.0841	-0.2056± 0.116
H33	0.9962± 0.0074	1.7121± 0.0409	-1.2818± 0.0854	-0.082± 0.1183
H35	0.9798± 0.0085	1.6738± 0.0468	-1.5311± 0.097	0.0303± 0.1356
H37	0.974± 0.0093	1.5712± 0.0506	-1.7932± 0.1041	0.2468± 0.1473
H39	0.9551± 0.0112	1.5546± 0.0611	-1.8459± 0.1254	0.3547± 0.1775

Table C.1: *List of coefficients obtained from fitting harmonic delay scans.*

Harmonic order	b_0	b_2	b_4	b_6
H9	1.1309± 0.0017	0.3292± 0.0045	-0.0786± 0.0093	0.0202± 0.0175
H11	1.1345± 0.0017	-0.2362± 0.0047	0.0073± 0.0097	-0.0074± 0.0204
H13	1.1725± 0.0058	0.7968± 0.015	0.4066± 0.0316	-0.0235± 0.0531
H15	1.16± 0.0079	1.5423± 0.0219	0.0037± 0.0401	0.2118± 0.0572
H17	1.1557± 0.0038	1.1935± 0.0099	0.5549± 0.02	0.0787± 0.031
H19	1.1922± 0.0063	1.8026± 0.0171	0.549± 0.0314	0.0572± 0.0434
H21	1.2184± 0.0064	1.7535± 0.0175	0.0555± 0.0315	0.0088± 0.0439
H23	1.1973± 0.0059	1.6643± 0.0165	-0.59± 0.0287	-0.0715± 0.0401
H25	1.1681± 0.0067	1.5426± 0.019	-1.0979± 0.0326	-0.213± 0.0462
H27	1.1676± 0.0074	1.5825± 0.0211	-1.3326± 0.0356	-0.2541± 0.0496
H29	1.1642± 0.0066	1.6925± 0.0189	-1.3861± 0.0314	-0.2203± 0.0422
H31	1.2189± 0.0077	1.8682± 0.0221	-1.6062± 0.036	-0.1726± 0.0468
H33	1.2327± 0.0085	1.8364± 0.0246	-1.8263± 0.0401	-0.1775± 0.0529
H35	1.2813± 0.0091	1.8009± 0.0264	-2.0931± 0.0433	-0.0909± 0.0586
H37	1.2853± 0.0092	1.6872± 0.0268	2.2221± 0.0443	-0.0447± 0.0619
H39	1.3528± 0.0106	1.6358± 0.0308	-2.2735± 0.0518	-0.0116± 0.0752

Table C.2: *List of coefficients obtained from fitting harmonic angle scans.*